

2014

Numerical modeling of pollutant emissions in practical combustion systems using detailed chemical kinetics

Sujith Sukumaran
Iowa State University

Follow this and additional works at: <https://lib.dr.iastate.edu/etd>

 Part of the [Mechanical Engineering Commons](#)

Recommended Citation

Sukumaran, Sujith, "Numerical modeling of pollutant emissions in practical combustion systems using detailed chemical kinetics" (2014). *Graduate Theses and Dissertations*. 13693.
<https://lib.dr.iastate.edu/etd/13693>

This Dissertation is brought to you for free and open access by the Iowa State University Capstones, Theses and Dissertations at Iowa State University Digital Repository. It has been accepted for inclusion in Graduate Theses and Dissertations by an authorized administrator of Iowa State University Digital Repository. For more information, please contact digirep@iastate.edu.

**Numerical modeling of pollutant emissions in practical combustion systems
using detailed chemical kinetics**

by

Sujith Sukumaran

A dissertation submitted to the graduate faculty in
partial fulfillment of the requirements for the degree of

DOCTOR OF PHILOSOPHY

Major: Mechanical Engineering

Program of Study Committee:

Song-Charng Kong, Major Professor

Stuart Birrell

Paul Durbin

Baskar Ganapathysubramanian

Terrence Meyer

Iowa State University

Ames, Iowa

2014

Copyright © Sujith Sukumaran, 2014. All rights reserved.

TABLE OF CONTENTS

LIST OF FIGURES	iv
LIST OF TABLES	viii
ACKNOWLEDGEMENTS	ix
ABSTRACT	x
CHAPTER 1. INTRODUCTION	1
1.1 Motivation	1
1.2 Objectives	2
CHAPTER 2. BACKGROUND AND LITERATURE STUDY	3
2.1 Combustion Modeling	3
2.2 Chemical Reaction Modeling	6
2.3 NO _x Modeling	7
2.4 Soot Modeling	9
2.5 Spray and Evaporation Modeling	10
2.6 Literature Review of Fuel-NO _x Modeling	13
2.7 Literature Review of Diesel Soot Modeling	16
2.8 Literature Review of Biodiesel Combustion Modeling	17
2.8 Literature review on spray model improvements	19
CHAPTER 3. FUEL NO _x EMISSIONS FROM PRODUCER GAS COMBUSTION	21
3.1 Objectives	21
3.2 Producer Gas Reaction Mechanisms	21
3.3 Mechanism Reduction Method	23
3.4 Model Details	27
3.5 Grid Independence Study	30
3.6 Burner Simulation Results	31
3.7 Designing Low NO _x Burners	46
3.7 Summary	50
CHAPTER 4. SOOT EMISSIONS FROM DIESEL SPRAY COMBUSTION	51
4.1 Objectives	51
4.2 Modeling Formulation	51

4.3 Soot Model	53
4.3 Results	59
4.4 Summary	74
CHAPTER 5. IMPROVEMENTS ON SPRAY AND EVAPORATION MODELS	75
5.1 Gas Parcel Model for Evaporating Sprays	75
5.2 Discrete Component Vaporization Model	81
5.3 Reaction Mechanism	82
5.4 Multi-Step Soot Model	83
5.5 Results	84
5.6 Summary	94
CHAPTER 6. CONCLUSIONS AND FUTURE RECOMMENDATIONS	96
6.1 Conclusions	96
6.2 Future Recommendations	97
APPENDIX A	100
APPENDIX B	108
REFERENCES	114

LIST OF FIGURES

Figure 3.1 NO mole fraction evolutions predicted using different mechanisms in a plug flow reactor with wood+40% DDGS derived producer gas as fuel	22
Figure 3.2 Rate of production of hydrogen reactions in a PSR with wood+40% DDGS derived producer gas as fuel	24
Figure 3.3 Ignition delay comparison of GRI-full mechanism and reduced mechanism ($\phi=1.0$, $p=1$ atm, fuel=wood+40% DDGS derived producer gas)	26
Figure 3.4 Comparison of laminar flame speed predicted using GRI 3.0 mechanism and the present reduced mechanism ($T_0=1000$ K, $p=1$ atm, fuel=wood+40% DDGS derived producer gas)	26
Figure 3.5 Comparison NO mole fractions predicted using GRI 3.0 mechanism and the present reduced mechanism ($T_0=600$ K, $p=1$ atm, fuel=wood+40% DDGS derived producer gas)	27
Figure 3.6 Schematic of the burner used for producer gas combustion	28
Figure 3.7 Computational mesh of the burner (within 0.5 m) and combustion chamber. Note that the scale is not linear.	30
Figure 3.8 NO mole fraction at burner nozzle exit using different mesh density	31
Figure 3.9 NO _x emissions measured (lines) [33] and predicted (symbols) using the reduced mechanism	33
Figure 3.10 Contours of NO (left half of each plot) and temperature (right half) of producer gas combustion derived from wood	34
Figure 3.11 Contours of NO (left half) and temperature (right half) of producer gas combustion derived from wood + 13%DDGS	36
Figure 3.12 Contours of NO (left half) and temperature (right half) of producer gas combustion derived from wood + 40%DDGS	37
Figure 3.13 NO reaction rate contours (left half) and Temperature contours (right half) in the flame region ($\lambda=1.54$, wood+13%DDGS gas)	37
Figure 3.14 Net reaction rates of each NO reaction in the domain with different producer gas composition at λ approximately equal to 1.6	38
Figure 3.15 Temperature-MER map of net NO rate in wood+13%DDGS gas combustion at $\lambda=1.54$	40
Figure 3.16 Temperature-MER map of the reaction rate of $\text{NO}_2+\text{H}\rightleftharpoons\text{NO}+\text{OH}$ in wood+13%DDGS (reaction#142) gas combustion at $\lambda=1.54$	41

Figure 3.17 Temperature-MER map of the reaction rate of $\text{NH}+\text{O} \leftrightarrow \text{NO}+\text{H}$ in wood+13%DDGS (reaction#143) gas combustion at $\lambda=1.54$	42
Figure 3.18 Temperature-MER map of the reaction rate of $\text{N}+\text{CO}_2 \leftrightarrow \text{NO}+\text{CO}$ in wood+13%DDGS (reaction#191) gas combustion at $\lambda=1.54$	42
Figure 3.19 Temperature-MER map of the reaction rate of $\text{N}+\text{NO} \leftrightarrow \text{N}_2+\text{O}$ in wood+13%DDGS (reaction#136) gas combustion at $\lambda=1.54$	44
Figure 3.20 Temperature-MER map of the reaction rate of $\text{CH}_3+\text{NO} \leftrightarrow \text{HCN}+\text{H}_2\text{O}$ (reaction#181) in wood+13%DDGS gas combustion at $\lambda=1.54$	44
Figure 3.21 Temperature-MER map of the reaction rate of $\text{HO}_2+\text{NO} \leftrightarrow \text{NO}_2+\text{OH}$ (reaction#139) in wood+13%DDGS gas combustion at $\lambda=1.54$	45
Figure 3.22 Temperature-MER map of NO production/consumption rate in wood+13%DDGS gas combustion at $\lambda=1.54$	46
Figure 3.23 Schematic of the three new burner designs (D2: with additional air stages, D3: with bluff body, D4: with constricted flame for recirculation)	48
Figure 3.24 Temperature (Left) and NO mole fraction (Right) contours on different burner designs	49
Figure 3.25 Predicted NO emissions using D1-D4 burner designs	49
Figure 4.1 Comparison of predicted and experimental data on (a) ignition delay and (b) flame speed	52
Figure 4.2 Comparison of the soot levels predicted by the two-step soot model (left) and experimental results (right) at an ambient density of 14.7 kg/m^3	54
Figure 4.3 Soot (ppm) contours in constant volume combustion chamber at 15% O_2 and 14.7 kg/m^3 ambient density using the multi-step soot model on different mesh sizes	60
Figure 4.4 Soot (ppm) by simulation (left) and experiment (right) at different EGR levels for ambient density of 14.7 kg/m^3 .	62
Figure 4.5 Soot (ppm) by simulation (left) and experiment (right) at different EGR levels for ambient density of 30 kg/m^3 .	63
Figure 4.6 Comparisons of the lift-off locations identified by experiments and simulation for 8% O_2 EGR level. Predicted flame temperature is also shown.	64
Figure 4.7 (a) Predicted and measured ignition delays at different EGR levels, (b) Comparison of the pressure histories by experiment (solid) and simulation (dashed)	65

Figure 4.8 Comparison of predicted soot contours using the present model (left) and the previous soot model in literature [61] (right) at ambient conditions (a) 14.5 kg/m ³ and 21% O ₂ (b) 30.0 kg/m ³ and 15% O ₂	66
Figure 4.9 Comparison of predicted in-cylinder pressure (MPa) and heat release rate (J/CAD) with experimental data for 8% EGR level	68
Figure 4.10 Comparison of predicted and measured engine-out soot data (g/kg-fuel)	69
Figure 4.11 In-cylinder soot evolutions for different EGR levels for SOI= -10 ATDC	70
Figure 4.12 Contours of temperature (left) and soot (right) at different times for 8% EGR, SOI= -10 ATDC	71
Figure 4.13 Contours of temperature (left) and soot (right) at different times for 8% EGR, SOI= 0 ATDC	72
Figure 4.14 Comparison of predicted and measured engine out NO _x data (g/kg-fuel)	73
Figure 4.15 Predicted Soot-NO _x trade-off for the SOI sweeps at different EGR levels	73
Figure 5.1 Liquid (L) and vapor (G) penetration of fuel spray using standard evaporation model KIVA-3V on different grid sizes compared with experimental liquid and vapor penetration results [115]	76
Figure 5.2 Schematic of gas parcel model	80
Figure 5.3 Diesel spray penetration data from experiments [124] and simulation at an ambient temperature of 1000K and different ambient densities	85
Figure 5.4 Experimental [115] and predicted liquid spray and fuel vapor penetration of n-dodecane spray at an ambient temperature of 900K.	86
Figure 5.5 Experimental [83] and predicted liquid spray and fuel vapor penetrations of biodiesel at an ambient temperature of 900 K	87
Figure 5.6 Experimental [83] and predicted liquid spray penetration of biodiesel at different ambient temperatures	88
Figure 5.7 Comparison of experimental and predicted single droplet vaporization curves using biodiesel at different ambient temperatures	89
Figure 5.8 Experimental (left half) and simulation (right half) results showing soot contours (ppm) and flame lift-off location (dashed lines) using diesel fuel (D2) and biodiesel (BD) at 1000 K and 900 K ambient temperatures	91
Figure 5.9 Temperature contours of diesel fuel (D2) and biodiesel (BD) flame at 5.5 ms at 900 K ambient temperature.	92

LIST OF TABLES

Table 3.1. Major Species composition (vol%) of producer gas for different biomass feedstocks	29
Table 3.2. Operating conditions for simulations	32
Table 4.1 Engine specifications	67
Table 5.1 FAME composition of RME [65] and SME [83] biodiesel	89
Table 5.2 John-Deere medium-duty diesel engine specifications	93

ACKNOWLEDGEMENTS

First and foremost, I would like to express my sincere gratitude to my advisor Prof. Song-Chang Kong for the continuous support he has rendered throughout my graduate study at Iowa State University. His guidance and acumen has led me through the right directions for the progress of this research. His motivation and patience helped me to perform the research in an efficient manner. I would also like to thank him for his moral support during the ups and downs in this thesis work.

Besides my advisor, I would like to thank the rest of my committee members, Dr. Stuart Birrell, Dr. Paul Durbin, Dr. Baskar Ganapathysubramanian, and Dr. Terry Meyer for being in my committee and providing their honest feedback on my research. I am also thankful to Dr. Nam-Hyo Cho of John Deere Power Systems for valuable discussions on diesel spray simulations. I would like to acknowledge the financial support of National Science Foundation, Iowa Office of Energy Independence and John Deere Power Systems. I would also like to mention my appreciation to department of Mechanical Engineering at Iowa State for giving me the opportunity to learn and teach at this wonderful institution and also for the financial assistance provided. I am indebted to my fellow labmates for the research atmosphere they have provided in the lab and all their help throughout my life at Iowa State and I wish them all good luck in their current and future endeavors.

Heartfelt thanks goes especially to my parents, wife and the rest of the family for their endless love and support, which is always an essential part of my life. I also thank all my friends for their constant help and support over the years.

ABSTRACT

Pollutant emissions from combustion systems are a major area of concern with today's energy needs. Numerical simulations have helped with the design of clean and efficient combustion strategies over the years. However, with the emergence of new fuels and combustion modes, it is necessary to improve the computational models. In this research, improved NO_x and soot models are developed which uses detailed chemical kinetics in order to simulate the combustion phenomenon. These models are coupled with Computational Fluid Dynamics (CFD) to predict the NO_x and soot emissions in practical combustion systems.

In the first part of the dissertation, a reduced chemical reaction mechanism is developed for modeling the combustion of biomass-derived gas (i.e., producer gas or synthesis gas). The mechanism reduction is performed on a well-validated comprehensive mechanism that was designed to simulate the combustion of natural gas constituents and NO_x emissions. The reaction mechanism also includes species and reactions related to the combustion of ammonia, which is an important component in the producer gas. Combustion experiments of a pilot-scale burner are simulated using the developed mechanism, and the model is able to predict the NO_x emission levels resulting from different feedstocks under a wide range of operating conditions. Detailed analyses of the simulation results are performed in order to determine the NO_x generating regions in the flame and reaction pathways leading to formation and destruction of NO_x. Further, new burner designs are evaluated using the model in order to select the best design for reduced NO_x emissions.

The second part of this research is focused on modeling soot emissions from diesel engine combustion. A multi-step soot model is developed which uses a detailed Poly-Aromatic Hydrocarbon (PAH) chemistry in order to predict the soot emissions from diesel combustion. The baseline n-heptane mechanism is modified by adding the PAH chemistry. The reaction mechanism is validated for ignition delay and flame speed. Further, the model is also validated using constant-volume combustion chamber experiments and diesel engine experiments at different operating conditions. The model is able to accurately predict the soot forming regions and engine out emissions over a wide range of operating conditions.

In addition to the pollutant emissions modeling, the existing diesel spray and evaporation models in the baseline CFD code, KIVA-3V, are improved. A gas parcel model is implemented in the baseline code to improve the prediction of vapor penetrations of evaporating sprays. The model is able to predict accurately the vapor penetration of different fuels at different operating conditions. A discrete-component vaporization model is implemented into the baseline code for predicting the vaporization of biodiesel. Coupled with the multi-step soot model, the new models in KIVA-3V are used to simulate the combustion experiments in a constant-volume chamber and a diesel engine using diesel fuel and biodiesel. The model is able to predict the reduction in soot emissions when biodiesel is used.

CHAPTER 1. INTRODUCTION

1.1 Motivation

Combustion plays a crucial role in meeting the world's energy needs. A majority of today's combustion fuels are fossil fuels, such as coal, oil and natural gas. Greenhouse gas emissions resulting from combustion of these fuels are a major concern because of its impact on climate change. Biorenewable fuels have also been used for combustion in an effort to mitigate the life-cycle greenhouse emissions. Regardless of the source of the fuel, combustion will generate pollutants that have negative impacts on the environment and health. Therefore, research on clean and efficient combustion has been an active area of research.

NO_x and soot are two of the major pollutants resulting from combustion [1]. NO_x is a mixture of nitrogen oxides, i.e., NO and NO_2 . Soot on the other hand has a more complex structure. It is generally formed from fuel rich combustion and is basically an agglomerate of complex hydrocarbons. NO_x in the atmosphere can result in acid rain, which deteriorates the ecosystem. By reacting with ammonia and moisture, NO_x can form small particles which will result in aggravating respiratory disorders in human beings. Diesel soot particles are found to be carcinogenic and pose a serious threat to human health[2]. As a result, emission regulations for these pollutants have become increasingly stringent around the world. The national ambient air quality standards require the NO_2 level to be within 53 parts per billion (ppb) as an annual average. To obtain such standards, low NO_x burners are recommended by EPA for industrial applications. In the case of diesel soot, the Tier 4 emission standards dictate the soot to be under 0.01 g/bhp-hr for heavy duty engines.

Improvements in combustion devices are required to meet such emission requirements. Computational models are proven to be very effective in designing clean and efficient

combustion devices. Computational Fluid Dynamics (CFD) is a tool that can mathematically model the fluid flow in a combustion device and can give detailed insights into the pollutant formation process. It is crucial to use accurate CFD models to predict the emissions accurately. With the application of supercomputing, detailed chemistry can be utilized to predict the combustion process and resolve all the major species that are involved in combustion [3]. Accurate computational models that consider the complex fluid flow and detailed chemistry are critical to help design and optimize clean and efficient combustion systems.

1.2 Objectives

The objective of this study is to develop accurate fluid dynamic and chemical kinetic models that can be used as a tool to analyze and design combustion systems. In this dissertation, NO_x and soot models are developed based on detailed chemistry to accurately predict the NO_x and soot emissions in different applications. The NO_x model will be used to predict the NO_x emissions resulting from combustion of biomass-derived synthesis gas, and the soot model will be used to predict the soot emissions from compression-ignition engines using diesel and biodiesel.

CHAPTER 2. BACKGROUND AND LITERATURE STUDY

2.1 Combustion Modeling

Combustion modeling plays a key role in the accurate prediction of pollutants. There are different approaches to model combustion, and some of the approaches are discussed here in detail. In order to model gas phase reactions, it is necessary to model the transport of each species involved in combustion. As a result of combustion, a source term or a sink term appear in the species transport equation. A general form of the governing equation for species transport is shown in Equation (2.1).

$$\frac{\partial}{\partial t}(\rho Y_i) + \frac{\partial}{\partial x_j}(\rho u_j Y_i) = -\frac{\partial}{\partial x_j}(J_j^i) + R_i \quad (2.1)$$

Turbulent combustion can be generally classified into two categories, premixed and non-premixed combustion. Homogeneous-charge spark-ignition engines are an example of premixed combustion system, and diesel engines are based on non-premixed combustion. The present research mainly focuses on non-premixed combustion systems. Some of the commonly used non-premixed combustion models are discussed in this section. Chemical reactions are represented by a set of chemical reaction equations. A standard practice is to formulate the reaction rate parameters into a format that can be accepted by the CHEMKIN code [4] for use in the CFD solver. In the case of a laminar flame, R_i can be calculated directly from the reaction rate. This type of kinetics-controlled chemistry approach is valid for slow reactions with negligible turbulent-chemistry interactions. However, most of the combustion flames are turbulent in nature and turbulent mixing has a dominant effect on the overall combustion rates.

There are various approaches to model turbulent combustion. One method is to use the averaged balance equations to describe only the mean flow field with local fluctuations and

turbulent structures integrated into mean quantities. As density fluctuations will be present in the reacting flows because of the thermal heat release, a Favre averaging [5], as opposed to the traditional RANS average, is used. The Favre-averaged species transport equation is shown in Equation (2.2).

$$\frac{\partial}{\partial t}(\bar{\rho}Y_i) + \frac{\partial}{\partial x_j}(\bar{\rho}u_j Y_i) = -\frac{\partial}{\partial x_j}(\bar{\rho}u_j''Y_i'') - \frac{\partial}{\partial x_j}\bar{J}_j^i + \bar{R}_i \quad (2.2)$$

The averaging gives rise to unresolved terms, such as $u_j''Y_i''$, which has to be closed using appropriate assumptions. A standard practice is to use the gradient transport hypothesis.

$$\bar{\rho}u_j''Y_i'' = -\frac{\mu_t}{Sc_{kt}}\left(\frac{\partial Y_k}{\partial x_j}\right) \quad (2.3)$$

Another term that requires a closure model is the mean burning rate, \bar{R}_i . Turbulent combustion models are used here for closure. The model based on the eddy dissipation concept is an example [6]. This model assumes that reactions occur in small turbulent structures, known as fine scales (L^*) over a fine time scale (τ^*). The resulting turbulent chemical length and time scales are calculated as follows.

$$L^* = C_L \left(\frac{\nu^3}{\varepsilon}\right)^{1/4} \quad (2.4)$$

$$\tau^* = C_\tau \left(\frac{\nu}{\varepsilon}\right)^{1/2} \quad (2.5)$$

C_L is the length scale constant (1.43), and C_τ is the time scale constant (0.41). ν is the kinematic viscosity, ε is turbulent dissipation rate, and k is turbulent kinetic energy.

Another method to model turbulent combustion is the so-called flamelet model. In this approach, combustion is assumed to take place over thin layers known as flamelets. The turbulent flame brush is treated as the average of numerous laminar flamelets subjected to statistical probability distribution similar to turbulent fluctuations. The combustion is modeled as a function of mixture fraction (Z). Mixture fraction is a function of local mixing of fuel and oxidizer. The mixture fraction is defined as

$$Z = \frac{\dot{m}_{fuel}}{\dot{m}_{fuel} + \dot{m}_{ox}} \quad (2.6)$$

\dot{m}_{fuel} is the fuel flow rate, and \dot{m}_{ox} is the oxidizer flow rate. The chemical reaction rates can be calculated as a function of mixture fraction and can be stored in look-up tables. During the CFD calculations, these reaction rates can be easily obtained from the lookup tables based on the local mixture fraction, thus reducing the computational cost of solving complex chemical reactions.

Other closure models for turbulent combustion are also developed, such as eddy dissipation model [7], RIF model [8], Shell model [9], and characteristic time scale model [9]. These alternate models are suited for simple global reaction mechanisms rather than detailed chemical mechanisms. Although these models are much more computationally efficient than the detailed chemistry models, the accuracy is limited. In order to model the pollutants from combustion, it is critical to model the detailed reaction pathways leading to the formation of these pollutant species. A detailed chemistry approach is preferable for such applications, and hence in the present research work detailed chemistry models will be used.

2.2 Chemical Reaction Modeling

As discussed in the previous section, the chemical reactions involved in combustion are expressed as a set of reaction equations with their rates expressed in the Arrhenius form. A typical reaction in CHEMKIN format is shown in Equation (2.7).

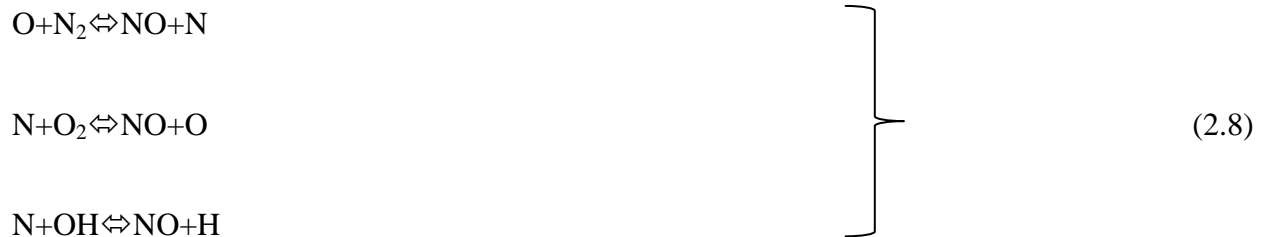


Here A and B are the reactants, and C and D are the products. The double arrows indicate that the reaction occurs in both directions. The first number after the reaction is the pre-exponential factor, the second number is the temperature exponent, and the last number is the activation energy in the Arrhenius rate equation. These constants are determined using a wide range of experiments, such as shock tubes, laminar flames, rapid compression machines, flow reactors, stirred reactors, and practical systems [10]. Comprehensive reaction mechanisms for various fuels have been developed over the past few decades. However, for practical applications these comprehensive mechanisms are computationally expensive. Thus, reduced mechanisms were developed in order to model practical combustion systems using CFD. The methodology to reduce mechanisms itself is a widely researched area. Some of the recent reduction strategies are direct relation graph (DRG) [11] and computational singular perturbation (CSP) [12] methods. In DRG method, a relation graph is plotted based on the contribution of each species in the mechanism in the production of other species. The connections between two species are marked by an arrow and a normalized contribution factor of the original species in the production of end species. Once the contribution factors between all species are determined, the connections with low contribution factors can be removed to reduce the mechanism. The CSP algorithm decouples fast and slow chemistry and using this data quasi steady species (QSS) can be identified to reduce the mechanism.

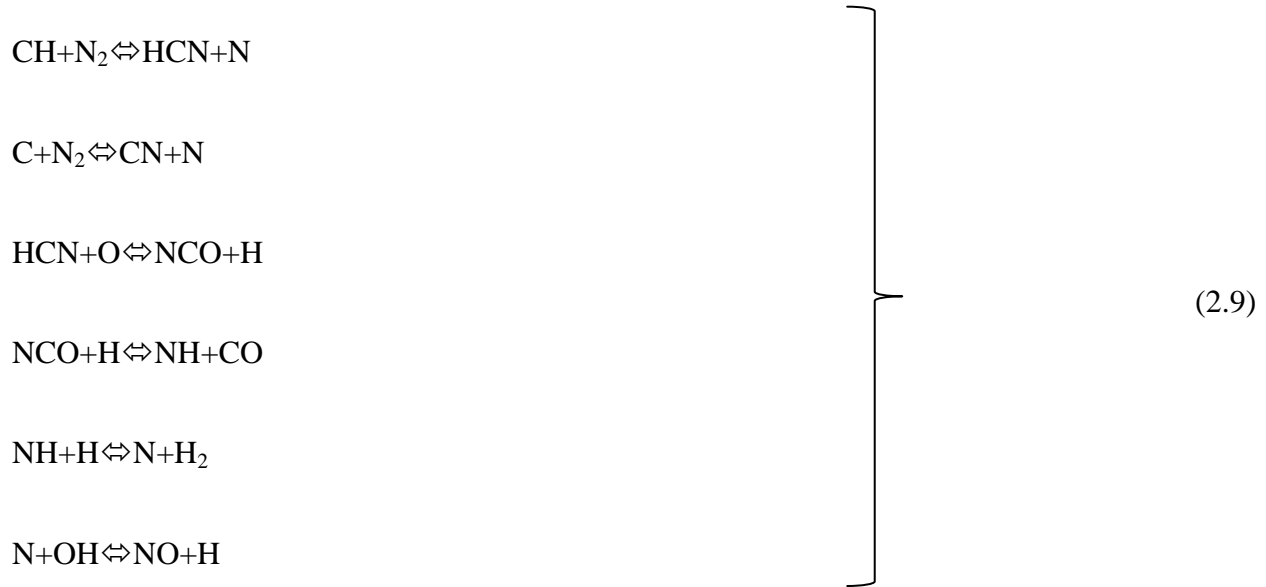
The reduced mechanisms can be validated with the detailed mechanisms using zero-dimensional reactor models. Two of reactor models used in this study are perfectly stirred reactor (PSR) and plug flow reactor (PFR). PSR is a zero dimensional reactor with the assumption that the species are well mixed and the composition is homogeneous throughout the reactor. When modeling combustion chemistry in CFD, each computational cell is assumed to be a PSR and reactions calculations are carried out in each cell. PSR is used to model the ignition delays predicted by the reaction mechanism. Plug Flow Reactor is a one dimensional reactor model with the approximation that the composition along the cross section of reactor is homogeneous. PFR reactor is a good initial approximation to model steady state burner flames. In this study PFR is used to compare the predictions of different reaction mechanisms.

2.3 NO_x Modeling

NO_x emissions from combustion systems is the sum of NO and NO₂. Since the quantity of NO is usually much greater than NO₂ in regular combustion systems, only NO needs to be considered in most of the applications. There are three types of mechanisms to produce NO_x, namely thermal NO_x, prompt NO_x, and fuel NO_x mechanisms [5]. The thermal NO_x is generated from the oxidation of N₂ present in the combustion system. This occurs at temperature above 1800 K and is a strong function of temperature. It is the major source of NO_x emissions from diesel engines. In numerical simulations, this is generally modeled using a three-step reaction known as Zeldovich mechanism, as shown in Equation (2.8).



In the prompt NO_x mechanism, NO is formed due to combustion of hydrocarbons in fuel rich zones. Hydrocarbons react with molecular nitrogen to form amines or cyano compounds. Prompt NO_x is generally observed in fuel rich flames. These compounds are converted to intermediate compounds which ultimately form NO as shown in Equation (2.9).



Fuel NO_x is formed from the fuel-containing nitrogen. Solid fuels, such as coal and woody biomass, contain nitrogen in low quantities. Gaseous fuels, such as producer gas contains nitrogen in the form of ammonia (NH_3), which serves as the source of fuel NO_x production. The reaction pathways for fuel NO_x differ for different fuels.



Reaction equations in Equation (2.10) are some other NO forming pathways, such as the N_2O intermediate mechanism and NNH mechanism. The NO- NO_2 interchange reaction, as shown in Equation (2.11), has been found to play a significant role in homogeneous-charge compression-ignition engine systems [13].



2.4 Soot Modeling

Soot formation in combustion is a complex process that involves both chemical and physical processes. The soot emissions are a result of chemical kinetics leading to the formation of soot precursors and further soot dynamics, including soot nucleation, surface growth, coagulation, oxidation and particle dynamics of soot. The evolution of soot in flames is not completely understood and is an active area of research today. As a result, modeling of soot formation in combustion is challenging.

The traditional two-step soot model [14] uses a soot formation step and a soot oxidation step to calculate the net soot production in the computational cell. Soot is modeled as an additional gas phase species with source and sink terms corresponding to the formation and oxidation of the soot as shown in Equation (2.12).

$$\frac{dM_{soot}}{dt} = \dot{M}_{sootf} - \dot{M}_{sootox} \quad (2.12)$$

\dot{M}_{sootf} , the rate of soot formation step and \dot{M}_{sootox} , the rate of soot oxidation are modeled as

$$\dot{M}_{sootf} = M_f A_{sf} P^{0.5} \exp\left(-\frac{E_{sf}}{R_u T}\right) \quad (2.13)$$

$$\dot{M}_{soot,x} = A_o M_{soot} \frac{P_{O_2}}{P} P^{1.8} \exp\left(-\frac{E_{so}}{R_u T}\right) \quad (2.14)$$

Here M_f is the mass of soot precursor species, which is either fuel or species, such as C_2H_2 , which is important to the formation of soot. P is the ambient pressure, P_{O_2} is the partial pressure of oxygen, T is the ambient temperature, and R_u is universal gas constant. A_{sf} and A_o are model constants that can be calibrated with the baseline measured soot emissions.

Although the two-step model is commonly used in modeling diesel soot emissions, with the emergence of new combustion technologies, such as low temperature combustion and dual-fuel combustion, this simplified model can be inadequate. As a result, multi-step soot models are developed to accurately predict the soot emissions. More details about the multi-step soot model will be described in Chapter 4.

2.5 Spray and Evaporation Modeling

A crucial step in the simulation of diesel combustion is the spray and evaporation modeling of liquid fuel. In a compression ignition (CI) engine, diesel fuel is sprayed into the combustion chamber, where it atomizes and evaporates to form the diesel vapor. Under high temperature and pressure this vapor autoignites to start the combustion process. In order to accurately model the diesel engine processes, it is critical to incorporate accurate spray and evaporation models. The diesel sprays are typically modeled using Lagrangian spray parcels injected to the Eulerian gas phase [15-17]. A parcel is a collection of spray particles with similar characteristics, such as location, size and temperature. Clustering of such similar particles reduces computational time without much loss in accuracy. These Lagrangian parcels, collections of fuel droplets, are injected into the Eulerian gas phase where it loses the initial momentum to the gas phase. As the droplets moves through the combustion chamber, they

evaporate to become diesel vapor. Thus constant mass and momentum exchange occur between the liquid droplet and gas vapor. The droplets also undergo physical processes such as spray breakup and collision. There are two stages of the breakup process, namely primary breakup and secondary breakup. In the primary breakup regime which is closer to the injector, the larger particles are broken down due to the stretching of droplets at high velocity. In the secondary breakup regime, the smaller droplets split into further smaller droplets due to instabilities. There are different models available to model the spray breakup such as TAB and KH-RT models [18-20]. Droplet collision results in coalescence or grazing of two droplets. Droplet coalescence is modeled using a stochastic collision model [21]. The evaporation of liquid droplets is taken care of by the evaporation model. For diesel sprays, a single component evaporation algorithm is used to calculate the evaporation rate of each droplet.

In the standard evaporation model for single component, the rate of the change of droplet radius, \dot{R} is given by the Frossling correlation [22].

$$\dot{R} = - \frac{(\rho D)_{air} (Y_1^* - Y_1)}{2\rho_d r (1 - Y_1^*)} Sh_d \quad (2.15)$$

In the above equation, $(\rho D)_{air}$ is the fuel vapor diffusivity in air, Sh_d is the Sherwood mass transfer number, Y_1^* is the fuel vapor mass fraction at the surface of droplet, Y_1 is the fuel vapor mass fraction at away from droplet, ρ_d is the density of droplet and r is the radius of droplet. The surface mass fraction is obtained from Raoult's law as shown in Equation (2.16).

$$X_i^* = X_i \frac{P_{vap}(T_s)}{P} \quad (2.16)$$

X_i^* and X_i represent the fuel mole fractions at the outside and inside of the droplet surface. P_{vap} is the vapor pressure at the surface temperature and P is the ambient pressure.

The temperature change of droplet due to evaporation is determined by the energy balance equation between heat conduction to the droplet and latent heat of vaporization as shown in the following equation.

$$\frac{4}{3}\rho_d\pi r^3 c_l \dot{T}_d - \rho_d 4\pi r^2 \dot{R}L(T_d) = 4\pi r^2 Q_d \quad (2.17)$$

In Equation (2.17), T_d is the droplet temperature, c_l is the liquid specific heat, $L(T_d)$ is the latent heat of vaporization and Q_d is the rate of heat conduction to the droplet surface per unit area. The heat conduction rate is given by the Ranz-Marshall correlation [22].

$$Q_d = \frac{K_{air}(T - T_d)}{2r} Nu_d \quad (2.18)$$

K_{air} is the thermal conductivity of air, T is the ambient temperature and Nu_d is the Nusselt number of droplet. Equation (2.17) is solved coupled with Equation (2.15) using Newton iteration.

Petroleum fuels are multicomponent in nature but they are usually represented as single component fuels in most evaporation models for the ease of calculations. For example, tetradecane ($C_{14}H_{30}$) is used as a surrogate fuel for diesel and iso-octane (C_8H_{18}) is used for gasoline. These species are chosen because they have similar physical properties (e.g., density and surface tension) to diesel and gasoline, respectively. However, this simple single-component approach can be inadequate to model the preferential vaporization of light components in the practical multi-component fuels. Moreover, with the introduction of biodiesel, the properties of

fuels vary considerably based on the feedstock. Thus, a multi-component vaporization model is necessary to accurately accommodate these fuel variations. Two main approaches of multi-component modeling are the continuous thermodynamics model and the discrete component model. In the continuous thermodynamics model the liquid composition and the consequent properties were defined as a probability density function. This model is computationally efficient but it does not provide specific information about the individual species within the liquid droplet or gas species. The discrete component approach treats each component independently and is able to provide the specific information of each species in the fuel. With this additional information, the chemistry model can be further developed to improve the emission predictions.

2.6 Literature Review of Fuel-NO_x Modeling

The growing demand for renewable energy and carbon-neutral fuels has propelled research on energy that can be derived from biomass. The efficient utilization of biomass energy can play a key role in reducing the life-cycle greenhouse gas emissions as well as providing economic security for many nations [23]. Biomass can be converted to transportation fuels or various forms of energy through biochemical or thermochemical conversion. Biochemical conversion is the conversion of biomass to fuel or other chemicals with the help of enzymes and microorganisms. Thermochemical processes include direct combustion, gasification, and pyrolysis [24]. Gasification converts solid biomass to a gas mixture which in turn can be burned to generate heat or synthesized to produce various liquid fuels [25, 26]. Gasification is a relatively mature technology and has the flexibility of utilizing a variety of feedstocks. For instance, agricultural waste or forest residue can be used for gasification, which makes it an attractive option for stationary power generation at many locations. On the other hand, power generation using integrated gasification combined cycle (IGCC) technology has proven to

produce much lower emissions than the direct combustion system [27]. The gas mixture derived from gasification is known by different names, e.g., synthesis gas, syngas, manufactured gas, or producer gas. In this thesis, the term “producer gas” is used to identify the gas derived from biomass gasification, which has a lower energy content than syngas derived from coal.

One of the major concerns of using producer gas or syngas for combustion is nitrogen oxides (NO_x) emissions. The fuel-bound nitrogen in producer gas undergoes oxidation to form NO_x . In biomass-derived producer gas combustion, ammonia is the main nitrogen-containing, combustible species whose combustion can produce significant amount of fuel NO_x emissions.

An extensive body of research is available on NO_x formation from coal-derived syngas combustion. Simulations were conducted using opposed-flow diffusion flames and it was found that thermal NO_x can be reduced by increasing the flame stretch [28]. Combustion simulations of ammonia-doped flame were conducted using an eddy dissipation concept model to predict NO_x emissions [29]. GRI 2.11 [30] was used to model the reaction and NO emissions and was able to obtain good agreement with experiment data. It was also found in the above study that the rate of NO produced from ammonia was much higher than thermal NO_x . In another study, a counter-flow syngas flame was modeled with the presence of diluents, and results showed that the presence of methane in syngas increases prompt NO formation and the presence of H_2O , CO_2 and N_2 diluents in the air stream reduces NO_x in the flame [31]. In a recent study, syngas diffusion flames were simulated using detailed chemistry along with a narrowband radiation model [32]. The results showed that the predicted peak temperature and NO_x were reduced when radiation was modeled. Most of these studies were focused on the thermal NO_x emissions as the syngas contains negligible amount of ammonia. On the other hand, it has been observed from experimental studies that producer gas generated from wood and seed corn has a non-negligible

amount of ammonia and the combustion of these gases can generate high NO_x emissions due to ammonia combustion [33, 34]. Fuel NO_x from the combustion of biomass-derived gas containing ammonia in a gas turbine combustor was modeled using a laminar flamelet model with a simplified global reaction mechanism for NO formation [35]. It was observed that the major contribution of NO_x emissions is from fuel NO_x . The results from the above study also revealed that the simplified mechanism for NO formation was not adequate to predict the trend of NO_x emissions.

It is critical to understand ammonia combustion chemistry in order to model fuel NO_x emissions from producer gas combustion. During combustion, nitrogen in ammonia is converted to either N_2 or NO_x , depending on the reaction conditions. The fuel NO_x formation pathways for ammonia combustion were examined in previous works [36-40]. In one of the early works, experimental studies were conducted on $\text{NH}_3\text{-NO-O}_2\text{-H}_2\text{O}_2$ system and it was found that presence of H_2O_2 helps in NO reduction reactions [36]. A 21 step ammonia combustion mechanism was also developed in the above work. In another work, modeling studies were performed on a non-premixed turbulent syngas flame containing ammonia, using a simple three-step mechanism to predict fuel NO_x and it was able to capture the NO_x trend [37]. A comprehensive review of NO_x formation pathways was given by Miller and Bowman [38]. Numerical studies on combustion of the syngas containing ammonia was performed using a series of plug flow reactors, and it was found that the fuel-bound nitrogen can be effectively converted to N_2 by increasing the pressure and staging [39]. Further studies revealed that a combined fuel staging, air staging, and selective non-catalytic reduction method can be very effective in reducing NO_x in low temperature reactors [41]. In another numerical investigation, it

was observed that ammonia to NO conversion efficiency decreases as ammonia concentration increases [40].

2.7 Literature Review of Diesel Soot Modeling

Numerical modeling of soot emissions started in as early as 1970s. Tenser et al. [42] studied soot formation in an acetylene-hydrogen flame and proposed that an intermediate radical of carbon compounds will become a soot nucleus. The soot model proposed consisted of conservation equations for radical nuclei and soot number density. This soot model was later improved by considering the formations and growths of the radical nuclei and the soot particle nuclei at different stages [43]. The standard KIVA-3V [15] soot model is primarily based on this approach with the addition of soot oxidation based on the reaction rates by Nagle and Strickland-Constable [44]. For practical applications, simplified soot mechanisms were developed for use in multi-dimensional engine simulations. A two-step soot model was used for diesel engine simulations which used an empirical first order reaction for soot formation and second order reaction for soot oxidation [14]. The two-step soot model and its modifications are widely used because of its ease of implementation and adjustable features [20, 45, 46]. In the above studies, intermediate radicals for soot nucleation were not considered. Because of this limitation, these models used fuel concentration to determine the soot inception rate. The advancements in computational resources have paved the way to use detailed chemical kinetics for combustion simulation [3]. Accordingly intermediate radical such as acetylene was used as the soot precursor species [47, 48]. However, recent studies have showed that acetylene may not be an appropriate soot precursor species, particularly under low temperature conditions [49]. Thus, polycyclic aromatic hydrocarbons (PAH) were proposed as soot precursors.

Detailed soot kinetic mechanisms have also been developed based on fundamental chemistry studies. Chemical kinetics for soot formation was derived based on measurements from laminar premixed flames [50-52] and counter-flow diffusion flames [53, 54]. An improved version of the Tesner soot model was also developed, including soot nucleation, surface growth, coagulation and destruction [55]. This soot model, coupled with gas phase chemistry using acetylene as the soot precursor species, was able to produce promising results for a wide range of counter-flow flames. Encouraged by this success, various researchers proposed multi-step soot models which consist of soot nucleation, surface growth, oxidation and agglomeration [56, 57]. The multi-step soot model was able to predict soot number density and soot diameter in addition to soot mass fractions. As a result, different variations of the multi-step model were derived for diesel spray combustion simulation [58, 59]. In recent studies higher hydrocarbons such as fullerene was used as soot precursor species [60]. The model was later improved by using a reduced mechanism for PAH chemistry with pyrene as the soot precursor species [61]. This model was able to predict the soot emissions at low temperature combustion conditions. However, at very high exhaust gas recirculation (EGR) levels, the above mechanism over-predicted the soot emissions and more detailed models were required at these conditions.

2.8 Literature Review of Biodiesel Combustion Modeling

Biodiesel can be derived from vegetable oils, animal fats, and nonfood biomass and is considered one of the major alternatives to the traditional diesel fuel. The engine running on biodiesel is found to produce significantly less particulate matter (PM) (or soot), total hydrocarbon (THC), and CO emissions [62]. However, the physical properties (e.g., volatility, viscosity, surface tension) and chemical composition of biodiesel are relatively different from those of conventional diesel fuel. Biodiesel produced from different feedstock also vary in

composition, which further gives rise to different properties [63]. This leads to different spray characteristics, such as vaporization rate and liquid length, and combustion behaviors, such as emissions and lift-off lengths. Computational Fluid Dynamics (CFD) simulations can be used as a tool to study the effect of fuel properties on spray and combustion.

In conventional diesel combustion simulations, the liquid fuel droplet is modeled as a single-component surrogate fuel (e.g., dodecane or tetradecane). This approach may work reasonably well for diesel fuel under traditional, high-temperature combustion conditions. In the case of biodiesel, its properties can vary drastically depending on the feedstock. Thus, a multi-component approach is required to model biodiesel droplet vaporization. Some of the previous research has laid the foundation for modeling multi-component fuel vaporization [64-66]. Two main approaches used in multi-component vaporization models are the continuous thermodynamics model and the discrete component model [65, 67]. In the continuous thermodynamics model, the molecular weight of the liquid fuel is represented by a distribution function. During vaporization this distribution function evolves as the lighter components vaporize earlier. This approach can be more computationally efficient than the discrete component model, which models the vaporization of individual species in the liquid droplet. Biodiesel is typically modeled using the discrete component approach as it can be represented as a mixture of several major components. Biodiesel derived from vegetable oils are mainly made of fatty acid methyl esters (FAME) namely methyl palmitate, methyl stearate, methyl oleate, methyl linoleate, and methyl linolenate. The fraction of each component varies, depending on the feedstock and production process. Some of the earlier works considered biodiesel as single component with the properties calculated dynamically as a function of the mass fractions of individual components [65, 68]. Recently the concept of discrete component approach was used

to develop a combustion chemistry mechanism for biodiesel [69]. In another study, a discrete component vaporization model was developed by combining a single-component vaporization model and an improved drag model [70-72].

In addition to modeling biodiesel sprays, numerical modeling of biodiesel combustion is another active area of research. Biodiesel combustion was represented using global reactions in a previous study to predict NO_x emissions [73]. However, for accurate prediction of emissions, an approach based on detailed chemistry is necessary. Methyl butanoate mechanism was initially proposed as a biodiesel surrogate to model combustion [74, 75]. Some recent research works used methyl decanoate mechanism to model biodiesel combustion [76-79]. Computational results show that the mechanism was able to predict the biodiesel combustion characteristics in terms of ignition delay, in-cylinder pressure, and NO_x emissions. Because one of the drawbacks of biodiesel is high NO_x emissions, most of the computational research has concentrated on modeling NO_x [80, 81]. Some experimental studies indicated that soot emissions from biodiesel combustion are not negligible under certain engine conditions and strongly depend on the operating conditions and injection parameters [82, 83]. Thus, accurate soot models are required to predict the trend of soot emissions from biodiesel combustion.

2.8 Literature review on spray model improvements

Past research on soot modeling in diesel engines has proven that the emissions depend largely on the spray and flame structure in the engines [84]. Thus, it is important that the computational model is able to precisely capture the spray and fuel vapor distribution. An accurate simulation of spray involves Direct Numerical Simulation of liquid spray atomization and evaporation of atomized droplets [85]. Such a detailed simulation will be computationally expensive and not viable for day to day engineering applications. As an alternative to this, most

of the commercial CFD programs model liquid sprays using a Lagrangian approach where the spray droplets are tracked along its trajectory and the primary gas phase is modeled as Eulerian fluid [15-17]. The spray particles are assumed to be point masses which interact with the gas phase via mass, momentum and energy exchange as they travel through the gas phase. However, simplification of the physics used in this model gives rise to other problems such as low accuracy and grid dependency [86]. The standard evaporation model in used with Lagrangian droplets was found to under predict the vapor penetration at high ambient pressure conditions. In order to simulate diesel sprays accurately improvements were necessary to increase the vapor penetration.

Beard et al. was able to improve the vapor penetration by using a vapor particle approach [87]. This model was used in diesel engine simulations with limited success [88]. In this model, the liquid particles evaporate to generate vapor particles and the vapor particle transfer mass to the gas phase by laminar diffusion. However a fine grid was required in the fuel jet region to capture the fuel penetration. The vapor particle approach was further improved by adding gas jet model and also tracking the vapor particle further downstream after the liquid core is completely evaporated [89]. It was shown to improve the grid independency and vapor penetration. The model uses a cut-off distance based on grid size to release the vapor particles. This could pose a problem in practical engine simulations as the grid size could vary in the domain. Thus the vapor particle approach required further improvement in order to use in practical diesel spray applications.

CHAPTER 3. FUEL NO_x EMISSIONS FROM PRODUCER GAS COMBUSTION

3.1 Objectives

The objective of this study is to investigate the effects of producer gas composition, particularly ammonia, on fuel NO_x formation using CFD with detailed chemical kinetics. A reaction mechanism is developed to predict producer gas combustion and characterize the reaction pathways leading to NO_x emissions. The model will be validated using data obtained from a pilot-scale biomass gasification and combustion system. The current low NO_x burners available in industry are designed mainly for natural gas whose combustion mainly generates thermal NO_x emissions. Thus, it is important to design new burners that are adequate for producer gas. The model is used as a tool to recommend favorable operating conditions for low NO_x emissions from an industrial burner. Detailed analysis of the results will be performed to identify the NO_x formation and consumption regions in the burner, and based on these results a new burner design is suggested for reducing fuel NO_x emissions.

3.2 Producer Gas Reaction Mechanisms

Various syngas reaction mechanisms have been developed previously by different researchers [90-94]. Mechanisms vary in their reactions and characteristics such as ignition delay and laminar flame speed for the producer gas fuel. In this study, a one-dimensional plug flow reactor (PFR) study is performed using CHEMKIN [4] in order to compare four detailed mechanisms and their NO emissions. The diameter of the PFR is specified as 20 cm and the axial length as 400 cm so that it represents the physical dimensions of the present burner. Before the PFR, the fuel and air are mixed in an adiabatic gas mixer at the specified equivalence ratios. A heat rate of 70 kW, based on the lower heating value of fuel is used which is approximately the heat rate used in the actual burner. An initial temperature and inlet temperature of 1000 K is used

for the simulations. The PFR is kept at atmospheric pressure conditions. Steady-state conditions are simulated. It is assumed that the ignition delay is proportional to the axial distance before the mixture is ignited.

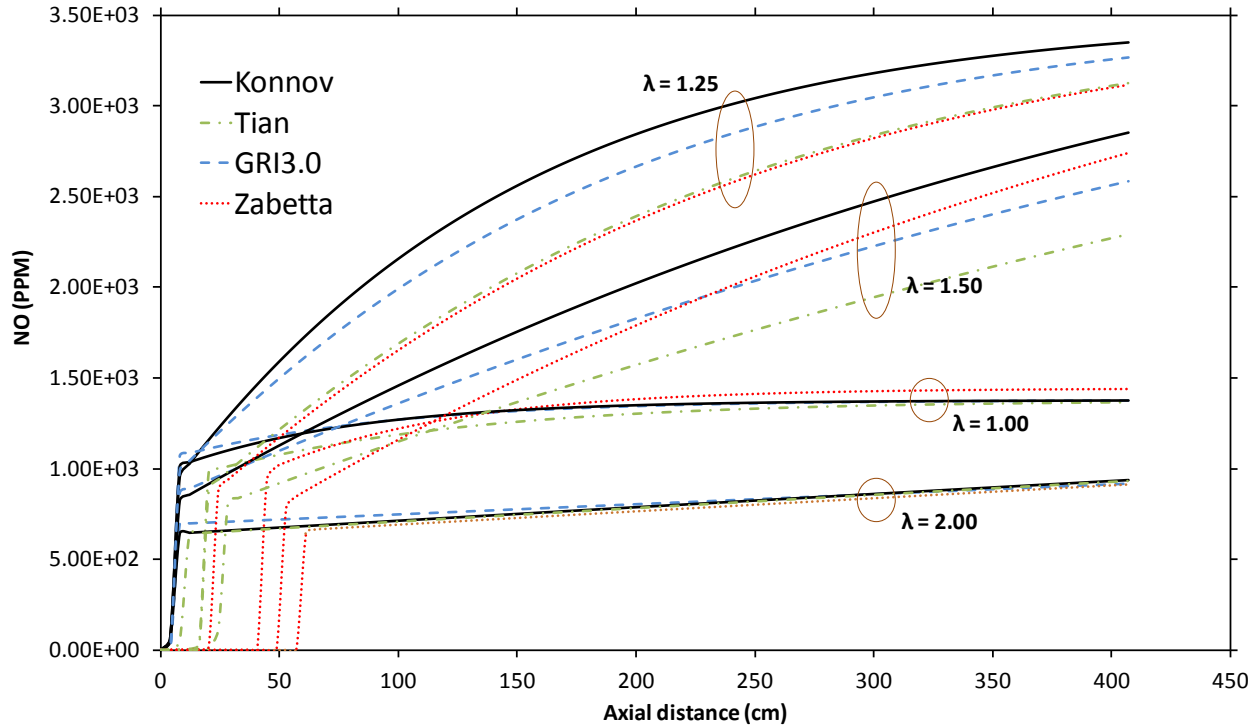


Figure 3.1 NO mole fraction evolutions predicted using different mechanisms in a plug flow reactor with wood+40% DDGS derived producer gas as fuel

The mechanisms in the decreasing order of number of reactions are Konnov [95], Tian [91], Zabetta [92] and GRI 3.0 [93] mechanisms. The producer gas composition derived from the mixture of wood and 40% dried distiller grain soluble is used as the fuel [33]. Figure 3.1 shows the NO mole fractions predicted by different mechanisms at different air equivalence ratios (λ), which is defined as the ratio of actual air-fuel ratio to stoichiometric air-fuel ratio. This parameter is used in this study since it is commonly used in the burner industry. It was observed that all the mechanisms predicted similar final NO emission levels, however, the predicted

ignition delays vary. The location of the sudden rise in NO levels coincides with the location of temperature rise and this represents the ignition location for each mechanism. Konnov mechanism (127 species and 1207 reactions) and GRI 3.0 mechanism (53 species and 325 reactions) have similar and shorter ignition delays, whereas Zabetta mechanism (60 species and 371 reactions) has the longest ignition delays. The differences in the mechanisms were arisen mainly due to the differences in the CH₄/H₂/CO chemistry. The contribution of small amount of ammonia is found to be insignificant in terms of heat release and ignition delay characteristics. GRI3.0, although validated extensively for natural gas, does not include a comprehensive NH₃ chemistry. Previous studies have shown that the NH₃ chemistries in GRI3.0, Konnov and Tian mechanisms differ, especially at high ammonia concentrations, i.e., ammonia is the main constituent of the fuel [96]. However, the results from PFR simulations show that the performances of these three reaction mechanisms are similar for low NH₃ concentration, which is the case in the producer gas studied here. Therefore, GRI 3.0 was chosen as the baseline mechanism for the 3D burner CFD simulation due to its consistency with the more comprehensive mechanism, smaller size, and extensive validation in literature.

3.3 Mechanism Reduction Method

A reduced form of GRI 3.0 is used to model producer gas combustion. GRI 3.0 was originally developed for methane combustion and it has been successfully used to model syngas and producer gas combustion [31, 97]. A CFD simulation to track all species and calculate all reactions of the complete mechanism would be computationally intensive. Thus, a reduced mechanism is developed for the current simulations. The objective of the reduced mechanism is to reproduce NO_x emissions, ignition delays and flame speeds similar to that predicted by GRI 3.0 full mechanism for producer gas fuel.

Among the 325 reactions of GRI 3.0 mechanism, not all contribute equally to the thermal and chemical changes occurring during combustion. CHEMKIN perfectly stirred reactor (PSR) simulations are conducted for producer gas at conditions similar to those inside the burner, and the results are analyzed to reduce the mechanism. A residence time 0.003 s is specified for the PSR. Initial temperature is kept at 600 K and the air equivalence ratio is varied from 0.5 to 1.5. A volume of 1000 cc and pressure of 1 atm are specified for the reactor. Adiabatic boundaries are used for the reactor. The fuel used is wood+40% DDGS syngas. The simulation is conducted using a transient solver for 0.02 s in which a steady state is attained. Figure 3.2 is an example plot showing the rate of production of hydrogen from different reactions in GRI 3.0

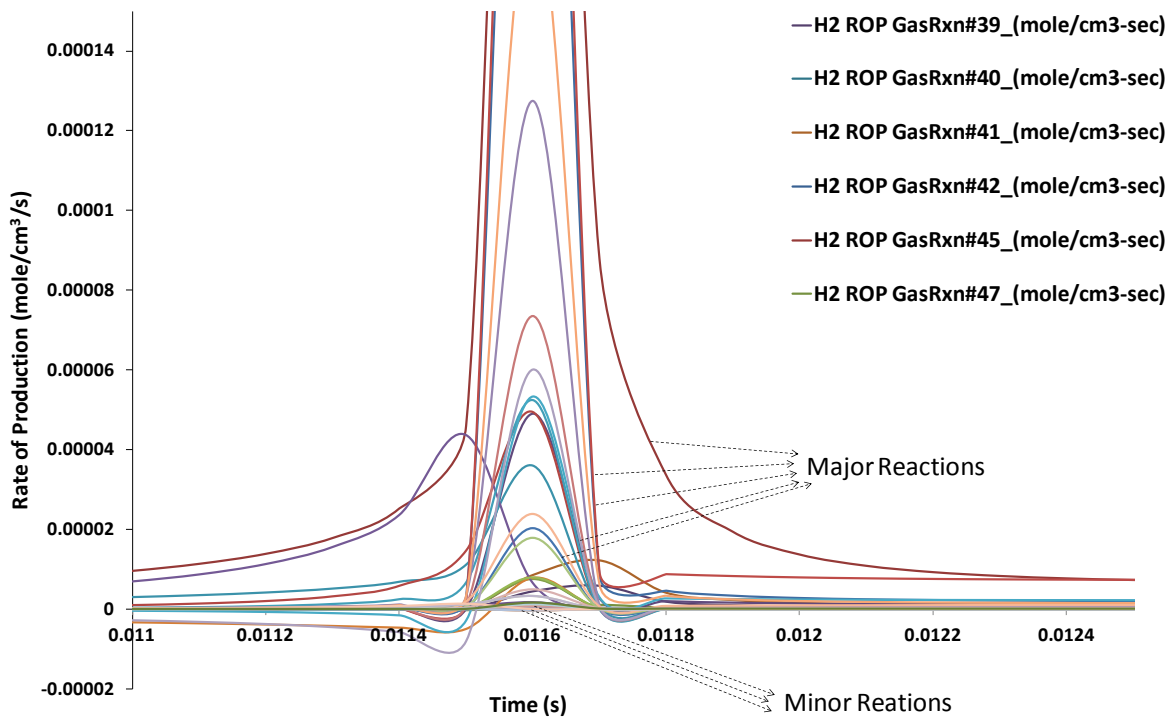


Figure 3.2 Rate of production of hydrogen reactions in a PSR with wood+40% DDGS derived producer gas as fuel

It can be seen that some of the reactions add very little to the rate of production or consumption of hydrogen. A similar plot of rate of change of enthalpy by each reaction reveals that many reactions do not have substantial impact on the thermal changes in the system. Neglecting such reactions will not have much effect on the reaction mechanism. The reactions to be neglected are identified by comparing the rate of production of species from each reaction to the maximum value of the rate of production of any species at the same time. Perfectly stirred reactor (PSR) calculations using CHEMKIN are performed using the full mechanism. Rate of productions (ROP) of each species from each reaction are exported at each time step from the CHEMKIN PSR model. The reactions for which the ROP of a species is less than a cut-off factor times the maximum ROP of any species at that time step are removed. Enthalpy changes of the removed reactions are compared against the reaction with the maximum enthalpy change to ensure that removing these reactions does not affect the thermal changes in combustion. The cut-off factor is iterated until the reduced mechanism produces similar results as that of the full mechanism in terms of ignition delay, flame-speed and NO mole fractions. Similar reduction techniques are previously used in other studies [98]. More rigorous methods for mechanism reduction are available in the literature such as direct relation graph [11] and computational singular perturbation [12]. In the current study the detailed reduction method is chosen for its ease of implementation.

The PSR results on three different air equivalence ratios 0.5, 1.0 and 2.0 are used to generate the new reaction set without the minor reactions. A cut-off factor of 0.01 was found to be most appropriate. The nitrogen pathway in the mechanism is only slightly reduced using a smaller cut-off because it is important to predict the NO_x correctly in this study. The reduced reaction mechanism is validated against the GRI 3.0 full mechanism for ignition delay and

laminar flame speed as shown in Figure 3.3 and Figure 3.4. The ignition delay is calculated as the time when the rate of change of temperature in the reactor is at its maximum. An additional validation is made to compare the NO species history predicted by the reduced mechanism and full mechanism as illustrated in Figure 3.5. In the PSR simulations for mechanism reduction, producer gas derived from “wood + 40% DDGS” is used as the fuel. The resulting reduced mechanism contains 36 species and 198 reactions. A speed up of 1.3 in CPU time was recorded with the reduced mechanism compared with the baseline mechanism.

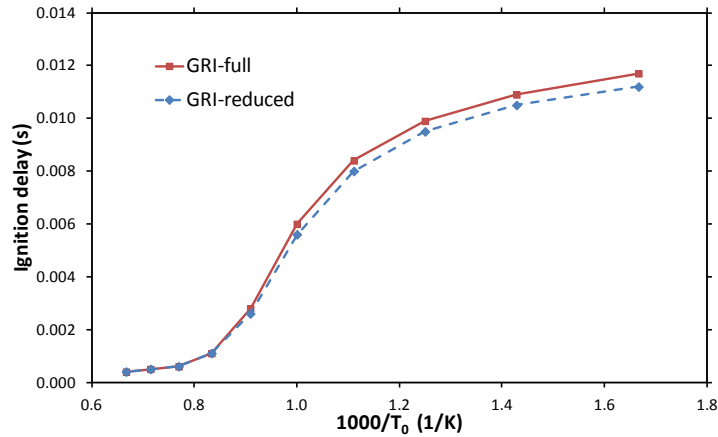


Figure 3.3 Ignition delay comparison of GRI-full mechanism and reduced mechanism ($\phi=1.0$, $p=1$ atm, fuel=wood+40% DDGS derived producer gas)

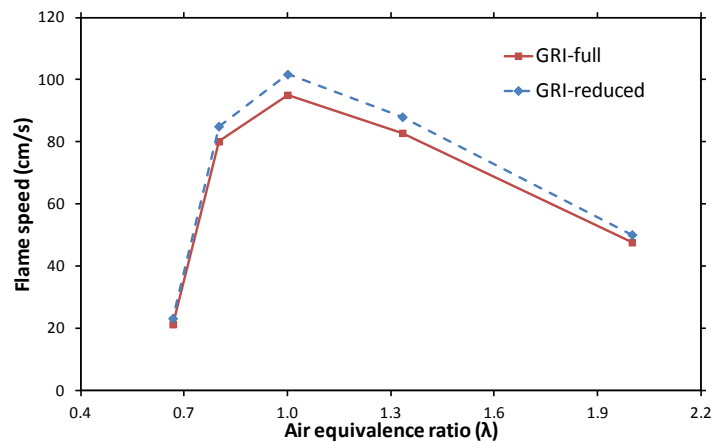


Figure 3.4 Comparison of laminar flame speed predicted using GRI 3.0 mechanism and the present reduced mechanism ($T_0=1000$ K, $p=1$ atm, fuel=wood+40% DDGS derived producer gas)

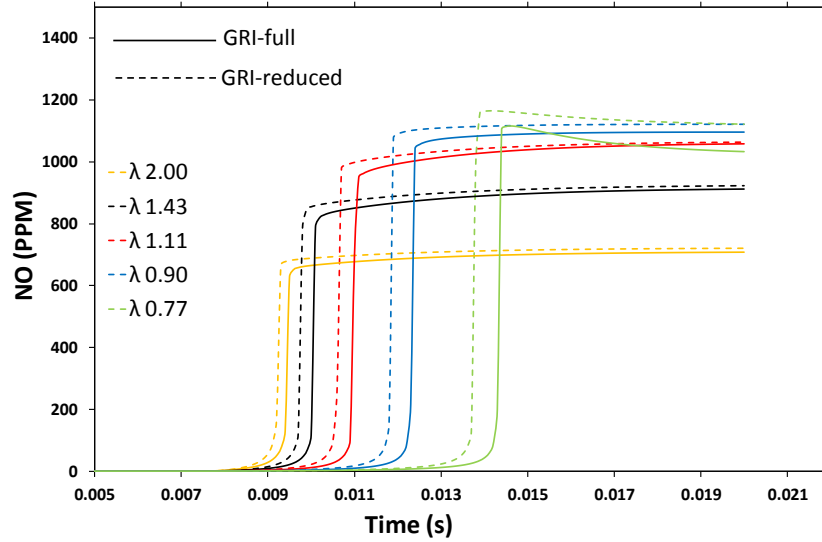


Figure 3.5 Comparison NO mole fractions predicted using GRI 3.0 mechanism and the present reduced mechanism ($T_0=600$ K, $p=1$ atm, fuel=wood+40% DDGS derived producer gas)

3.4 Model Details

The burner modeled in this study is an industrial burner rated at 879 kW thermal input. This burner is integrated into a pilot-scale biomass gasification system [33, 34]. The burner is an air-staged burner with four stages of fuel-air mixing. A schematic of a cut section view of burner is shown in Figure 3.6. Producer gas enters the center tube of the burner, and there are air holes at different locations to introduce air into the producer gas stream, which is the so-called staged combustion concept. As a result, the combustion is a combination of premixed and diffusion modes. The composition of the producer gas is obtained from a previous experimental study [33]. The biomass feedstocks used for gasification include wood, wood with 13% DDGS, and wood with 40% DDGS. Dried distiller grain soluble (DDGS) contains a high amount of fixed nitrogen. In general, wood has relatively low nitrogen content, and hence the ammonia present in the producer gas is low. DDGS is purposely added to wood powder and made into pellets to increase the nitrogen content in feedstock, which in turn increases the ammonia concentration in

the producer gas. In the simulations, the higher order hydrocarbons, which are of very low concentration, are lumped into methane volume fraction in order to reduce the complexity of the model. The producer gas composition for each biomass feedstock is shown in Table 3.1. The species composition presented in the table is in wet volume percentage.

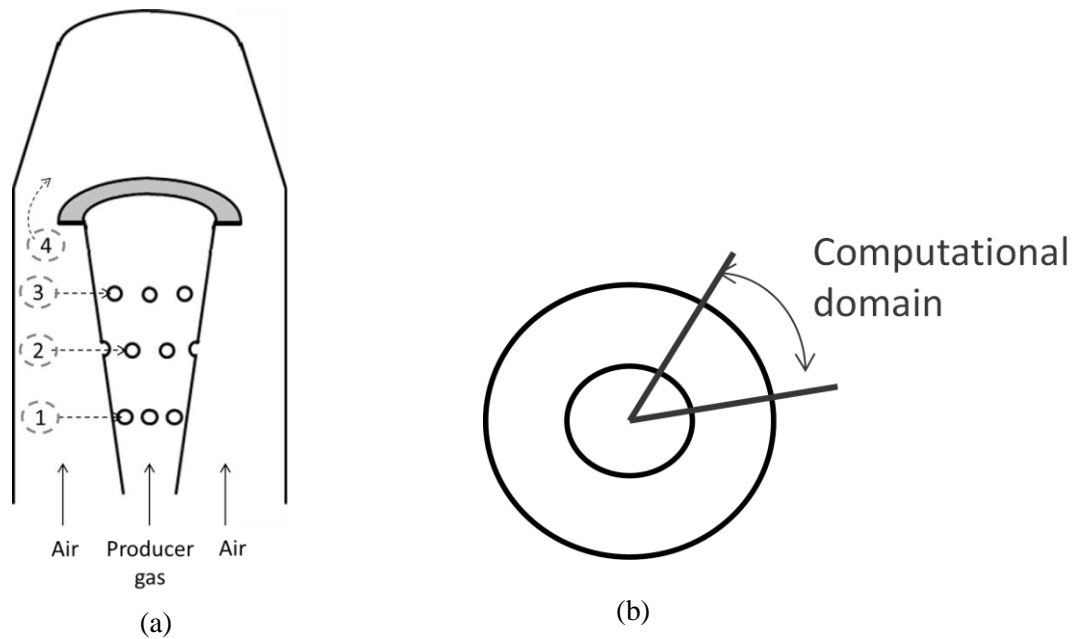


Figure 3.6 Schematic of the burner used for producer gas combustion: (a) cross-sectional view through the centerline, (b) bottom view, showing the 45-degree sector computational domain.

Steady-state turbulent combustion is modeled using ANSYS FLUENT [99] together with the SST- $k\omega$ model for turbulence and the eddy-dissipation concept (EDC) for modeling turbulence-chemistry interaction. The EDC model allows one to model detailed chemical kinetic reactions in a turbulent flame. This model assumes that the reaction occurs in small turbulent scales in space and time [6]. The reaction rates which are governed by Arrhenius equations are calculated over these scales and integrated using an ISAT algorithm [100] to calculate the

combustion rate of each species from the reaction mechanism. The computational domain is a 3D sector of the burner and combustion chamber with rotational periodic boundary conditions. Figure 3.7 shows an image of the computational mesh. The mesh consists of 800,000 cells with most regions meshed using hexahedral cells. The holes used for air staging are meshed using conformal tetrahedral cells. The fuel flow rate and air flow rate at the mass flow inlet boundaries are varied based on the heat rate and air equivalence ratio used in the experiments. The outlet is at 4 m from the bottom of combustion chamber where the exhaust emission measurements are made. In simulations, a pressure outlet boundary condition with atmospheric pressure is specified here. The walls of the combustion chamber are modeled using convection heat transfer boundary conditions with a temperature of 20° C and a convection coefficient of 40 W/mK, which corresponds to the ambient wind conditions.

Table 3.1 Major Species composition (vol%) of producer gas for different biomass feedstocks

% wet volumetric basis			
Producer gas component	Wood	Wood + 13% DDGS	Wood + 40% DDGS
CH ₄	6.85	7.42	7.66
CO	16.91	16.26	12.55
CO ₂	13.56	14.88	12.87
H ₂	11.33	10.46	7.01
H ₂ O	9.97	10.64	18.63
N ₂	41.32	40.16	41.04
NH ₃	0.06	0.18	0.24

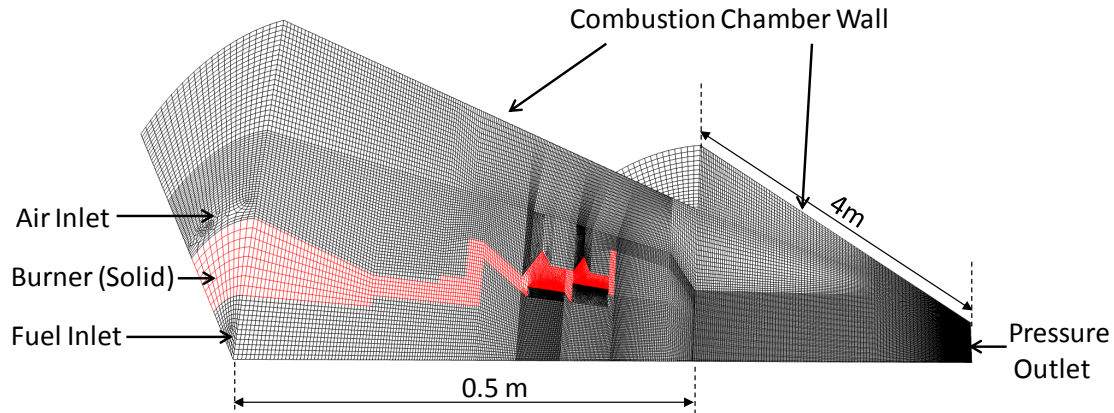


Figure 3.7 Computational mesh of the burner (within 0.5 m) and combustion chamber. Note that the scale is not linear.

The simulations are carried out using the first-order upwind scheme until steady-state results are obtained. The normalized residuals converge to 10^{-3} levels. Each simulation is performed parallel on eight processors and the average wall clock time for a simulation is approximately 600 hours. The NO emissions at the outlet boundary are compared with the experiment results. Further detailed analysis of NO_x forming regions and their corresponding combustion conditions are conducted, as described in the following sections.

3.5 Grid Dependence Study

Grid dependence study of the burner model is conducted using three sets of meshes with increasing mesh density. A 2D axi-symmetric assumption was used to speed up the computation. Mesh density was varied with 50 (coarse), 100 (baseline) and 200 (fine) grid points at the exit of burner nozzle. The simulations were performed using wood+40% DDGS-derived producer gas with an equivalence ratio of 1.6. NO mole fractions at burner exit were compared, as shown in Figure 3.8. It was observed that the coarse mesh predicted the peak NO region slightly shifted away from the burner axis. The NO emissions at outlet from the three cases from lower grid

density to higher grid density were 261, 306 and 317 parts per million (ppm), respectively. The baseline and fine-mesh results were close to each other in terms of the distribution and the peak value. Thus, the baseline mesh sizing was used for the future 3-D simulations in this study.

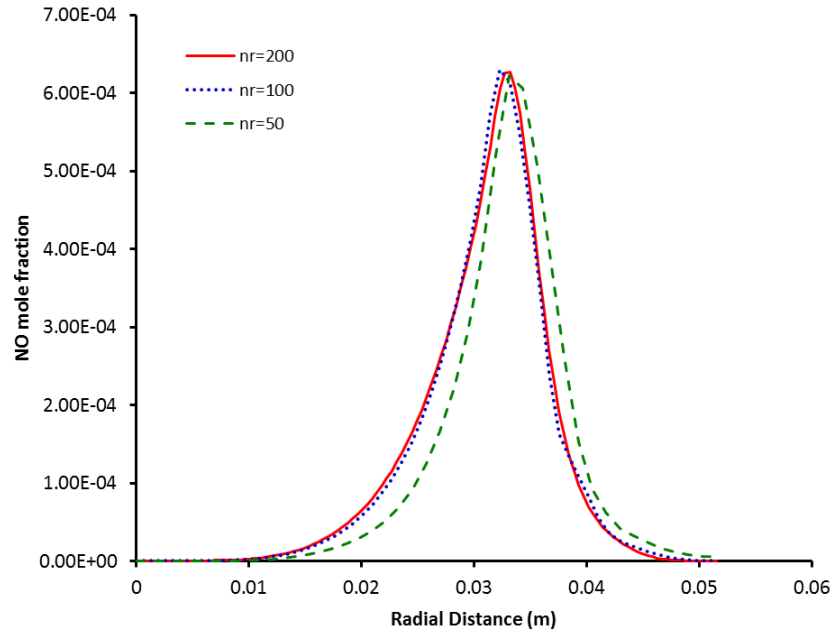


Figure 3.8 NO mole fractions at the burner nozzle exit using different meshes

3.6 Burner Simulation Results

Simulations are performed for a range of air equivalence ratios (λ) varying from 1.05 to 2.5 based on the experimental conditions. From the experiments, it was observed that the NO_x levels are less sensitive to the heat rate. Thus only low heat rate experiments are chosen for the numerical study. The simulation test matrix is listed in Table 3.2. The experiments are designed to study the effect of air equivalence ratio and ammonia concentration in producer gas on NO_x emissions. The measurement of total fixed nitrogen (TFN) is typically used in the industry to account for the net NO_x emissions. TFN includes all nitrogen-containing species except molecular nitrogen. From the simulations, it was observed that NO is the major component of

emissions at the outlet. The rest of the other nitrogen-containing compounds accounted for only less than 1/100 of NO concentration. Thus, only NO concentration at the outlet is used in the simulations to represent the NO_x emissions.

Table 3.2 Operating conditions for simulations

Biomass Feedstock	Heat Rate (kW)	Air Equivalence Ratio (λ)			
		1.36	1.60	2.00	2.50
Wood	70.2	1.36	1.60	2.00	2.50
Wood + 13% DDGS	71.72	1.16	1.31	1.54	1.68
Wood + 40% DDGS	56.87	1.05	1.19	1.32	1.60

Mass weighted average of NO in ppm at the pressure outlet boundary is used to compare with experimental results. NO_x emissions are normalized to the 3% oxygen level at exhaust using the following formula, which is commonly used in industry to correct for the dilution effect.

$$\text{NO}_x @ 3\% \text{O}_2 = \text{NO}_{x, \text{raw data}} \times \frac{1 - 0.03}{1 - \frac{\% \text{O}_2}{100}} \quad (3.1)$$

Figure 3.9 shows the comparison of measured and predicted NO_x emissions at the outlet. It can be seen that a very good level of agreement is obtained, especially at lean conditions (i.e., high λ). NO_x emissions increase for producer gas with high ammonia content, e.g. mixtures of wood and DDGS. The present model is able to capture the trend and predict the effects of feedstock on NO_x emissions. For wood and wood+13% DDGS cases, as the air equivalence

ratio approaches unity (i.e. fuel rich), the model is able to predict slight increase in NO_x emission. For wood+40% DDGS cases that have relatively high ammonia concentration, as the conditions approaches stoichiometric, the model predicts an increase in NO_x emission whereas the experiments show a decrease. One possible reason could be the limitation in the reaction mechanism at rich conditions. Figure 3.1 shows that there are larger variations in NO predictions using different reaction mechanisms when the NO emissions are high. Thus, it is thought that there are more uncertainties in the reaction mechanism under these conditions. Nonetheless it could be observed from both experiment and simulation results that NO_x emissions are more sensitive to the ammonia content in producer gas than air equivalence ratio.

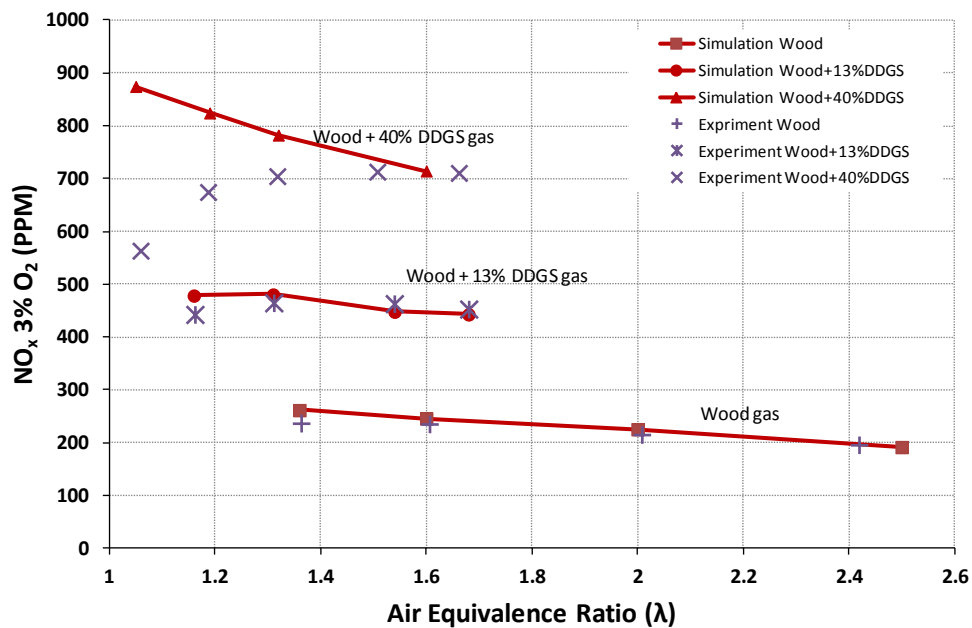


Figure 3.9 NO_x emissions measured (lines) [33] and predicted (symbols) using the reduced mechanism

It should be noted that practical burners always operate at a fuel lean condition to ensure complete combustion. Thus, the present model proves to perform relatively well under regular operating conditions. Moreover, the wood+40%DDGS mixture produces a relatively high

ammonia concentration in producer gas, much higher than regular biomass feedstock [40]. Overall, the good agreement for wood and wood+13% DDGS indicates that the present model is able to predict combustion and NO_x emissions using biomass-derived producer gas

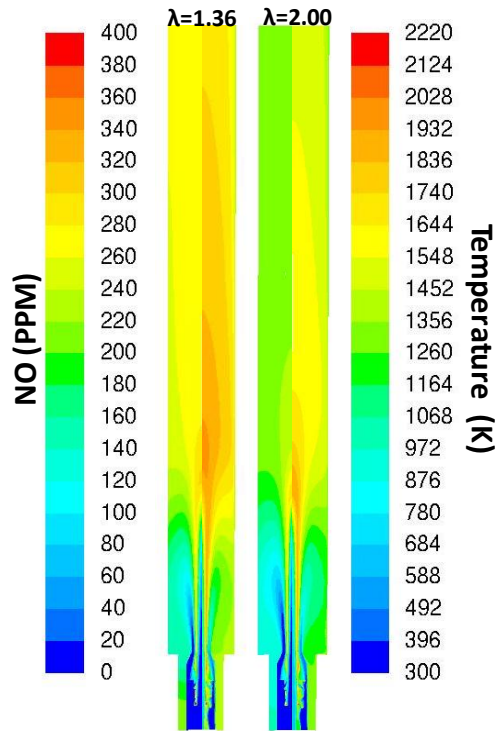


Figure 3.10 Contours of NO (left half of each plot) and temperature (right half) of producer gas combustion derived from wood

Figure 3.10, 3.11 and 3.12 show the contours of NO and temperature on a cut plane from the mid-section of the sector mesh. The temperature contour represents the approximate flame structure. The core of the flame consists of unburned fuel and air is outside the flame. It can be seen that as the air equivalence ratio increases (i.e., higher λ), the flame region becomes smaller. The NO mole fraction contours also follow the flame structure. The decreasing NO emissions with higher air equivalence ratios is associated with the flame length. NO mole fraction is high in

the high temperature zones inside the flame. At the location where the flame converges, both temperature and NO mole fractions are high. Downstream this location, there is no NO production or consumption. The flame starts from stage 1, where air first mixes with fuel (see Fig. 6). The peak temperatures in most of the cases are approximately 2,200 K and are located in the flame near stage 1 and stage 2 of the burner where high mixing occurs. The peak NO mole fraction and NO production rate were also observed at this location.

Due to the low amount of H₂ and CO in the producer gas from the wood+40%DDGS mixture, the lower heating value (LHV) of this fuel is low compared to the other two fuel gases. As a result, the flame temperature of wood+40%DDGS-derived producer gas is lower than those of the other cases. However, the higher amount of NH₃ present in the gas raises the NO_x emissions.

A closer look of the flame is shown in Figure 3.13. It displays the cut-section view of wood+13%DDGS producer gas flame with air equivalence ratio 1.54. It can be seen that most of the NO reactions takes place in a thin region along the flame. As the producer gas moves from fuel inlet to upwards, alternate NO generating and NO consuming regions are seen inside the burner. Outside the burner, the NO generating region is seen at the outer side of the flame and the NO consuming region is seen at the inner side of the flame. The contour shown in Figure 3.13 is the net NO reaction rate, which is the sum of NO reaction rates from all reactions involving NO. The burner region can be identified as the region below the converging section in the temperature contours in the figure.

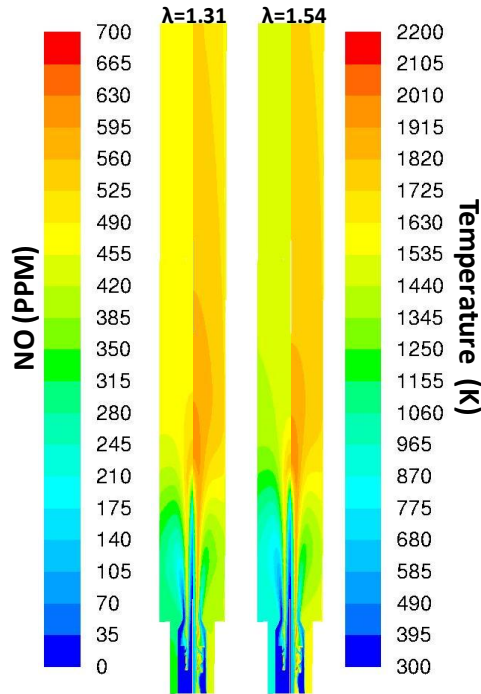


Figure 3.11 Contours of NO (left half) and temperature (right half) of producer gas combustion derived from wood + 13% DDGS

In order to find the reactions that help reduce NO, it is necessary to look into the details of each reaction. Figure 3.14 compares the net effect of each NO containing reaction for different feedstocks at air equivalence ratio close to 1.60. The net reaction rate of each reaction is obtained as a volume integral of the reaction rate over the entire domain. As the ammonia content in the fuel increases, the reaction rate of each reaction increases. The four most prominent reactions are reactions between NO and NO₂. These are also the only four reactions involving NO₂. Two of these reactions generate NO and the other two convert NO to NO₂. These reactions occur outside the burner and are spread almost to the entire flame region. NO₂ to NO conversion is the most prominent reaction among these. As a result, the mass of net NO in the domain is about 100 times more than net NO₂ present. The NO generation from atomic nitrogen forms the set of second most prominent reactions among NO reactions. Atomic nitrogen is mainly formed from

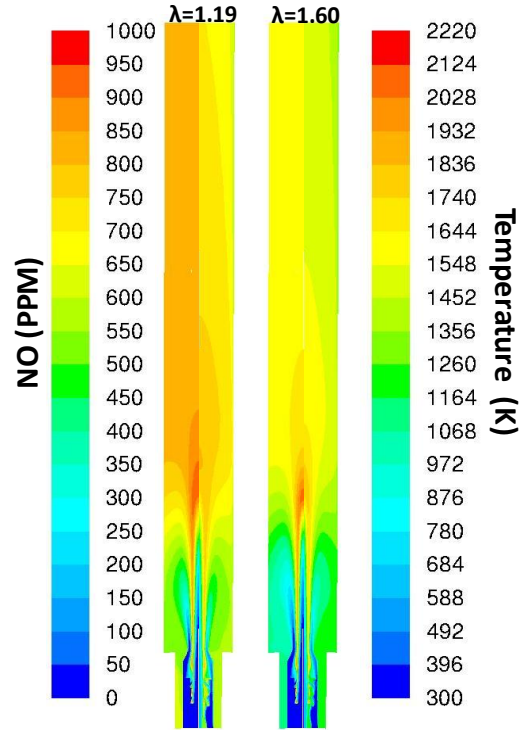


Figure 3.12 Contours of NO (left half) and temperature (right half) of producer gas combustion derived from wood + 40% DDGS

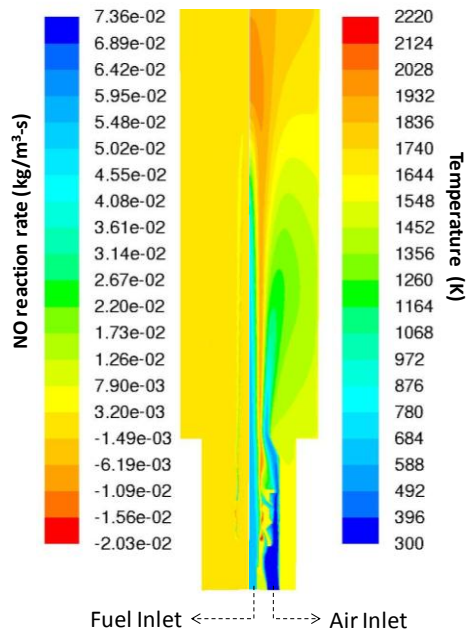


Figure 3.13 NO reaction rate contours (left half) and Temperature contours (right half) in the flame region ($\lambda=1.54$, wood+13% DDGS gas)

amine radicals evolved from ammonia dissociation. Therefore, the main pathway of NO formation is from $\text{NH}_3 \rightarrow \text{NH} \rightarrow \text{N} \rightarrow \text{NO}$. Atomic nitrogen reacts with O_2 , OH and CO_2 to form NO. Amine radicals also react directly with atomic oxygen to form NO.

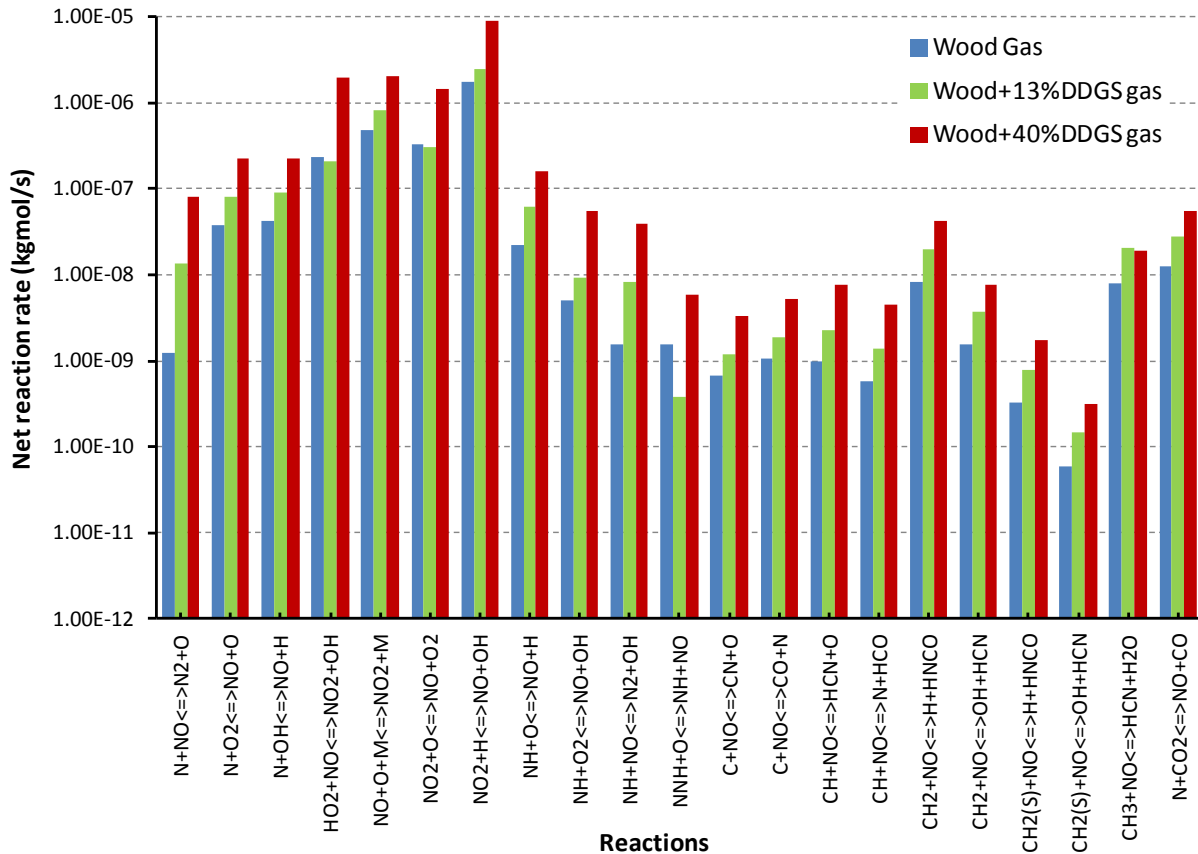


Figure 3.14 Net reaction rates of each NO reaction in the domain with different producer gas composition at λ approximately equal to 1.6

Further analysis of these reaction rate data shows that these reactions occur in a thin region along the flame, inside and outside the burner. The reaction rates are much higher inside the burner. Another major set of reactions are the reactions of NO with hydrocarbons. In the presence of hydrocarbon radicals such as CH_3 , CH_2 , $\text{CH}_2(\text{s})$ and CH , NO is converted to HCN, HNCO and HCN molecules. Among these, CH_3 and CH_2 reactions are present both inside and

outside the burner, along the flame. CH reactions are contained mainly inside the burner. $\text{CH}_2(\text{s})$ reactions are present both inside and outside, however, the reaction rates are much lower than other reactions. The main NO reducing reaction, or de- NO_x reaction, is the reaction of NO with nitrogen atom to form N_2 . This is the reverse reaction of thermal NO_x generation. It can be seen from Figure 3.14 that the net de- NO_x reaction rates are positive. So more NO is converted to N_2 than thermal NO_x generated. This reaction is also present both inside and outside the burner, but with higher reaction rates inside the burner. A region of thermal NO_x generation is also observed at the flame tip, which is a high temperature zone with temperature above 2000 K. Additionally, patches of thermal NO_x regions are observed in the high temperature zones near the first and second stages of burner.

Although the $\text{NO} \leftrightarrow \text{NO}_2$ reactions have the highest net reaction rates, these reactions do not contribute in generating or reducing NO_x . The NO production from atomic nitrogen and amine and the NO consuming reactions, such as NO conversion to N_2 and NO reduction in the presence of hydrocarbons, are the major reactions which determine the net NO_x emissions. In order to understand the conditions at which these reactions occur, a temperature-equivalence ratio (ER) map is generated. Figure 3.15 shows a temperature-ER map of the net NO reaction rate of a case using wood+13%DDGS producer gas with $\lambda=1.54$. Note that in order to indicate the mixture condition, the equivalence ratio (ER) is calculated based on methane and oxygen content in the computational cell. The methane equivalence ratio (MER) is calculated using the following formula.

$$\text{MER} = 4 \times \frac{X_{\text{CH}_4}}{X_{\text{O}_2}} \quad (3.2)$$

X represents the mass fraction of the species and 4 is the stoichiometric oxygen-fuel ratio for methane on mass basis. At the core of the flame, the oxygen mass fraction decreases and CH_4 mass fraction increases. As a result, methane MER will have very high values at the core of the flame.

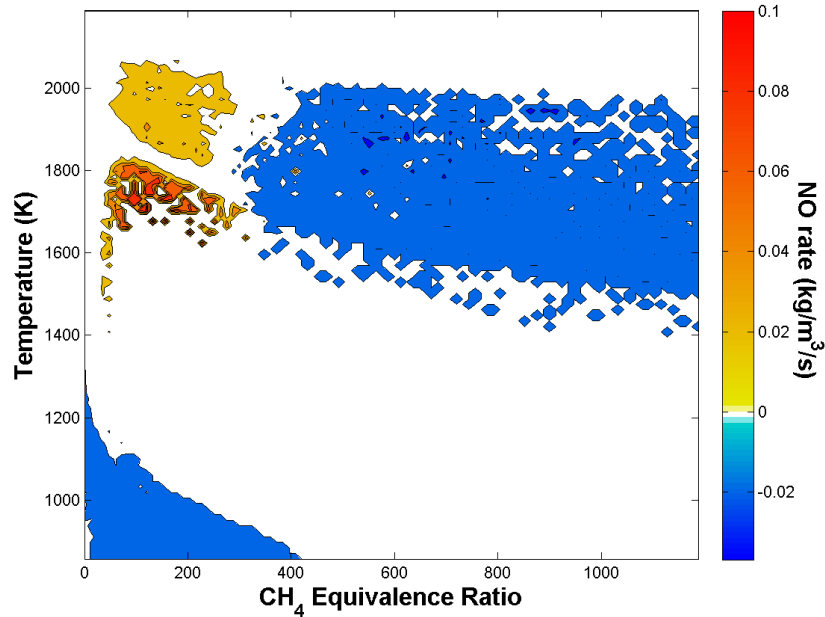


Figure 3.15 Temperature-MER map of net NO rate in wood+13%DDGS gas combustion at $\lambda=1.54$

The color contours in Figure 3.15 represent NO reaction rates at different temperature and MER conditions. A positive value indicates NO production and negative value indicates NO consumption. A wide range of NO consumption can be seen on the map, whereas net NO production is confined to a smaller region of temperature-MER conditions. However, the NO production rates are higher than NO consumption rates.

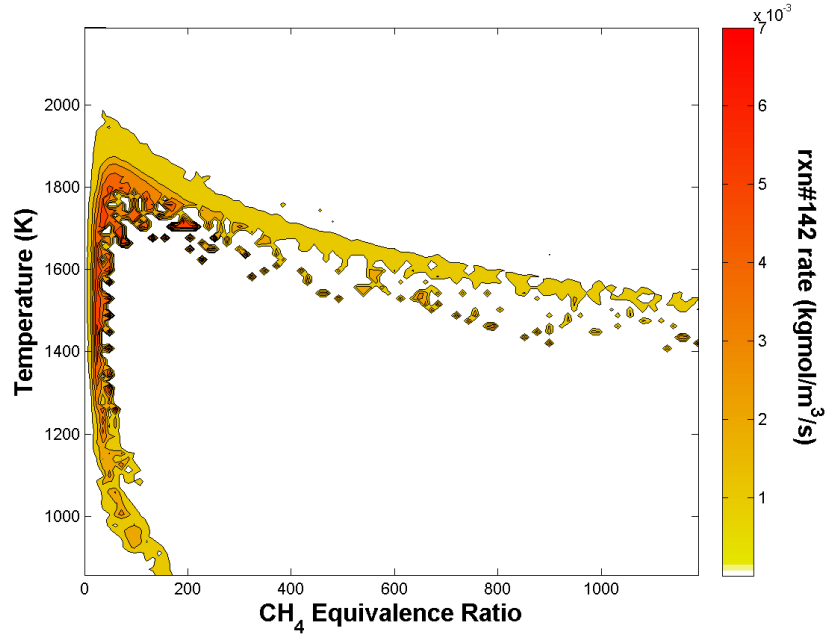


Figure 3.16 Temperature-MER map of the reaction rate of $\text{NO}_2+\text{H} \rightleftharpoons \text{NO}+\text{OH}$ in wood+13%DDGS (reaction#142) gas combustion at $\lambda=1.54$

Figure 3.16 to Figure 3.21 show the contribution of different reactions to the net NO rate. The kinetic rate of each reaction is mapped against local temperature and MER conditions. Reactions #142, 143 and 191 are NO producing reactions and reactions #136, 139 and 181 are NO consuming reactions. The numbered reactions are listed in the Appendix A. The NO producing region at 1,800 K and 200 MER seen in Figure 3.15, is mainly caused by NO_2 to NO reactions, which are not the primary NO generating reactions. The NO production map from NH and N is shown in Figure 3.17 and Figure 3.18, respectively. These reactions occur at slightly rich conditions about 200–600 methane equivalence ratio and at temperatures of 1,800–1,900 K. As the flame length increases, this region also increases which in turn increases the NO production. This effect can be seen as the increasing NO emissions with decreasing air equivalence ratio.

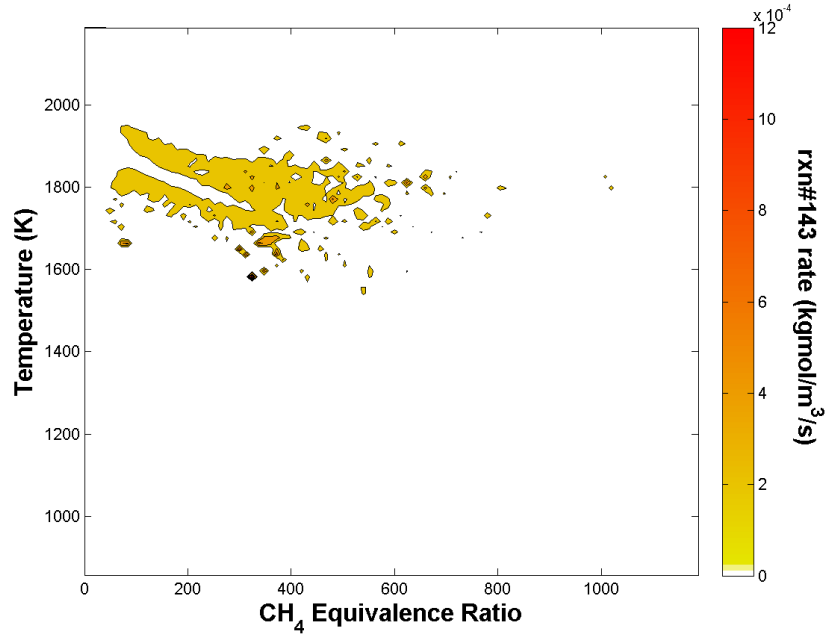


Figure 3.17 Temperature-MER map of the reaction rate of $\text{NH} + \text{O} \leftrightarrow \text{NO} + \text{H}$ in wood+13%DDGS (reaction#143) gas combustion at $\lambda=1.54$

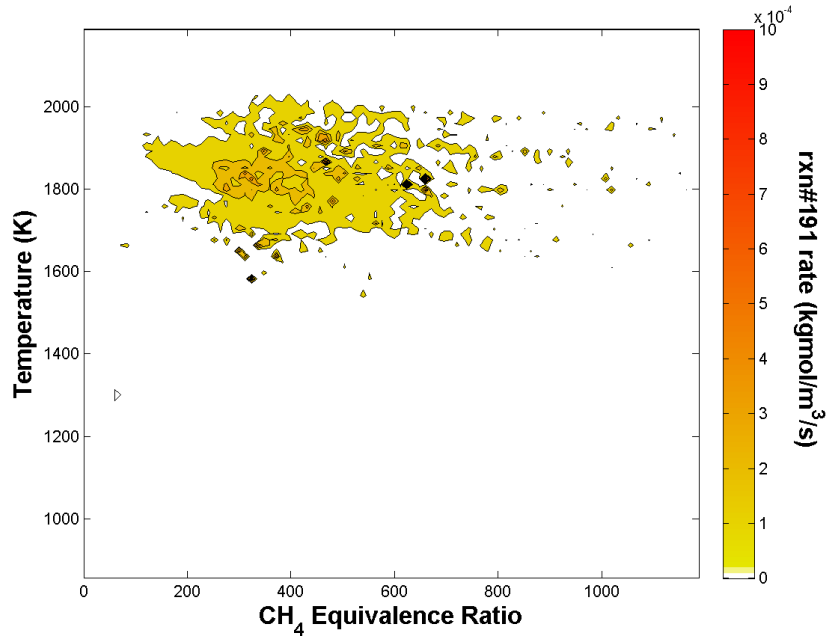


Figure 3.18 Temperature-MER map of the reaction rate of $\text{N} + \text{CO}_2 \leftrightarrow \text{NO} + \text{CO}$ in wood+13%DDGS (reaction#191) gas combustion at $\lambda=1.54$

The temperature-MER map in Figure 3.19 shows that the de-NO_x reaction which converts NO to N₂ occurs at almost the same temperature and ER conditions. A small amount of thermal NO_x production can be seen at higher temperatures and fuel lean mixture conditions, which can be seen as negative rate in Figure 3.19. At further fuel rich conditions, NO reduction occurs in the presence of hydrocarbon radicals such as CH₃ as can be seen in Figure 3.20. The NO consumption observed at low temperatures between 1,200 K and 1,000 K and ER less than 400 is the conversion of NO to NO₂, as seen in Figure 3.21. This reaction does not help in reducing NO, as NO₂ will be converted back to NO. Figure 3.22 shows the temperature-MER map for NO generating and consuming reactions, excluding the NO \leftrightarrow NO₂ interchanges. The conditions for NO production and NO consumption can be clearly identified from this map. So the main strategy for NO reduction in producer gas combustion is the reduction in the presence of hydrocarbon radicals. In the presence of hydrocarbon radicals such as CH, CH₂, CH₂(s) and CH₃, NO is converted to HCN. In rich conditions, HCN reacts with NH and N radicals to form N₂. Another reaction occurring in the fuel rich region is the conversion of NO to N₂ in the presence of NH radicals. These alternate de-NO_x pathways would help reduce NO emissions. In order to make use of these NO reduction pathways, it is preferable that main combustion takes place at richer conditions to reduce the NO formed by reacting with intermediate combustion products.

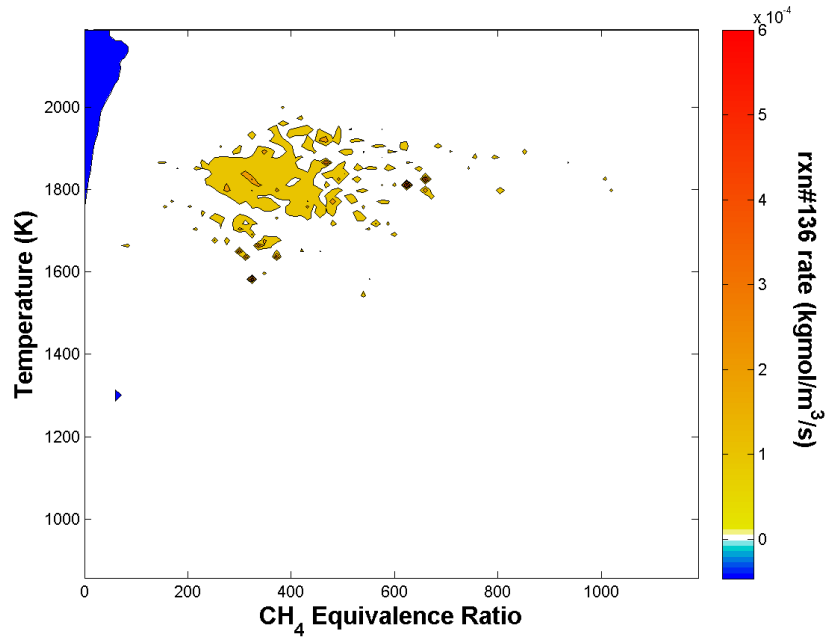


Figure 3.19 Temperature-MER map of the reaction rate of $\text{N}+\text{NO} \rightleftharpoons \text{N}_2+\text{O}$ in wood+13%DDGS (reaction#136) gas combustion at $\lambda=1.54$

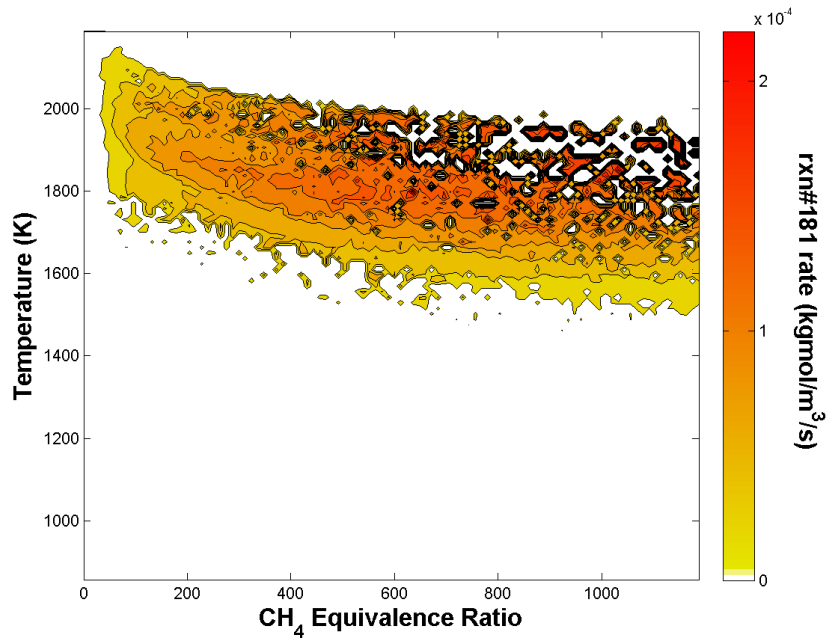


Figure 3.20 Temperature-MER map of the reaction rate of $\text{CH}_3+\text{NO} \rightleftharpoons \text{HCN}+\text{H}_2\text{O}$ (reaction#181) in wood+13%DDGS gas combustion at $\lambda=1.54$

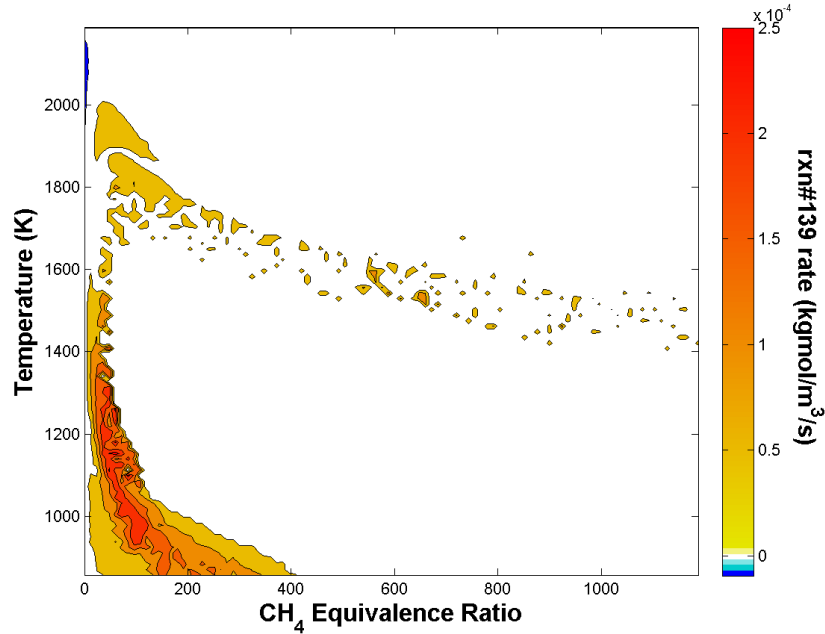


Figure 3.21 Temperature-MER map of the reaction rate of $\text{HO}_2+\text{NO} \rightleftharpoons \text{NO}_2+\text{OH}$ (reaction#139) in wood+13%DDGS gas combustion at $\lambda=1.54$

In the present burner, the air-staged design can help reduce some of the NO that is produced in the earlier stages. As NO molecules, which are produced in stages 1, 2 and 3, pass through the fuel rich regions downstream, they are converted to HCN by the hydrocarbon radicals. However, beyond the burner region, the local conditions become leaner and more NO is produced. In order to reduce NO produced beyond the burner, it is necessary to design the flame structure in such a way that NO molecules pass through a fuel rich region where hydrocarbons and NH radicals are present, which can reduce NO. One method to achieve this is to generate a diverging flame as opposed to the present converging flame. This can be done by obstructing the nozzle jet flow using a bluff body. As the flow passes around the bluff body, the flame will be diverged and NO produced in the lean regions upstream will pass through the rich regions in the diverging section. The bluff body also generates recirculation zones in the flame which

enhances the mixing of NO with the hydrocarbon radicals. Such a flame could potentially promote the de-NO_x pathways and reduce exhaust NO emissions.

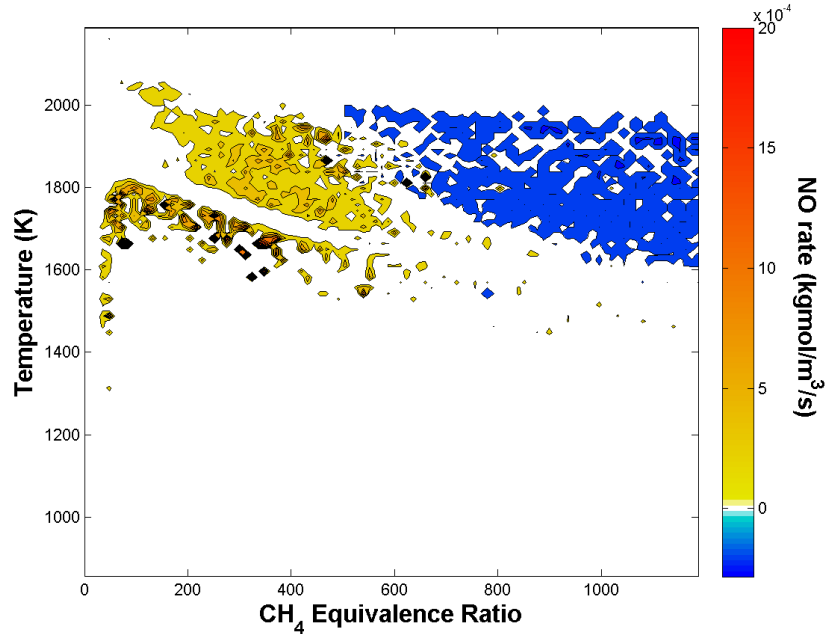


Figure 3.22 Temperature-MER map of NO production/consumption rate in wood+13%DDGS gas combustion at $\lambda=1.54$

3.7 Designing Low NO_x Burners

The producer gas combustion mechanism developed in this study is further used to design burners that can result in low fuel NO_x emissions. From the analysis of the previous section, it was observed that if the NO produced is passed through a high temperature zone, it could be converted to other compounds. The study suggests that a diverging flame can achieve this as the NO produced in the lower part of flame will pass through the upper diverging part of the flame. Other designs for achieving this condition include adding more air staging and generating recirculation. More air stages in the burner will help with faster conversion of NH₃ to NO inside the burner itself. As the NO produced inside the burner passes through the flame

outside of it, NO reduction can take place. By generating recirculation regions near the flames, the NO produced in the flame can be circulated back into the flame thereby reducing the final NO_x emissions. In order to investigate these concepts, three new designs were considered.

Figure 3.23 shows the schematic of three new designs investigated, namely D2, D3 and D4. The simulation results using the new designs were compared with the original burner design (D1), the schematic of which is shown in Figure 3.6. A 2D axi-symmetric approximation of the burner is considered in order to reduce the computational expense of the numerical investigations. All the four designs were modeled using a producer gas composition of wood+40%DDGS at an air equivalence ratio of 1.6. Other models in the simulation were kept the same as that of the 3D simulations discussed in Section 3.4.

From the simulations, it was evident that the new designs generated lower NO emissions than the original burner design. The original D1 model generated 322 PPM NO_x at 3% O₂ level. Notice that this result is different from the one obtained from the 3D simulation for the same burner. This difference could be because of the 2D-axisymmetric approximation used in this design study. It is observed that the 3D simulations were more accurate in predicting the turbulent mixing effects. However for this design investigation, 3D simulations of the prospective burners were found to be extremely slow. Thus 2D models were used with the assumption that the 2D simulations are able to predict the trends correctly. Figure 3.24 shows the temperature and NO mole fraction contours using different burner designs. The difference in flame structure can be observed from the temperature contours. D1 and D2 flames are very similar as the additional air stages provided are inside the burner. These additional air stages do not affect the mixing outside of burner. However, the mixing and flame structure inside of burner is different in D1 and D2. The alternate air streams helps in converting NH₃ to NO inside the

burner itself, which is further converted to other compounds as it travels through the flame in the chamber. A 13% reduction of NO at the outlet was observed with design D2. This strategy was found effective in converting the nitrogen content in fuel gas to N_2 at the outlet. In design D3, the flame curved around the bluff body generating a broader flame beyond the bluff body.

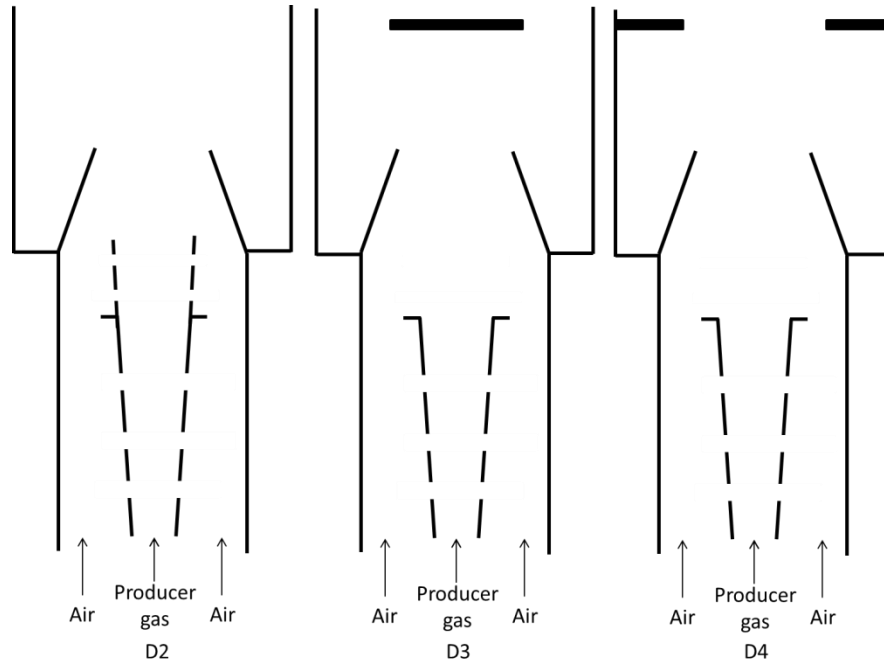


Figure 3.23 Schematic of the three new burner designs (D2: with additional air stages, D3: with bluff body, D4: with constricted flame for recirculation)

Downstream the bluff body a recirculation zone was formed which resulted in a longer residence time for the reacting species. This resulted in NO molecules to pass through the high temperature reactive zone for a longer time, where they are converted to other compounds. A greater reduction of 23% in NO emissions was observed with design D3. Design D4 generated recirculation zones before and after the constriction. However these recirculation zones were not effective in reducing the NO molecules as it was occurring mainly outside the flame region. As a

result the reduction was only 3%. Figure 3.25 shows the NO_x emissions at the outlet for the different designs.

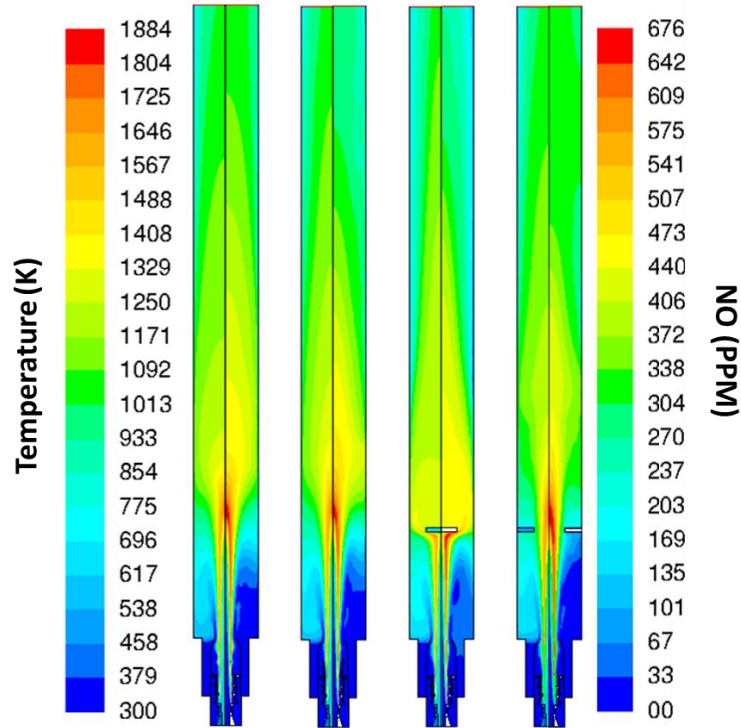


Figure 3.24 Temperature (Left) and NO mole fraction (Right) contours on different burner designs

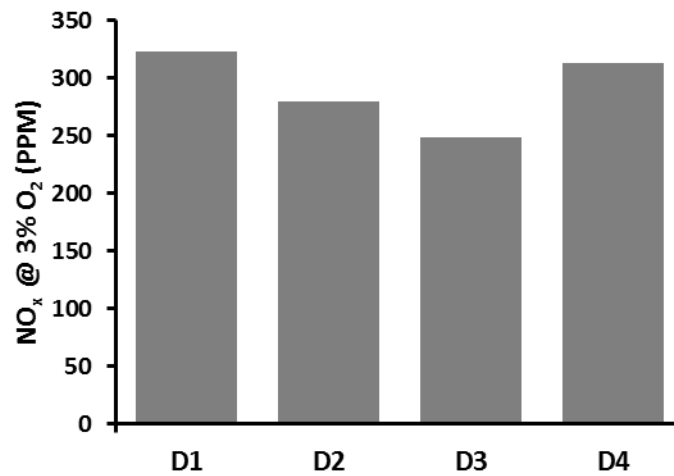


Figure 3.25 Predicted NO emissions using D1-D4 burner designs

3.7 Summary

Combustion simulations of biomass-derived producer gas in an industrial burner are performed in this work. A chemical reaction mechanism is developed for predicting NO_x emissions for different feedstocks and operating conditions. The simulation results were compared with the experimental data obtained from a pilot-scale gasification and combustion system. The mechanism is able to capture the NO_x levels and trends resulting from different ammonia contents in producer gas. The reduction in NO_x emissions at fuel lean conditions is able to be explained based on the flame structure observed from the simulations.

The present model is also able to provide insights into the combustion phenomena occurring inside the burner and combustion chamber and its effect on NO_x emissions. A thorough analysis of simulation results is carried out to provide the details of each reaction occurring in the flame. Results show that NO to NO_2 and NO_2 to NO reactions are very prominent. However, the major NO producing reactions are the oxidation of NH and N at slightly rich conditions and temperatures over 1700 K. The de- NO_x reaction where NO is converted to N_2 by reacting with N atom also occurs at the same conditions. The alternate de- NO_x pathway, which can be more useful in reducing NO_x emissions, occurs at richer conditions and temperatures over 1700 K. Under these conditions, NO reacts with hydrocarbon radicals and NH to form HCN and N_2 , respectively. HCN can be further converted to N_2 or NO depending on the local conditions.

Using the developed mechanism, three different burner designs were evaluated for their effectiveness in reducing NO_x emissions. It was found that a burner with a bluff body in the flame region is able to reduce NO_x better than the other designs.

CHAPTER 4. SOOT EMISSIONS FROM DIESEL SPRAY COMBUSTION

4.1 Objectives

In this study, a multistep soot model was derived and coupled with a detailed PAH mechanism to simulate soot formation and oxidation processes in diesel sprays. The soot model parameters were determined by comparing with the experimental data. Because the PAH mechanism was originally developed for diffusion flame application, it was found appropriate to be used for diesel spray combustion, and the soot prediction was improved for high EGR cases. The model was validated using experimental data from a constant volume combustion chamber and a heavy-duty diesel engine under different operating conditions.

4.2 Modeling Formulation

In this study, KIVA-3V was used as the baseline code with improvements in various physical and chemical submodels. Diesel spray was modeled as the Lagrangian phase moving in the Eulerian gas phase. Various submodels in the original KIVA-3V were replaced, including those for drop breakup, drop-wall interactions, wall heat transfer, and piston-ring crevice flows [20, 46, 101, 102]. Turbulence was modeled using RNG k - ϵ model with standard values for turbulence parameters [103]. KIVA-3V was integrated with chemical kinetics solver to allow the use of detailed chemistry. In the present model the chemistry and flow turbulence are coupled using diffusion transport and no subgrid scale turbulence-chemistry interaction model is used in this study.

The liquid properties of diesel fuel are based on those of tetradecane ($C_{14}H_{30}$) because of the similarity in the physical properties (e.g., vapor pressure, surface tension, etc.). The oxidation chemistry of diesel fuel is modeled using the chemical kinetics of n-heptane because both fuels have similar cetane numbers and combustion characteristics. The baseline n-heptane mechanism

has 35 species [104], which has been previously used in other studies and found to be effective in simulating diesel fuel combustion [47, 105]. The PAH mechanism, which describes the evolutions of the soot precursor species, is extracted from a detailed combustion mechanism [106]. The PAH chemistry involves the growth of a benzene molecule to pyrene, which acts as a soot nucleation site in the present model. The PAH mechanism essentially contains the sequential addition of aromatic rings through reactions with H, O, OH and C_2H_2 . The PAH oxidation by O_2 and OH is also considered in the reaction mechanism. The PAH mechanism and n-heptane mechanism are linked through the formation of benzene from acetylene. Overall, during combustion fuel species breaks down to form smaller molecules, such as C_2H_2 , and these molecules combine to form the PAH species, which in turn leads to inception of soot. The mechanism was also enhanced with additional species and reactions to model thermal NO_x emissions [47]. The new mechanism has 68 species and 144 reactions.

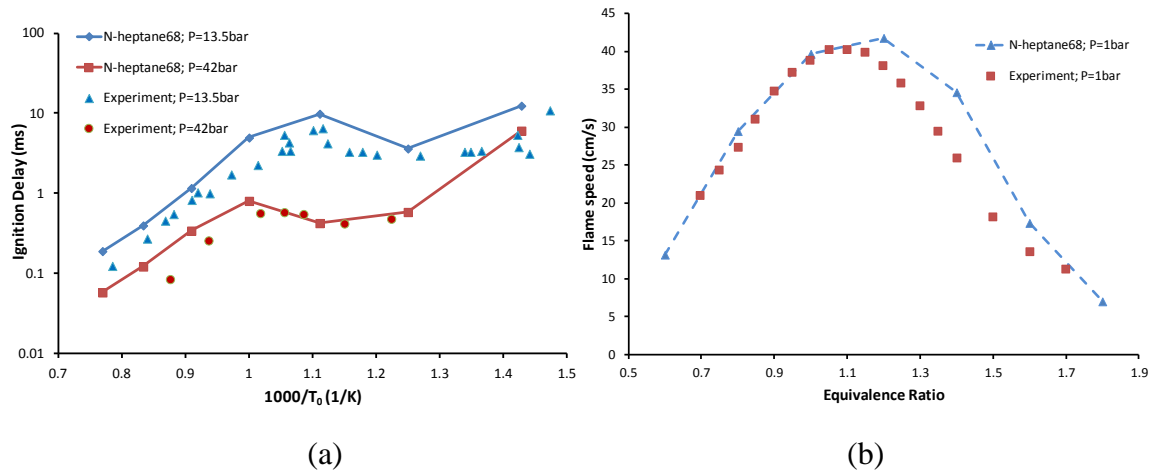


Figure 4.1 Comparison of predicted and experimental data on (a) ignition delay and (b) flame speed

The combined mechanism was further modified by modifying appropriate reactions such that the predicted ignition delays and flame speeds agree with the experimental results [107,

108], as shown in Figure 4.1. Ignition delays were slightly over-predicted at lower pressure. For the predicted flame speeds using the baseline 35-species n-heptane mechanism were over-predicted significantly, and this was fixed in the new mechanism by adjusting the rate constants for the most sensitive reaction $O+OH \rightleftharpoons O_2+H$. The validations were performed on the basis of zero-dimensional reactor simulation using DARS [109]. When the resulting mechanism was used for multi-dimensional spray combustion simulation, the model predicted longer ignition delays than experimental results. This was corrected by adjusting the reaction rate of $C_7H_{15}O_2+O_2 \rightleftharpoons C_7KET_{12}+OH$, which was found to be the most sensitive reaction for ignition delay. The modifications made in the mechanism are listed in Appendix A. The chemical kinetics solver was parallelized using mpi subroutines for faster chemistry calculations.

4.3 Soot Model

The standard two-step soot model has been used to predict soot emissions in diesel engines. However, at high EGR rates, as used in the new engines, the model is unable to predict the soot emissions correctly. Figure 4.2 shows the predicted soot level using a two-step soot model in a constant-volume combustion chamber at two EGR levels compared with the experiment results. As shown in the figure, the two-step model predicts nearly identical soot regions in both cases; however, experimental data indicate that the soot region is farther downstream and is much smaller than the predicted results. This two-step soot model treats soot as an additional species with source terms for soot formation and soot oxidation, as described in Section 2.4. The model was originally developed and validated for traditional diesel engine simulations. However, this model was not able to capture the soot evolution in diesel engines operated at high EGR conditions in which combustion takes place low-temperature environments [61]. It is known that the low-temperature chemistry is much more complex than the traditional

high-temperature chemistry because of the increase in reaction pathways in low-temperature combustion.

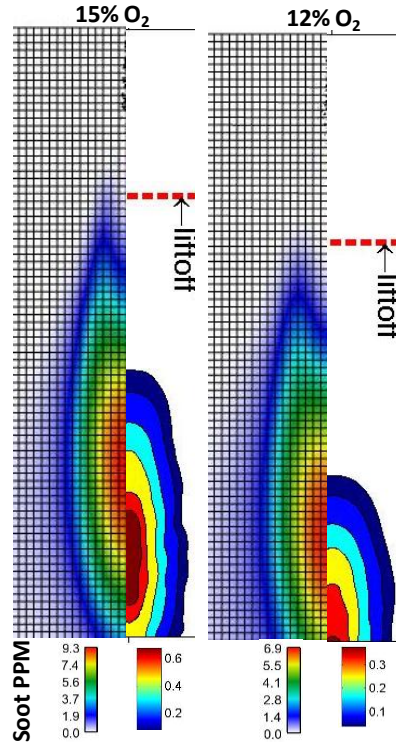


Figure 4.2 Comparison of the soot levels predicted by the two-step soot model (left) and experimental results (right) at an ambient density of 14.7 kg/m^3

A more comprehensive soot model is thus necessary to accurately predict the soot forming regions in the flame. The present multi-step soot model solves two additional transport equations for soot and soot number density, as shown in Equations (4.1) and (4.2). Moreover, the current model includes three soot formation and two oxidation steps along with a soot coagulation step. Details of each step and model parameters will be described in the following subsections.

$$\frac{d\rho y_s}{dt} = -\nabla \cdot (\rho y_s \cdot v) + \nabla \left[\frac{\mu}{SC} \nabla \left(\frac{\rho y_s}{\rho} \right) + \xi \cdot \rho y_s \cdot \frac{\mu}{\rho} \left(\frac{\nabla T}{T} \right) \right] + 16\dot{\omega}_{m1} + 3\dot{\omega}_{m2} + 6\dot{\omega}_{m4} - 2\dot{\omega}_{m5} - 2\dot{\omega}_{m6} \quad (4.1)$$

$$\frac{dN}{dt} = -\nabla \cdot (N \cdot v) + \nabla \left[\frac{\mu}{SC} \nabla \left(\frac{N}{\rho} \right) + \xi \cdot N \cdot \frac{\mu}{\rho} \left(\frac{\nabla T}{T} \right) \right] + 16 \cdot C_n \cdot \dot{\omega}_1 - \dot{\omega}_3 \quad (4.2)$$

ρy_s is the species density of soot and N , soot number density, is the number of soot particles per volume. The diffusion term of the governing equations are modified by including the thermophoretic diffusion of the transported quantities with $\xi=0.556$ [55, 110]. C_n is the number of soot particles corresponding to one carbon atom. The $\dot{\omega}_{mi}$ and $\dot{\omega}_i$ terms excluding $\dot{\omega}_3$, are the reaction rates in grams/(cm³.sec) and moles/(cm³.sec), respectively, from the different stages in soot evolution process. $\dot{\omega}_3$ is the coagulation rate of soot particles in particles/(cm³.sec). CGS system of units is used in this study unless specified otherwise.

The present soot model considers different reaction stages, including soot inception from the PAH species, soot surface growth, soot coagulation, PAH condensation, soot oxidation by oxygen, and soot oxidation by OH. The reaction rates for soot inception, surface growth, PAH condensation and soot oxidation serve as the source terms for soot species. The soot number density is affected by the rates of soot inception and soot coagulation. The framework of this soot stages are based on the recent soot model approach by Vishwanathan and Reitz [61]. Details of these reaction stages are described in the following.

Soot inception

Pyrene (C₁₆H₁₀) is used as the soot inception species similar to the previous work [61].



Rate constant k_1 is 2000 s^{-1} . $\dot{\omega}$ is the reaction rate and the term in square parenthesis indicates the molar concentration of the species. Pyrene is a four ring aromatic hydrocarbon and has been used as a soot inception species in recent studies [111]. Soot is assumed to be made of only by carbon atoms. The inception diameter is assumed to be 128 nm which corresponds to approximately 100 carbon atoms.

Soot surface growth

Soot surface is assumed to be enlarged by the addition of C_2H_2 through the following reaction proposed by Leung et al [55].



$$k_2 = 8.64 \times 10^4 \exp\left(-\frac{12100}{T}\right) \times \sqrt{S} \quad \text{s}^{-1} \quad (4.5)$$

S is the surface area of soot per volume, which is assumed to be spherical. T is the local temperature of the gas phase. The soot surface area is obtained from particle size as

$$S = \pi \cdot d_p^2 \cdot N \text{ cm}^{-1} \quad (4.6)$$

Particle diameter, d_p is calculated using a mass balance of soot species density and particle number density.

$$d_p = \left[\frac{6 \cdot \rho_y \cdot y_s}{\pi \cdot \rho_{C(s)} \cdot N} \right]^{1/3} \text{ cm} \quad (4.7)$$

Here, $\rho_{C(s)}$ is the density of soot species. The pre-exponential factor of the rate constant k_2 is calibrated based on the engine experimental results. Based on a sensitivity study of the stages in soot evolution, it was observed that soot surface growth rate has more influence on the soot production. The surface growth rate is adjusted to match with one of the diesel engine experimental study and the same value is used for all other simulations discussed in this study.

Soot coagulation

During soot coagulation, a number of soot particles aggregate together [55]. The process is represented by the following step.



Where, $M_{C(s)}$ is Molecular weight of carbon atom, N is the number of soot particles per volume and ρ is the density of gas phase.

$$k(T) = 2 \times C_a \times \left(\frac{6M_{C(s)}}{\pi\rho_{C(s)}} \right)^{\frac{1}{6}} \times \left(\frac{6K_{bc}T}{\rho_{C(s)}} \right)^{\frac{1}{2}} \quad \text{particles}^{-5/6} \cdot \text{mols}^{-1/6} \cdot \text{cm}^{-5/2} \cdot \text{s}^{-1} \quad (4.9)$$

Where, C_a is the agglomeration rate constant, which is assigned a value of 9, K_{bc} is the Boltzmann constant.

PAH condensation

Soot growth by the condensation of PAH compounds on soot particles is represented by



where, γ_{ks} is the PAH-soot collision efficiency, equal to 0.3, and β_{ks} is the PAH-soot collision frequency [112]. Benzene is used as the PAH species involved in this reaction.

Soot oxidation by O₂

To model the soot oxidation by O₂, the standard NSC soot oxidation formula with modified Arrhenius rates is used [113].

$$C_{(s)} + 0.5O_2 \rightarrow CO; \dot{\omega}_5 = \frac{12}{M_{c(s)}} \left[\left(\frac{K_A \cdot P_{O_2}}{1 + K_Z \cdot P_{O_2}} \right) x + K_B \cdot P_{O_2} \cdot (1 - x) \right] \cdot S \quad (4.11)$$

$$x = \frac{P_{O_2}}{P_{O_2} + \frac{K_T}{K_B}} \quad (4.12)$$

$$K_A = 30.0 \exp\left(\frac{-15800}{T}\right) \quad \text{g.cm}^{-2} \cdot \text{s}^{-1} \cdot \text{atm}^{-1} \quad (4.13)$$

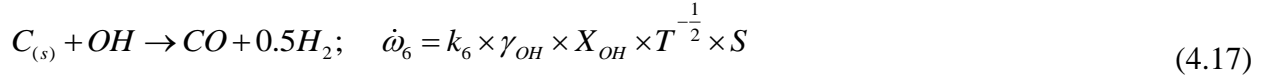
$$K_B = 8 \times 10^{-3} \exp\left(\frac{-7640}{T}\right) \quad \text{g.cm}^{-2} \cdot \text{s}^{-1} \cdot \text{atm}^{-1} \quad (4.14)$$

$$K_T = 1.51 \times 10^5 \exp\left(\frac{-49800}{T}\right) \quad \text{g.cm}^{-2} \cdot \text{s}^{-1} \cdot \text{atm}^{-1} \quad (4.15)$$

$$K_Z = 27.0 \exp\left(\frac{3000}{T}\right) \quad \text{atm}^{-1} \quad (4.16)$$

Soot oxidation by OH

A modified form of soot oxidation by hydroxyl [114] is used to model soot oxidation by OH.



γ_{OH} is the soot-OH collision efficiency, 0.13 and X_{OH} is the OH mole fraction. The value of the rate constant k_6 is adjusted to match the experimental results and a value of $106 \text{ mol.K}^{0.5}.\text{cm}^{-2}.\text{s}^{-1}$ is used in the presented study.

The soot model developed in this study provides more detailed descriptions of the soot formation and oxidation processes than the simple two-step soot model. The improvement of predicted results will be shown in the following section. The present soot model differs from other recently-developed soot models, which also use multiple reaction steps [60, 61], in the PAH mechanisms used. The PAH chemistry proposed by Wang and Frenklach [51, 52], which was used in the previous models, are mainly validated for premixed flames. The present model uses a PAH chemistry that is more suitable for non-premixed flames [115, 116], which is encountered in diesel engines. The PAH chemistry used in the present study incorporates additional reactions of H_2O and PAH reactions that are important at high EGR conditions. Note that EGR contains significant amount of water, which can alter reactivity of the system. The PAH mechanism used in this study is also a detailed mechanism with 60 reactions compared to the previous mechanism. This detailed reaction mechanism is provided in Appendix B.

4.3 Results

Grid Dependence Study

The grid dependence study of the multi-step soot model is performed by modeling n-heptane spray and combustion in a constant volume combustion chamber at 15% ambient oxygen mole fraction and 14.7 kg/m^3 ambient density conditions. A 2D mesh is used and the

mesh sizes are varied from 3 mm to 0.5 mm. The results using different meshes are presented in Figure 4.3.

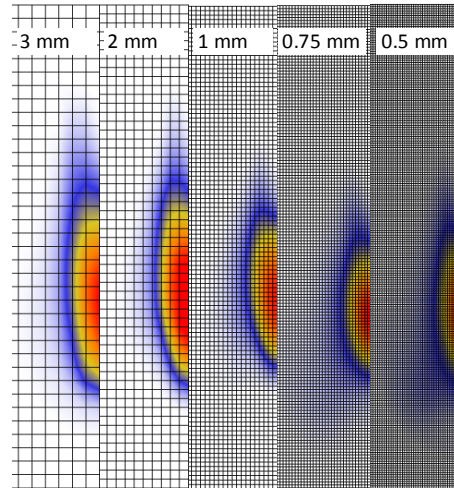


Figure 4.3 Soot (ppm) contours in constant volume combustion chamber at 15% O₂ and 14.7 kg/m³ ambient density using the multi-step soot model on different mesh sizes

In diesel spray flames the phenomenological scales that need to be considered in determining the grid size include those related to liquid droplets and flame thickness. The diameters of typical diesel droplets in the combustion chamber range from 0.15 mm to 0.05 mm during the injection and atomization processes. In the present computational approach, droplets are treated as discrete particles together with the assumption of dilute sprays. Therefore, the grid size needs to be considerably larger than the droplet diameter. On the other hand, the combustion regime in a diesel spray flame is a combination of premixed and diffusion combustion. The reaction zone appears to be a brush of reaction region with a thickness of a few millimeters. The exact details of the diesel spray flame remain a challenging research topic. Nonetheless, typical diesel engine combustion simulations use a grid size of 1 to 2 mm across the computational domain, considering the resolution of physical phenomena and the computational requirements.

Note that the grid size is not uniform in a diesel combustion chamber because of the complex geometry, but the present grid dependence study uses a uniform mesh for the single diesel spray for comparison. The grid size used here, 3 mm to 0.5 mm spacing, is considered reasonable for assessing the grid effects.

Results of this grid dependence study show that the coarser mesh predicted a wider region of soot whereas the finer mesh, with 1 mm or smaller, predicted approximately the same soot formation regions. The soot model was able to provide qualitatively grid independent results using grid size below 1 mm for diesel spray conditions. It is also noticed that the peak values of soot using different mesh sizes varied considerably, from 10 ppm for coarser mesh to 2 ppm at the 0.5 mm mesh. It is worth noting that it is extremely challenging to predict soot emissions accurately, even by use of detailed chemistry that considers hundreds of species and reactions. Because of the complexity of the soot process and the limitation of the present model, soot model constants will be calibrated for the baseline engine case when the model is applied for engine simulation. Once the model constants are determined, they remain unchanged for all other operating conditions.

Constant Volume Combustion Chamber Results

The present multi-step soot model was used to simulate Sandia combustion chamber experiments [117]. The experiments were conducted in an optically accessible combustion chamber. High-pressure and high-temperature conditions are generated inside the chamber by burning a specified premixed mixture before the start of fuel injection. Different ambient EGR conditions were created by using appropriate mixture compositions. The experiments were conducted for studying the effect of EGR on soot emissions. A 2-D axisymmetric domain with a height of 10.8 cm and width of 12.4 cm was used in simulation. The domain was discretized

using 1×1 mm mesh. Predicted flame lift-off lengths and soot contours were compared with the experimental results. In the experiments, OH chemiluminescence was used to determine the lift-off length. However, in the simulations, active OH radical (OH^*) was not modeled. The lift-off lengths in simulations were determined at locations where the combustion reaches an apparent high temperature, i.e., 1400 K. In the experiments, laser extinction and planar laser-induced incandescence (PLII) were used to make quantitative measurements of soot in a diesel fuel jet. For model validation, the soot volume fractions (in ppm) from experiments were compared with those from simulations. In the simulations, the code was parallelized for running on four processors, and each simulation required approximately two hours.

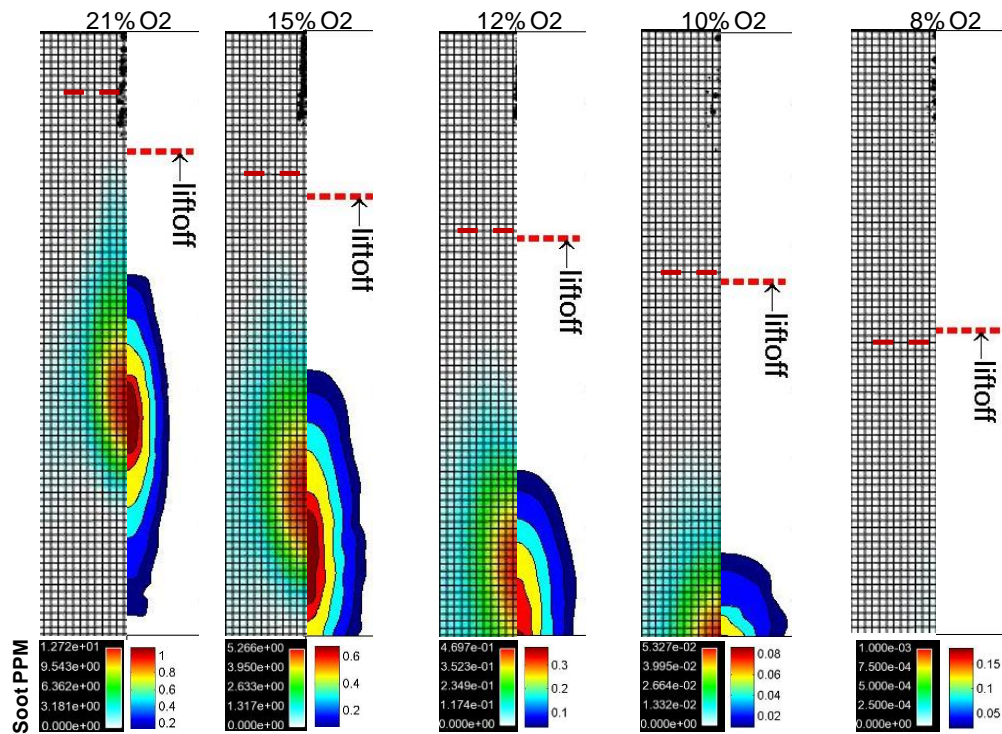


Figure 4.4 Soot (ppm) by simulation (left) and experiment (right) at different EGR levels for ambient density of 14.7 kg/m^3 .

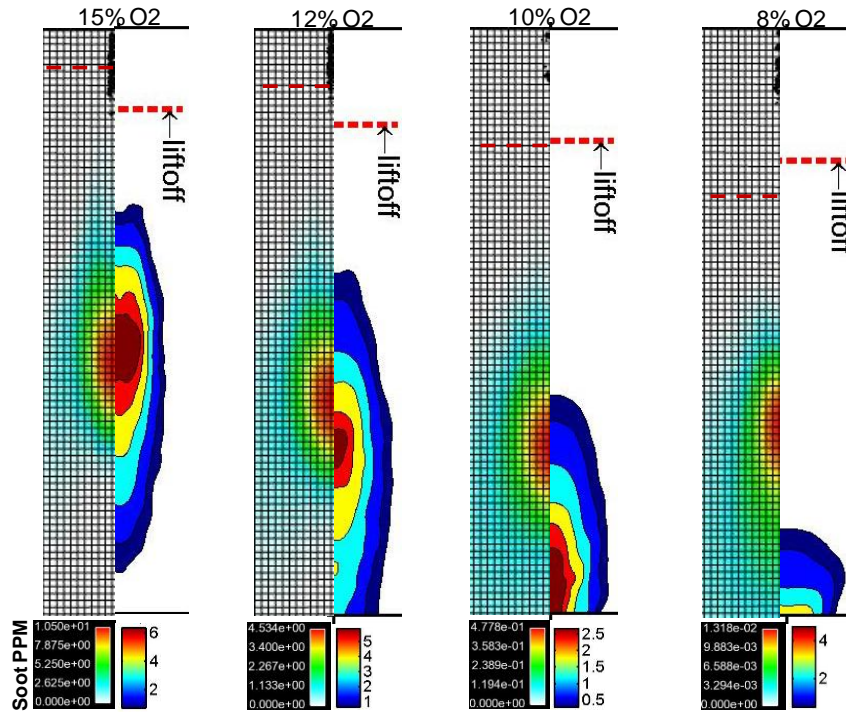


Figure 4.5 Soot (ppm) by simulation (left) and experiment (right) at different EGR levels for ambient density of 30 kg/m^3 .

Figure 4.4 and Figure 4.5 show the comparison of experimental and simulation results at different ambient densities. The multi-step soot model predicted improved results compared to the two step soot model. It can be seen that the peak soot concentration decreases and also the location of soot shifts downstream with decreased oxygen content in ambient air, i.e., higher EGR levels. Good qualitative agreement was obtained between experimental and predicted results. The quantitative agreement in ppm varies under different conditions. With high EGR levels, the peak soot locations are predicted more upstream than the experimental data. In the case of high ambient density and high EGR conditions, the predicted location of soot does not agree well with the experiments, and possible reasons are as follows. A likely downward shift was reported in experimental soot contours derived from the PLII intensity images [116]. The

standard KIVA-3V evaporation model tends to under-predict the vapor penetration at high ambient density conditions, resulting in a shorter flame [118]. Improved spray and evaporation models will help improve the prediction of the fuel vapor distribution, which in turn will affect the combustion prediction.

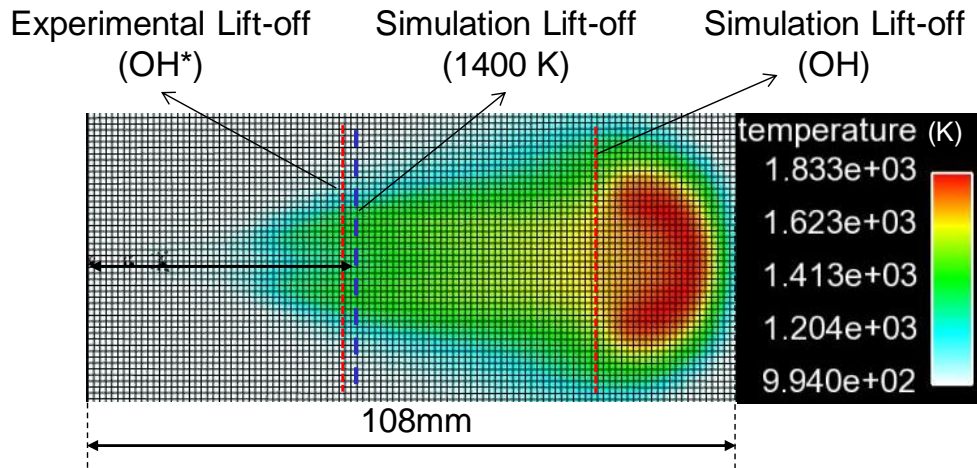


Figure 4.6 Comparisons of the lift-off locations identified by experiments and simulation for 8% O₂ EGR level. Predicted flame temperature is also shown.

The present mechanism was able to predict the lift-off length reasonably well at all EGR conditions. In the simulations, the predicted lift-off locations were determined based on the temperature data, unlike experiments that used OH* because OH* radicals were not modeled in the simulations. Although OH is also one of the chemical species in the reaction mechanism, OH is different from OH* and thus is not used for identifying the lift-off location. The OH contours was found to perform well in predicting lift-off at 21% O₂ ambient conditions, however at high EGR cases the OH lift-off predicted from OH contours deviated considerably from the experimental results. This could be a limitation of the baseline N-heptane mechanism which was generated by applying mechanism reduction to a more comprehensive mechanism. It was found that it is more appropriate to use temperature to identify the lift-off location than OH in the

simulation. A comparison of experimental lift-off and simulation lift-offs using temperature and OH species for 8% O₂ at 4.2 MPa ambient pressures is shown in Figure 4.6. An empirical temperature of 1400 K was used to determine the lift-off location. Despite the uncertainties in identifying the lift-off locations and certain levels of disagreement in soot concentrations for some cases, overall the present model has performed reasonably well, particularly the trend, considering the complex nature of fluid mechanics and soot chemistry in diesel sprays.

Figure 4.7 (a) shows the comparison of ignition delays from experiments and simulations. The ignition delay is derived from the point of the initial pressure rise. At high EGR levels, the predicted ignition delays were shorter than the experimental delays with a maximum of 0.2 ms difference at 8% O₂ EGR level. This is because of the slight difference in the pressure rise at the start of ignition. Figure 4.7 (b) compares the pressure rises between predicted and experimental data. Although the present model was able to predict the overall pressure rise, slight differences at the starting of ignition are seen. The model was able to predict the increase of ignition delay at high EGR levels.

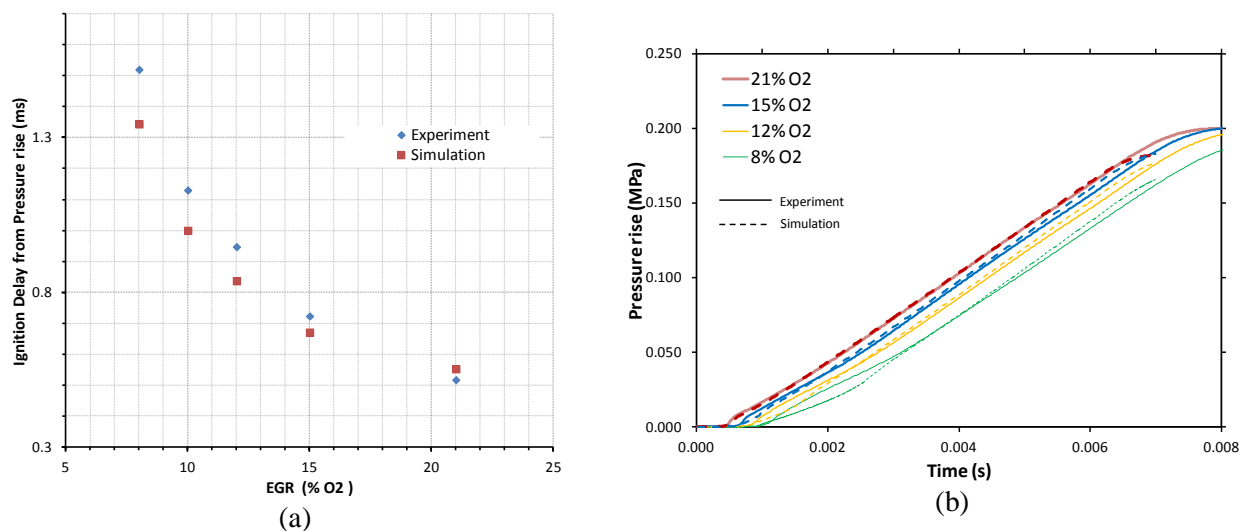


Figure 4.7 (a) Predicted and measured ignition delays at different EGR levels, (b) Comparison of the pressure histories by experiment (solid) and simulation (dashed)

The performance of the present multi-step soot model is compared to those of other soot models. Comparisons between Fig. 4.2 and Fig. 4.3 (15% and 12% O₂ conditions) indicate that the present multi-step soot model is able to predict the sooting regions more accurately compared to the two-step soot model. On the other hand, when compared to the other multi-step soot models [61, 119, 120], the present model is able to improve the predictions on sooting regions of the flame, especially for the lower ambient density conditions. The thickness of the sooting region predicted by other previous models is thinner compared to the present results and experimental results, as shown in Figure 4.8. Previous models also predicted that soot started to form at upstream locations at high ambient pressure and high EGR (low O₂ levels) conditions, same as the present soot model (e.g., Figure 4.5). Although the present soot model predicts different magnitudes of soot emissions (in ppm) from the experimental data, the model is able to predict the soot locations reasonably well, which is critical in engine application as the engine-out soot is strongly dependent on the soot forming locations.

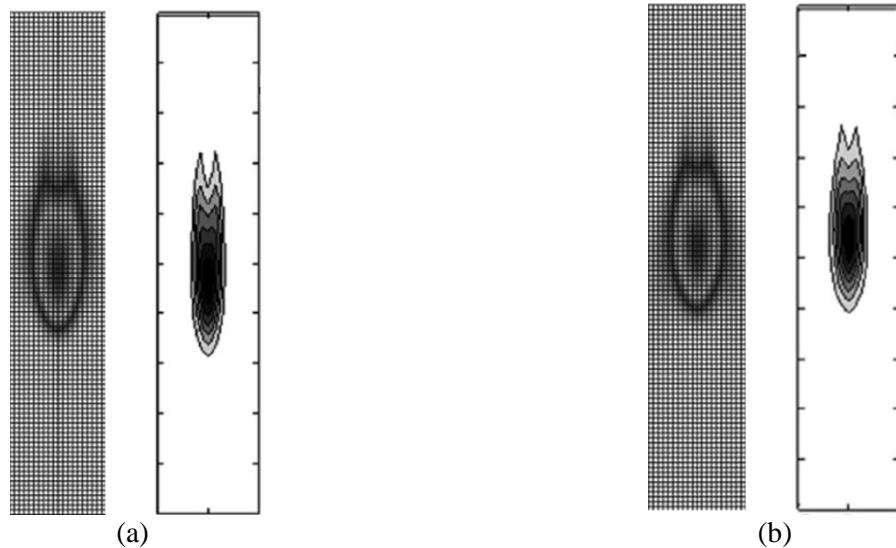


Figure 4.8 Comparison of predicted soot contours using the present model (left) and the previous soot model in literature [61] (right) at ambient conditions (a) 14.7 kg/m³ and 21% O₂ (b) 30.0 kg/m³ and 15% O₂

Engine Results

Table 4.1 Engine specifications

Manufacturer	Caterpillar
Type	Single-cylinder
Bore X Stroke	137.2 mm X 165.1 mm
Compression ratio	16.1:1
Displacement	2.44 L
Connecting rod length	261.6 mm
Squish height	1.57 mm
Combustion chamber geometry	In-piston Mexican hat with sharp-edged crater
Piston	Articulated
Charge mixture motion	Quiescent
Maximum injection pressure	190 MPa
Injected fuel	3.31 – 3.62 g
Injection duration	5.0 – 7.0 deg crank angle
Number of nozzle holes	6
Nozzle hole diameter	0.214 mm
Included spray angle	145.0 deg
Injection rate shape	Rising
Experimental conditions	
Percentage EGR	SOI (ATDC)
8% EGR	-20, -15, -10, -5, 0, +5
27% EGR	-20, -15, -10, -5, 0, +5
40% EGR	-20, -15, -10, -5, 0, +5

The multi-step soot model was further applied to simulate the experiments using a heavy-duty diesel engine [47]. Table 4.1 lists the specifications of the engine and the operating conditions used for model validation. The simulations were conducted for three different EGR

levels, each with six different start of injection (SOI). A 60-degree sector mesh with periodic boundaries was used as the computation domain. The domain was meshed using a cylindrical grid with fine mesh near the axis and coarse mesh at the cylinder walls. The average grid size was approximately 2 mm. The mesh is finer near the spray region with an average cell size of 0.5mm. The predicted in-cylinder pressure and heat release rate data were compared with experimental results as shown in Figure 4.9. The results shown in Figure 4.9 are those of 8% EGR cases, and similar levels of agreement were obtained for other EGR conditions. The ignition delay prediction was within ± 4 crank angle degrees (CAD). The maximum deviation in peak pressure was approximately 1 MPa, obtained for 8% EGR case at SOI of +10 degrees after top dead center (ATDC).

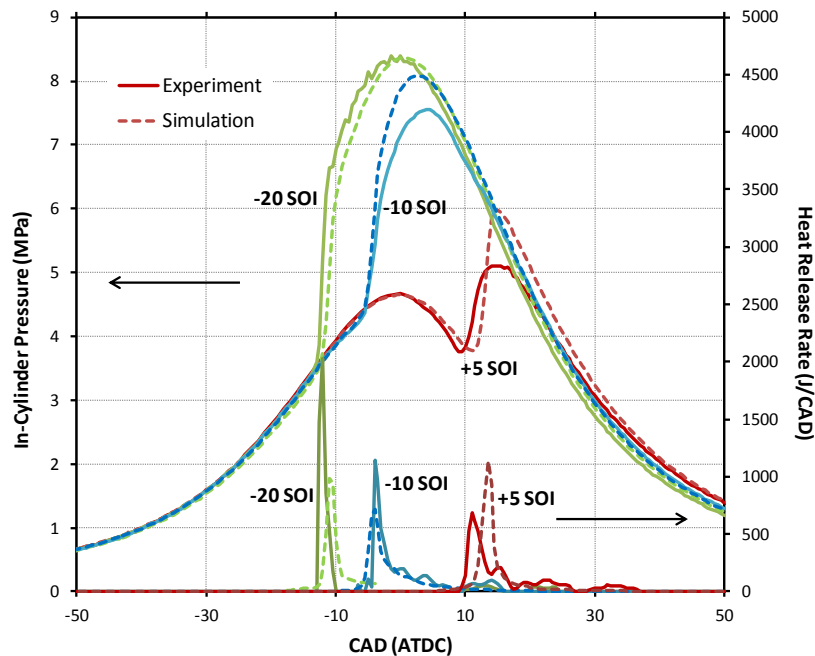


Figure 4.9 Comparison of predicted in-cylinder pressure (MPa) and heat release rate (J/CAD) with experimental data for 8% EGR level

The predicted engine-out soot emissions were compared with the experiment data in Figure 4.10. The present soot model was able to predict the trend of soot emissions at different EGR conditions reasonably well. The soot emissions increase with increased EGR. It can be seen that the soot emissions are the highest when SOI is close to TDC. At late injection conditions, the model predicted almost zero soot at all conditions. This deficiency is believed to be caused by the fact that very low C_2H_2 at late injection conditions was predicted, and as a result, the predicted exhaust soot level was low. Compared with one of the previous multi-step soot model which used the same experiment for comparison [60], the present soot model is able to improve the sensitivity of soot on EGR conditions.

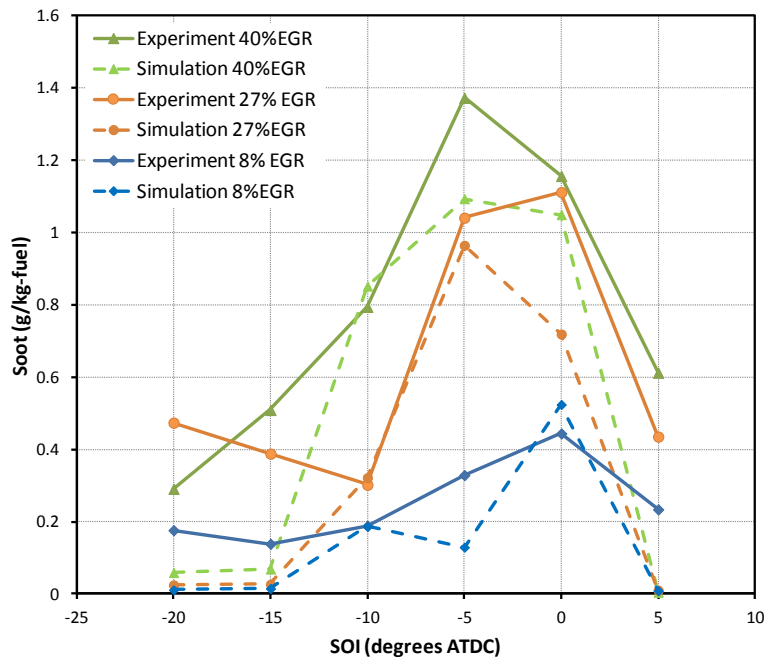


Figure 4.10 Comparison of predicted and measured engine-out soot data (g/kg-fuel)

Experimental results obtained from the constant-volume combustion chamber at Sandia show that soot decreases with increased EGR; however, results obtained from engine tests

indicate that the engine-out soot increases at high EGR. This phenomenon can be explained using the predicted in-cylinder soot evolution as shown in Figure 4.11. It can be seen that the 8% EGR case produces maximum soot and the 40% EGR case produces minimum soot. At low EGR conditions, the combustion temperature is high, resulting in the oxidation of most of the soot generated. Thus, the engine-out soot emissions are lower for low EGR conditions.

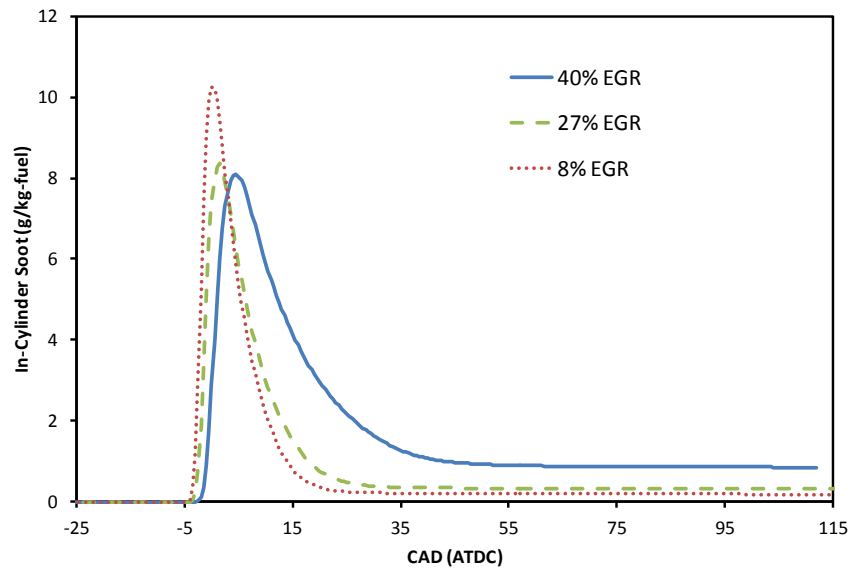


Figure 4.11 In-cylinder soot evolutions for different EGR levels for SOI= -10 ATDC

For the same EGR, the trend in soot emissions with respect to different injection timings can be explained based on the difference in the combustion characteristics. Figure 4.12 and Figure 4.13 show the temperature and soot contours of the 8% EGR conditions at SOI at -10 and 0 ATDC, respectively. It can be seen that initially soot forms primarily near the piston bowl surface, which is at moderately high temperature. This region is also rich in fuel. As the cycle progresses, combustion (i.e., high temperatures) spread to this rich region and soot is oxidized. Similar trends of soot evolution are observed in all EGR conditions. When the injection timing is

retarded from -10 to 0 ATDC, combustion mainly occurs during the expansion stroke, and as a result combustion temperature decreases rapidly. For SOI at -10 ATDC, the peak temperature drops from 2750 K to 2650 K during the period shown in the figure, whereas for SOI at 0 ATDC, the peak temperature drops from 2700 K to 2450 K. A higher temperature enhances the oxidation of soot. Thus, the comparatively lower temperatures when start of injection is close to TDC results in lower soot oxidation and higher engine out soot emissions. When the SOI was delayed further into the expansion stroke, the soot formation itself was reduced. This could be because of the lower ambient pressure due to delayed injection as seen in Figure 4.9. The constant volume combustion chamber results shown in Figure 4.4 and Figure 4.5 also suggest that the soot formation decreases at lower ambient pressures. Thus lower engine out soot emissions was observed when SOI was further delayed beyond TDC.

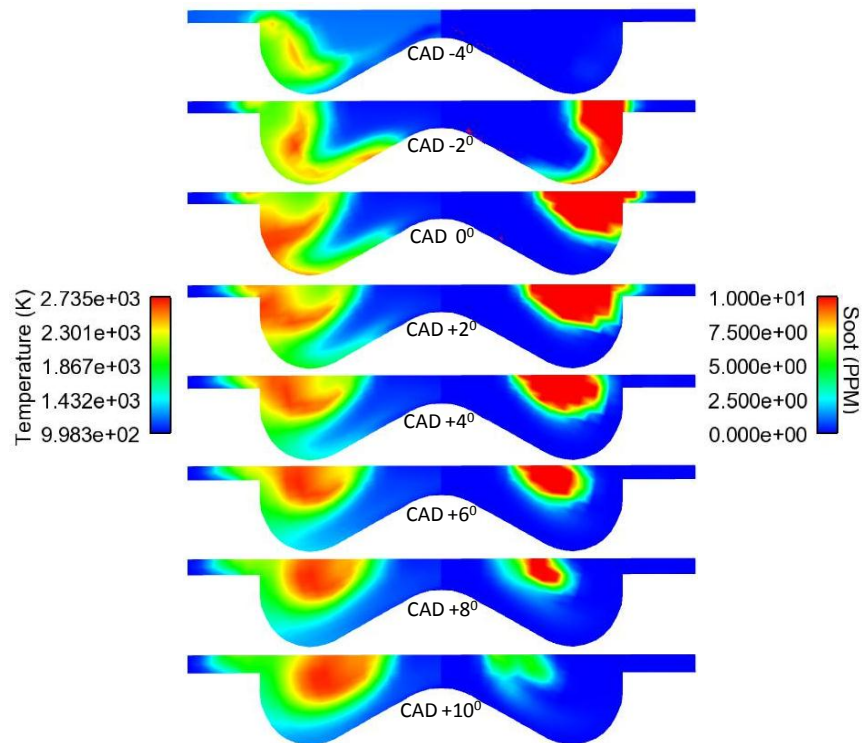


Figure 4.12 Contours of temperature (left) and soot (right) at different times for 8% EGR, SOI= -10 ATDC

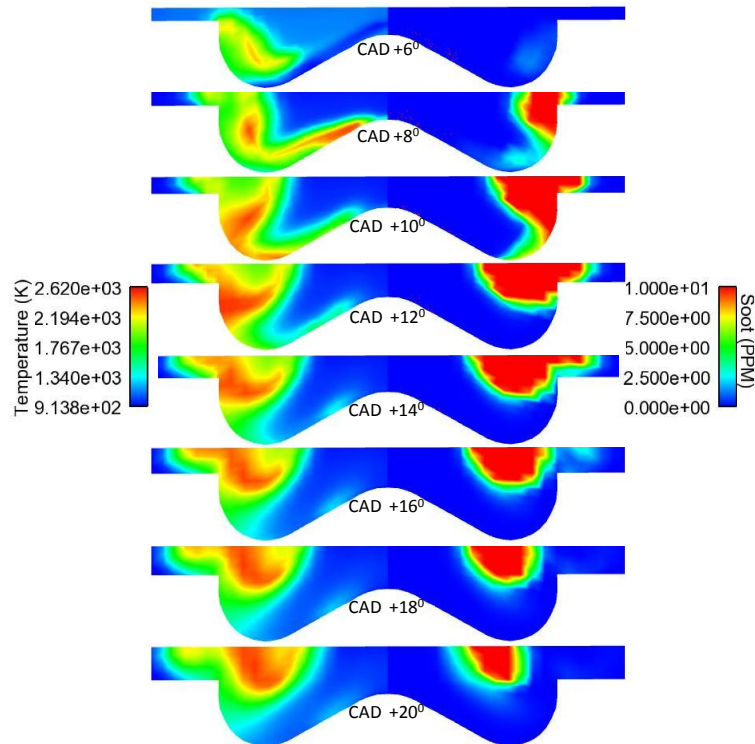


Figure 4.13 Contours of temperature (left) and soot (right) at different times for 8% EGR, SOI= 0 ATDC

The NO_x emission prediction from the current model is shown in Figure 4.14. Since only thermal NO_x is present in n-heptane combustion, the NO_x emissions are mainly a function of temperature. As a result, the NO_x emissions reduced considerably at low temperature combustion regimes such as the 40% EGR cases. Figure 4.15 represents the soot- NO_x trade off from the engine cases modeled. The increasing NO_x axis corresponds to the advanced SOI timings. In general a low NO_x regime is negated by high soot emissions. However, in some cases such as 40% EGR and -20 ATDC SOI, it was observed that low soot emissions can be achieved along with low NO_x emissions. The zero soot emissions observed at late injection cases are not accounted as a viable low emission strategy, as accurate predictions at these conditions remains out of reach for the current soot model.

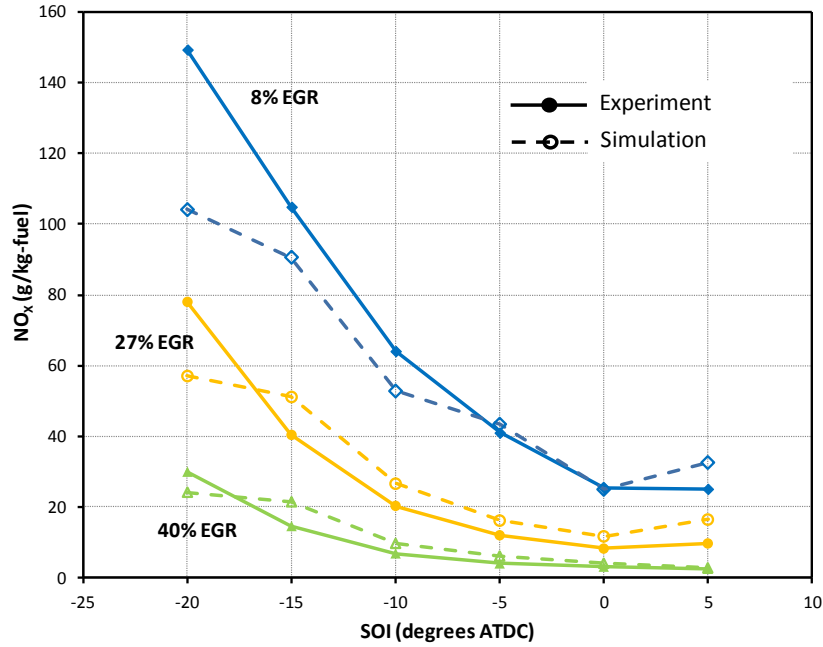


Figure 4.14 Comparison of predicted and measured engine out NO_x data (g/kg-fuel)

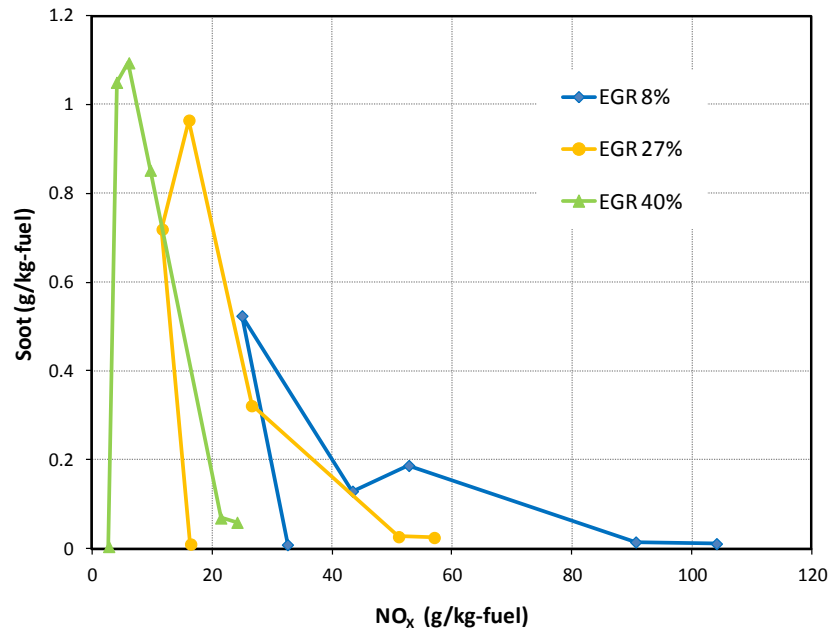


Figure 4.15 Predicted Soot-NO_x trade-off for the SOI sweeps at different EGR levels

4.4 Summary

A multi-step soot model, coupled with detailed n-heptane and PAH chemistry, was used to simulate soot emissions from diesel spray combustion. The model considers different stages of soot formation and oxidation, including inception, surface growth, coagulation, PAH condensation, and oxidation. The PAH chemistry considers the growth of benzene rings to pyrene and the oxidation of these PAH molecules. The PAH mechanism and n-heptane mechanism are coupled through the formation of benzene from acetylene. The new n-heptane mechanism with PAH chemistry was validated by experimental data for ignition delays and flame speeds.

For diesel spray combustion in a constant-volume chamber, the present model was able to predict the trend of soot emissions with respect to EGR levels. The model was able to predict the locations of the peak soot regions for most of the cases. For the case of high ambient pressure with extremely high EGR, the predicted high soot region was more upstream than the experimental results. The present model was also applied to simulate the combustion in a heavy-duty diesel engine and was able to predict the trend of soot emissions with regard to EGR levels and injection timings. The results from engine simulations were further analyzed to determine the effect of EGR on engine soot emissions. It was found that high EGR will result in lower combustion temperature which in turn will inhibit soot oxidation, resulting in high engine-out soot emissions.

CHAPTER 5. IMPROVEMENTS ON SPRAY AND EVAPORATION MODELS

5.1 Gas Parcel Model for Evaporating Sprays

Background and Objective

In this study, KIVA-3V is used to model the diesel spray processes [15, 21]. The basic spray breakup model in KIVA-3V is replaced by a breakup model that considers the growth of the unstable surface wave, which induces breaking up of liquid spray into droplets [20]. This spray model, along with the original KIVA-3V evaporation model, often under-predict vapor penetration, as shown in Figure 5.1. It can also be seen that the slope of the vapor penetration curve has a sudden decrease when the liquid particles are completely evaporated. The momentum sources from the liquid particles vanish as soon as the particles are evaporated. The absence of momentum sources causes the sudden variation of vapor penetration with and without the presence of liquid particles, as seen in Figure 5.1. Thus, additional models are required to supply the momentum sources to the gas phase beyond the region where the liquid spray is present.

In this study, a new model, based on the concept of “gas parcel,” is used in order to improve the predicted spray penetration results. In this new model, momentum sources are provided to the gas phase through gaseous parcels which do not retain any fuel vapor mass. The gaseous parcels are tracked even after the liquid droplets are completely evaporated. This is necessary to provide extra momentum for the gas phase in order to increase the vapor penetration. By providing continuous momentum sources after the liquid droplet region, the sudden decrease in the vapor penetration can be avoided. The current model differs from the previous models in releasing the vapor mass to the gas phase. Previous models retained the vapor mass to the vapor parcel and gradually released it to the gas phase based on certain criteria which

depend on cell size. This results in conditions such as very low or no vapor near the nozzle region even though the particle is evaporating, especially in the case of coarse grids. In the new model, the vapor mass is released to the gas phase directly from the liquid droplet and the same mass is added to the vapor parcel, which is an imaginary parcel used to track the momentum sources. The model is applied to non-reacting diesel sprays to validate the vapor penetration and grid dependency. The model is further applied in reacting spray cases in constant volume chamber and diesel engine simulations.

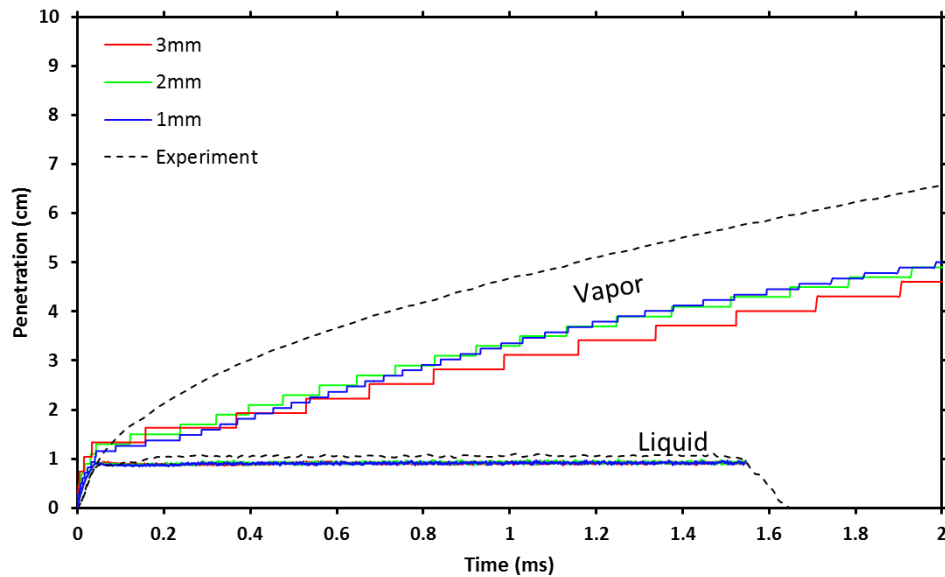


Figure 5.1 Liquid (L) and vapor (G) penetration of fuel spray using standard evaporation model KIVA-3V on different grid sizes compared with experimental liquid and vapor penetration results [117]

In this work, for improving the droplet vaporization modeling of complex fuels, a discrete component model is developed to simulate biodiesel drop vaporization. A hybrid approach is used which models the biodiesel-diesel spray by treating the droplet as multicomponent for evaporation purpose and as single component for spray dynamics. This

approach is as computationally efficient as the single-component model but possesses the advantages of multi-component models in predicting the vaporization rates of individual components. In addition, a multi-step soot model is integrated with the discrete component vaporization model to predict soot emissions from biodiesel combustion. The biodiesel reaction mechanism is coupled with additional PAH reactions.

Model Details

KIVA-3V employs a “parcel” technique to model evaporating sprays in which each parcel represents a number of droplets with identical properties such as radius, velocity and temperature [121]. The parcels are injected with an initial velocity and as they travel through the gas phase, mass, momentum and energy are exchanged with the gas phase. The momentum sources are calculated based on the difference in particle velocities between the time steps. The sources are coupled to the momentum equation to the node closer to the particle. If the spray is evaporating, the particle radius will diminish every time step based on the evaporation rate and the corresponding change in particle mass is added to the gas phase as fuel vapor [16]. The momentum sources from liquid particles initiate motion to the gas phase fluid. The momentum sources cease at the location where the spray is completely evaporated. The reason for this under-prediction is because of the large difference between the droplet particle mass and cell mass. The momentum exerted by the evaporated particle mass is insufficient to drive the gas phase mass. Previous studies have reported that with a very fine mesh this issue can be mitigated to some extent [122, 123]. However, such fine mesh requires large computational resources, which is not feasible for practical engine applications. An alternative approach to reduce this deficiency is to introduce gas parcels into the gas phase in order to track the momentum resulting from the evaporating particles [87].

Gas parcels are imaginary Lagrangian particles used to track the momentum of evaporated liquid particles. As the liquid particle evaporates, a gas parcel is assigned. The mass of the gas parcel is equal to the mass evaporated from the liquid particle with the velocity equal to that of the liquid particle. Thus, the gas parcel has the same momentum as that of the evaporated droplet mass. By tracking this gas parcel, the momentum of evaporated mass is transported. This gas parcels provide momentum sources even after the liquid spray is completely vaporized. However, in this model the gas parcel does not retain the vapor mass from the evaporation of its corresponding liquid parcel. The gas phase cell will receive the evaporated fuel vapor mass and at the same time the mass of gas particle is increased by the same amount as shown in Equation (5.1). The radius of a gas particle will grow with time by diffusion of fuel vapor as per Equation (5.2).

$$m_{gasp}^{n+1} = m_{gasp}^n + m_{evap}^n \quad (5.1)$$

$$r_{gasp}^{n+1} = r_{gasp}^n + \sqrt{(D_v dt)} \quad (5.2)$$

Where, m_{gasp} is the mass of gas particle, m_{evap} is the evaporated mass from liquid particle, r_{gasp} is the radius of gas particle, D_v is the molecular diffusivity of fuel vapor and dt is the time step size.

If the gas particle grows larger than cell size, the diameter of gas particle is limited to the cell size and a corresponding mass is shed from the gas particle. The mass distribution inside the gas particle is assumed to be a Gaussian distribution as used by Beard et al. [87]. The gas parcel is tracked along with the liquid parcel as long as the liquid parcel exists. When a liquid parcel undergoes breakup, the associated gas parcel will remain with the parent liquid parcel with larger radius. In the case of collision and coalescence of liquid parcel, the mass of gas particles are

added to the dominant parcel and the larger gas parcel radius is retained. When the liquid particle is completely evaporated, the gas parcel is tracked independently as per Equation (5.3).

$$\frac{d\vec{V}_p}{dt} = \frac{C_D \rho \|\Delta\vec{V}_p\| \pi r_{gasp}^2}{m_{gasp}} (\Delta\vec{V}_p) \quad (5.3)$$

C_D is the drag coefficient of particle, V_p is the particle velocity, ΔV_p is the relative velocity of particle and ρ is the density of gas phase. In order to calculate the drag coefficient of the gas parcel, it is assumed that these are spherical particles. The density of a gas parcel was found to be few orders of magnitude higher than that of the ambient medium during most of its lifetime. Under these conditions, it is safe to assume that these gas parcels behave similar to liquid droplets. This allows calculating the drag force on the gas parcel similar to that of the liquid particle [16] as shown in Equation (5.4). Similar drag force correlations for the gas parcels have been used in previous gas parcel models as well [89].

$$C_{D,pgas} = \frac{24.0}{Re_{pgas}} \left(1 + \frac{1}{6} Re_{pgas}^{2/3} \right) \text{ for } Re_{pgas} < 1000 \quad (5.4)$$

$$C_{D,pgas} = 0.424 \text{ for } Re_{pgas} \geq 1000$$

Re_{pgas} is the Reynolds number based on the gas parcel diameter.

Turbulent dispersion of these standalone gas parcels are also considered in the tracking. The gas particle adds momentum sources to the cell vertex closer to the gas particle. Breakup and collision models were not implemented for standalone gas parcels.

The standalone gas particles are terminated based on two conditions. If the density of gas particle is less than the fuel species density in the cell or if the velocity of gas parcel is less than cell velocity as shown in Equations (5.5) and (5.6), the particle will be deleted. A gas parcel is

terminated by setting its mass to zero and excluding the zero mass particles in the future calculations.

$$\frac{Nm_{gasp}}{\frac{4}{3}\pi r_{gasp}^3} \leq \rho_{fuel} \quad (5.5)$$

$$\|\vec{V}_p\| \leq K_v \|\vec{V}_{local}\| \quad (5.6)$$

Where, N is the number of droplets in a parcel, ρ_{fuel} is the fuel density in the cell and V_{local} is the local velocity of gas phase. The first condition removes gas parcels which are diluter than ambient fuel vapor. The second condition removes gas parcels with low relative velocities. It was found that the velocity condition is more sensitive to the vapor penetration and thus a tuning factor, K_v is provided for this condition. In this study a tuning factor of 1.0 was used. The gas parcel model was developed and validated with only non-reacting spray conditions in this study. A detailed investigation on the effect of chemical reactions on these momentum sources has not performed in this study.

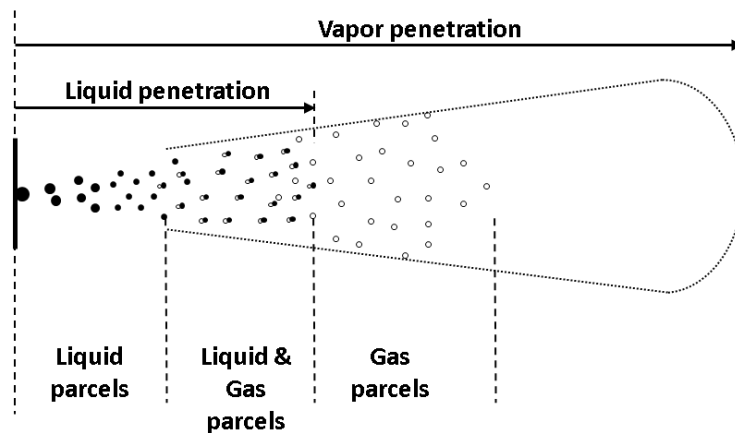


Figure 5.2 Schematic of gas parcel model

A schematic of gas parcel model is given in Figure 5.2. The solid spheres represent the liquid parcels and hollow spheres represent the gas parcels. The region where gas parcels are tracked along with liquid particles are shown as hollow sphere attached to solid sphere.

5.2 Discrete Component Vaporization Model

A discrete component vaporization model is developed to predict the vaporization of the biodiesel components by considering the physical properties of individual components. The vapor pressure of biodiesel components are evaluated using the Antoine equation [124]. The latent heat data are determined from Yaws handbook [125]. The density of biodiesel is calculated using the Rackett equation [68, 126]. Fuller correlation is used to determine the diffusivity of biodiesel components in air [127].

The evaporation rate of each component is determined as

$$\dot{m}_i = 4\pi R\rho\varepsilon_i D_{ig} \ln(1 + B_{M,i}) \quad (5.7)$$

where, R is the radius of the drop, ρ is the density of ambient medium, D_{ig} is the diffusivity of fuel vapor component in ambient medium, ε_i is the fraction of vaporization rate and $B_{M,i}$ is the Spalding mass transfer number, defined as

$$B_{M,i} = \frac{y_{i,s} - y_{i,\infty}}{\varepsilon_i - y_{i,s}} \quad (5.8)$$

Here, subscript s denotes the surface of the drop, ∞ denotes far away from the drop and i denotes the fuel component. ε_i is calculated by solving simultaneous equations of

$$D_{ig} \ln(1 + B_{M,i}) = D_{jg} \ln(1 + B_{M,j}) \quad (5.9)$$

$$\sum \varepsilon_i = 1. \quad (5.10)$$

The temperature of the drop is determined through the energy balance of droplet heating, latent heat of vaporization, and the temperature change of the ambient air.

$$\left(\sum m_i C_{liq,i}\right) \dot{T}_d = \sum \dot{m}_i L_i(T_d) + 4\pi r^2 Q_d \quad (5.11)$$

In the above, Q_d is the heat transfer rate to the droplet and is calculated as

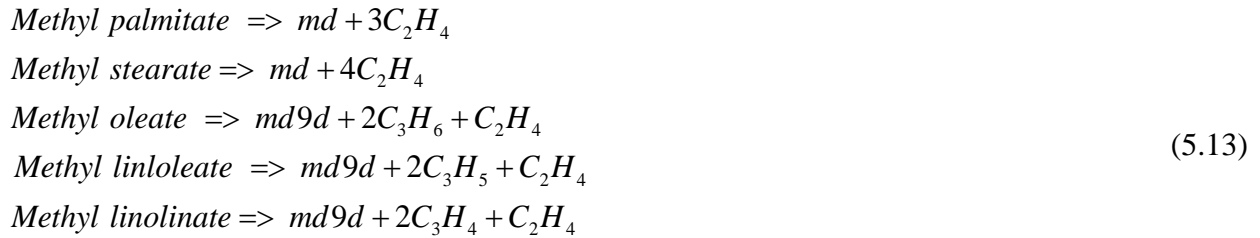
$$Q_d = \frac{K_{air}(T - T_d)}{2r} Nu_d. \quad (5.12)$$

Nusselt number is calculated for each component in a way similar to that of the standard KIVA-3V approach. A mass fraction weighted averaged Nusset number, Nu_d is used in Equation (5.12). K_{air} is the thermal conductivity of air. Equation (5.7) is coupled with Equation (5.11) and is solved implicitly for the droplet temperature.

5.3 Reaction Mechanism

The biodiesel reaction mechanism [69] is coupled with a PAH reaction mechanism in order to predict soot precursor formation and oxidation. In the mechanism, the PAH species are formed from acetylene molecules, which undergoes a series of reactions to form benzene. Benzene then forms polycyclic aromatic rings through hydrogen abstraction carbon addition reactions. The PAH mechanism is part of a detailed n-heptane combustion mechanism, which was used in previous studies and validated for non-premixed flame simulation [106]. Five additional reactions are added to the mechanism to convert the methyl ester components to the corresponding reacting species as shown in Equation (5.13). In the chemical reactions, the

saturated esters are converted to methyl decanoate (*md*) and unsaturated ones are converted to methyl-9-decenoate (*md9d*) species. The rates of these reactions are assumed to be same as the rate at which a heptyl radical (C_7H_{15}) breaks down to form smaller hydrocarbons in the parent mechanism. The overall mechanism consists of 95 species and 257 reactions. The parallel version of KIVA-CHEMKIN is utilized to speed up the computation of this reaction mechanism.



5.4 Multi-Step Soot Model

The soot model described in Chapter 3 is used to model soot from biodiesel. In the soot model, soot species growth and soot OH oxidation are the two most sensitive reactions which affect the soot evolution. Thus, the model constants for these reactions are calibrated with the experimental data for specific fuels. In the soot growth step, soot is assumed to be enlarged by the addition of C_2H_2 through the following reaction.



$$k_2 = 3.6 \times 10^3 \exp\left(-\frac{12100}{T}\right) \times \sqrt{S} \quad s^{-1} \tag{5.15}$$

Here, S is the surface area of soot per volume, which is assumed to be spherical. T is the local temperature of the gas phase. The soot surface area is obtained from the particle size as

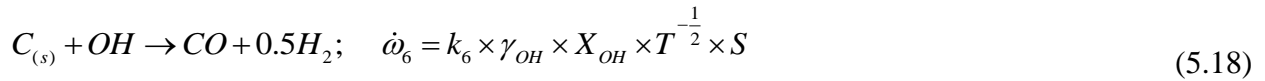
$$S = \pi d_p^2 N \text{ cm}^{-1} \tag{5.16}$$

Particle diameter, d_p is calculated using a mass balance of soot species density and particle number density.

$$d_p = \left[\frac{6\rho y_s}{\pi\rho_{C(s)}N} \right]^{1/3} \text{ cm} \quad (5.17)$$

$\rho_{C(s)}$ is the density of soot species.

In the OH oxidation step, a modified form of soot oxidation by hydroxyl is used.



γ_{OH} is the soot-OH collision efficiency, equal to 0.13, and X_{OH} is the OH mole fraction. The value of the rate constant k_6 is adjusted to match the experimental results and a value of $500 \text{ mol}^{-1} \text{ K}^{0.5} \text{ cm}^{-2} \text{ s}^{-1}$ is used in the present study.

5.5 Results

Non-reacting sprays

Three sets of non-evaporating spray experiments are modeled using the presented gas parcel model. Naber and Sieber's spray experiments injected diesel#2 into a constant volume optical chamber and measured the vapor penetrations at different ambient density conditions [128]. An injector of 0.257 mm orifice diameter was used in this experiment. Spray-A experiments from Sandia National Labs measured liquid and vapor penetrations of n-dodecane spray at an ambient density of 22.8 kg/m^3 [117]. In another recent study soy methyl ester (SME) was sprayed into a constant volume chamber and liquid and vapor penetrations were measured at different ambient temperatures [83]. In the simulations diesel#2 was modeled using the surrogate fuel, $C_{14}H_{30}$. The discrete component model was used for SME evaporation. The composition of

SME used in the study is provided in Table 5.1. A 3-D block of 10.8 cm height and 4 cm width is used to model the chamber. The 1mm mesh is used to discretize the domain. Turbulence was modeled using RNG k-epsilon model. The liquid spray was modeled using standard KIVA model with KH-RT break up models and collision model. The vapor penetration is measured as the maximum axial distance from the injector tip to the cell which contains 95% of the maximum vapor fraction.

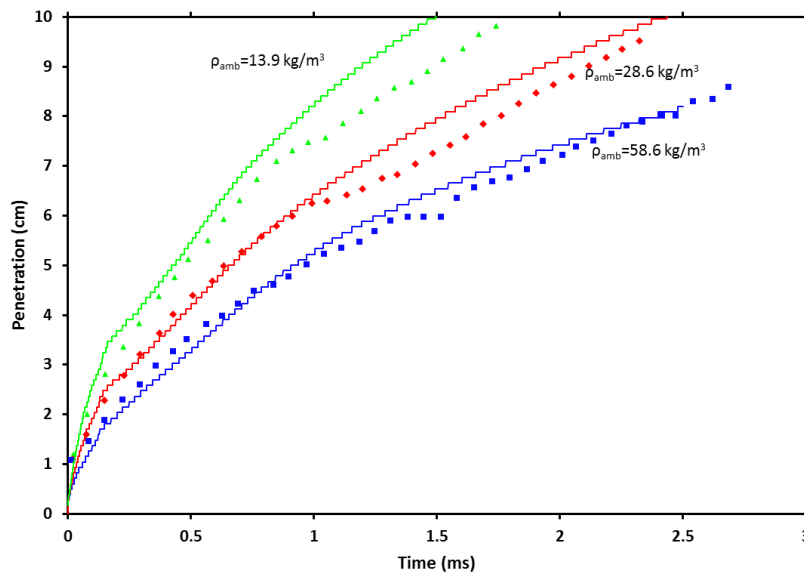


Figure 5.3 Diesel spray penetration data from experiments [128] and simulation at an ambient temperature of 1000K and different ambient densities

Using the gas parcel model, simulations were able to predict the diesel vapor penetrations in good agreement with the experimental results at different ambient densities as seen in Figure 5.3. The model was able to predict the decreasing penetration levels with increasing ambient density. It was observed that the model slightly over predicted the penetrations at low ambient density conditions. Also in the experimental data, between 1 ms and 1.5 ms, a small region was observed where vapor penetration seems to halt before further penetrating. The reason for this

behavior is unknown. However, the simulations were predicting rather smooth increase of vapor penetration. Nonetheless the model provided an improved vapor distribution when compared with the standard evaporation model.

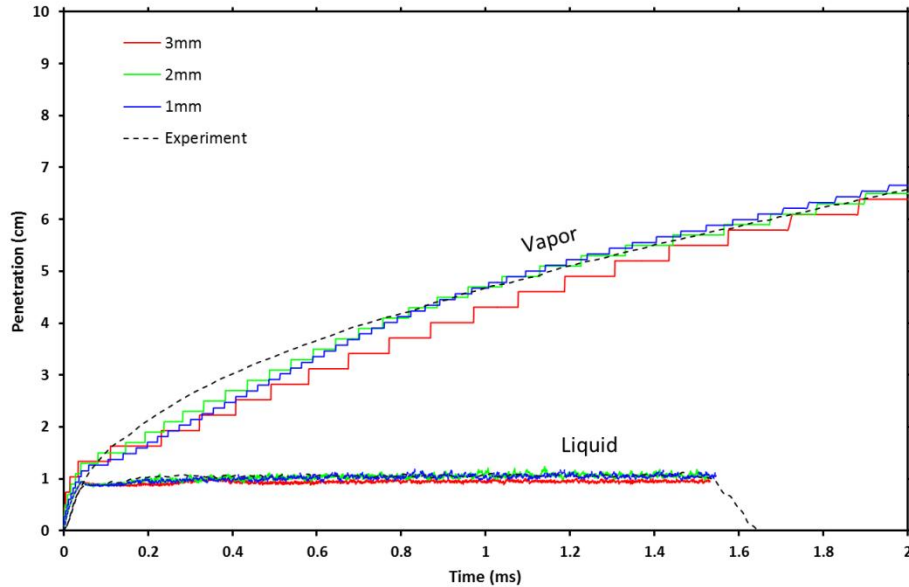


Figure 5.4 Experimental [117] and predicted liquid spray and fuel vapor penetration of n-dodecane spray at an ambient temperature of 900K.

Figure 5.4 shows the liquid and vapor penetrations of n-dodecane using gas parcel model compared with the experimental Sandia Spray A results from Engine Combustion Network (ECN). Figure 5.5 shows the comparison of predicted and measured penetrations of biodiesel spray and vapor at 900 K ambient temperature. Both these experiments were done at an ambient density of 22.8 kg/m^3 and ambient temperature of 900 K. The injector used also was identical with an orifice of diameter 0.090mm. It can be observed that the predicted penetrations are in good agreement with the experimental results. Figure 5.4 also shows the vapor penetration predicted using three different mesh sizes, varying from 3 mm to 1 mm. The coarse mesh slightly under predicted the liquid and vapor penetrations. The 2-mm and 1-mm meshes predicted vapor

penetrations very close to that of experimental measurements. The gas parcel model has resulted in significant improvement in the numerical results when compared to the prediction by the standard KIVA model as shown in Figure 5.1. The vapor penetrations predicted using the biodiesel spray was also in good agreement with the experimental results. Before 1 ms after the injection, a slight region of under prediction was observed in the vapor penetration from the model. This could be a limitation of gas parcel model, as there are not enough gas parcels during this period so as provide the additional momentum sources to accelerate the vaporized fuel. However as time progress, the gas parcels accumulate and the fuel vapor distribution are predicted close to the experimental observations.

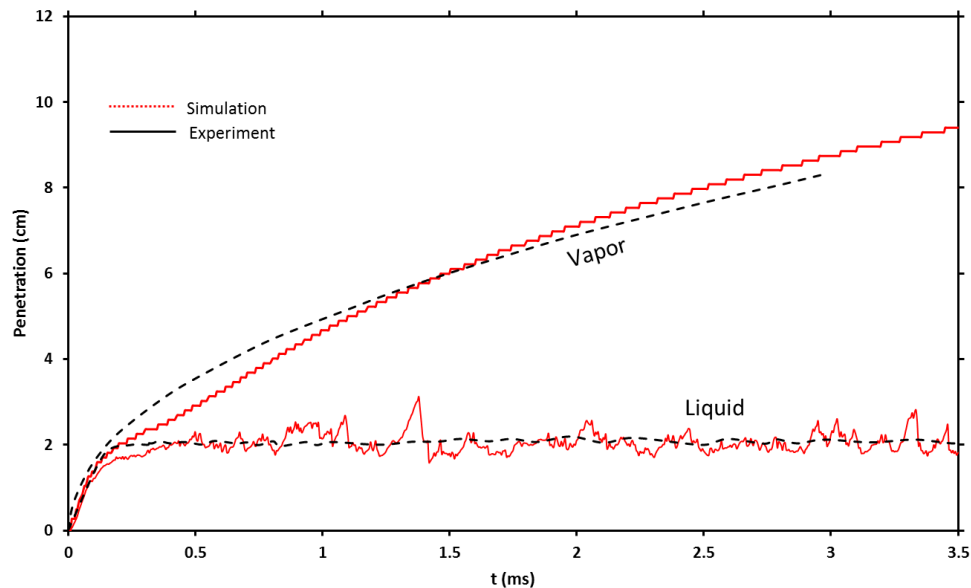


Figure 5.5 Experimental [83] and predicted liquid spray and fuel vapor penetrations of biodiesel at an ambient temperature of 900 K

In the SME spray models, the ambient density is kept at 22.8 kg/m^3 and the ambient temperatures used are 900 K and 1000 K. Figure 5.6 compares the liquid penetrations of biodiesel sprays at two different temperatures. The liquid penetrations are measured as the

maximum axial distance of the liquid droplets from the injector. The model was able to accurately capture the variation in the liquid spray with respect to the difference in the ambient temperature, i.e., liquid penetration is approximately 0.5 cm longer for the 900 K case than the 1000 K case. A slight under-prediction in the liquid length is observed initially before the droplets completely vaporize in the 900 K case.

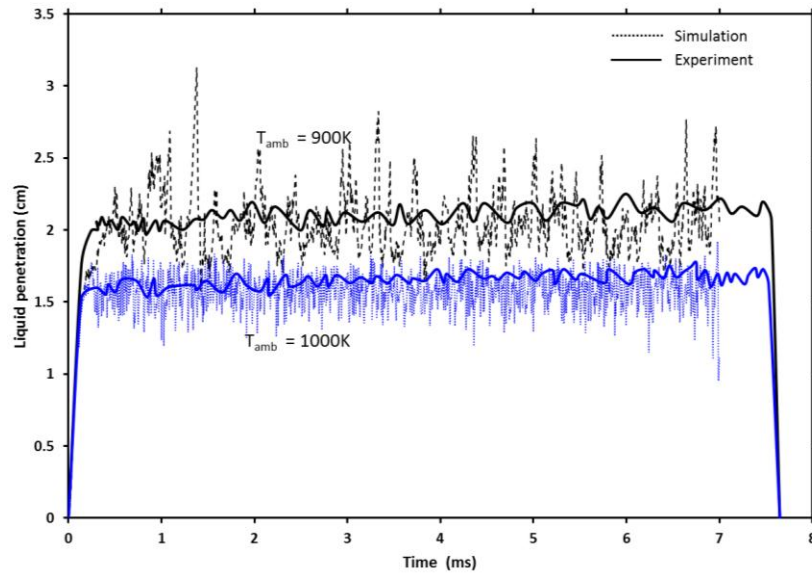


Figure 5.6 Experimental [83] and predicted liquid spray penetration of biodiesel at different ambient temperatures

The discrete component vaporization model is also validated against the experimental data on single droplet vaporization and biodiesel spray penetration. In the single droplet experiments, Rapeseed Methyl Ester (RME) was used to study vaporization characteristics [129]. In this simulation, the droplet was modeled using the discrete component model, and the initial droplet diameter is 0.7 mm. The ambient pressure is 0.1 MPa, and ambient temperatures are varied, i.e., 748K, 912K and 1019K. The d^2 -curves are shown in Figure 5.7. The results show that the present discrete component model is able to predict the biodiesel vaporization

characteristics, especially at lower ambient temperatures. At higher ambient temperatures, during the initial stage the model over-predicts the droplet diameter. This may arise from the homogeneous droplet temperature assumption, which results in faster temperature rise and density reduction of the biodiesel droplet. As the temperature reaches steady state, the droplet vaporization rate is accurately predicted by the model.

Table 5.1 FAME composition of RME [65] and SME [83] biodiesel

Biodiesel FAME Component (carbon length: unsaturated bonds)	RME Mass%	SME Mass%
Methyl Palmitate (C16:0)	3.52%	11.0%
Methyl Stearate (C18:0)	0.86%	4.0%
Methyl Oleate (C18:1)	64.9%	25.0%
Methyl Linoleate (C18:2)	22.5%	53.0%
Methyl Linolenate (C18:3)	8.29%	7.0%

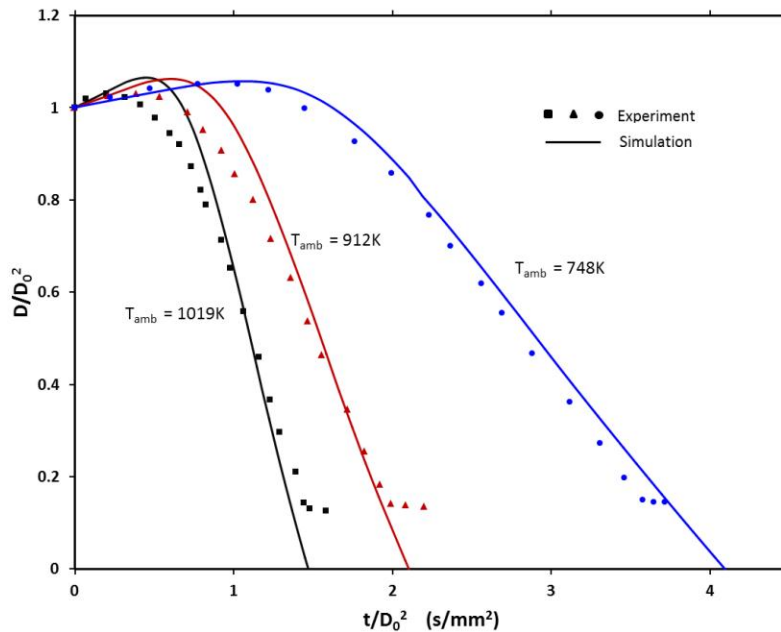


Figure 5.7 Comparison of experimental and predicted single droplet vaporization curves using biodiesel at different ambient temperatures

Reacting sprays

The combustion experiments conducted in the constant-volume chamber are also modeled using the aforementioned discrete component vaporization model and the multi-step soot model with detailed chemistry [83]. The combustion chamber is represented using a 2D axisymmetric domain with 108 mm in height and 124 mm in diameter. A 1 mm by 1 mm uniform mesh is used to discretize the domain. Diesel fuel liquid properties were modeled using tetradecane ($C_{14}H_{30}$) and the combustion chemistry is based on n-heptane (n- C_7H_{16}) reaction mechanism detailed in Chapter 3. Soy Methyl Ester (SME) was modeled using the SME composition as given in Table 5.1. Figure 5.8 shows the soot contours and the flame lift-off locations from the simulation and the experiment. The lift-off length is measured as the minimum axial location where OH species density reaches 50% of its maximum value at steady state. In the experiments, however, OH* is used to determine the lift-off lengths, which is different from the OH species used in the model. Nonetheless, the model was able to predict the sooting tendency correctly with respect to the fuel type and the ambient temperature.

Based on the aforementioned fuel chemistry and soot reactions, the present model predicts lower soot emissions for biodiesel than diesel fuel without adjustments to kinetics constants. At 1000 K ambient temperature, the predicted high soot regions agree with the measurements. As the ambient temperature decreases, the soot regions and lift-off locations move downstream because of long ignition delays. At 900 K ambient temperature, the predicted high soot regions are more upstream than the measurements. Nonetheless, the decrease in soot emissions for the 900 K case is captured by the model. It is also seen that the model predicts a drastic difference in soot emissions between diesel and biodiesel, more than that observed from the experiments.

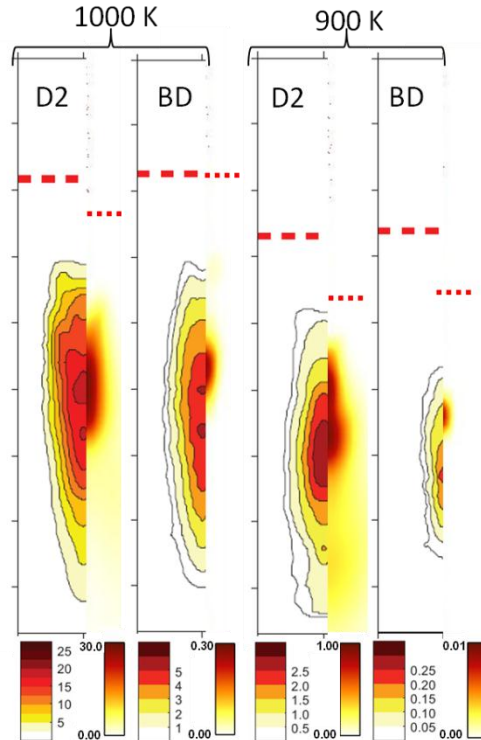


Figure 5.8 Experimental (left half) and simulation (right half) results showing soot contours (ppm) and flame lift-off location (dashed lines) using diesel fuel (D2) and biodiesel (BD) at 1000 K and 900 K ambient temperatures

The low soot emissions of biodiesel combustion can be due to many reasons. The oxygen content in biodiesel results in more complete combustion, even in the fuel rich zones. This provides a double advantage as it generates less soot as well as helps with the oxidation of soot already formed. In the soot model, this is simulated by the OH oxidation reaction. Biodiesel flame generates more OH species in the fuel rich zone, which reduces soot. Another major reason is the flame temperature. Biodiesel flame produces a higher temperature than diesel flame. This also helps with the soot oxidation. In the simulations, a wider region of high temperature is observed for biodiesel flame, as seen in Figure 5.9. This high temperature zone generates more thermal NO_x emissions. The absence of aromatics in the biodiesel is another

reason. These aromatics are considered as the soot precursors. This is not captured in the simulations as both diesel and biodiesel combustion is modeled using surrogate fuels. Overall the present numerical tool, a combination of multi-component vaporization model, detailed fuel chemistry, and multi-step soot model, is able to capture the effects of biodiesel fuel effects and ambient temperatures on the sooting tendency.

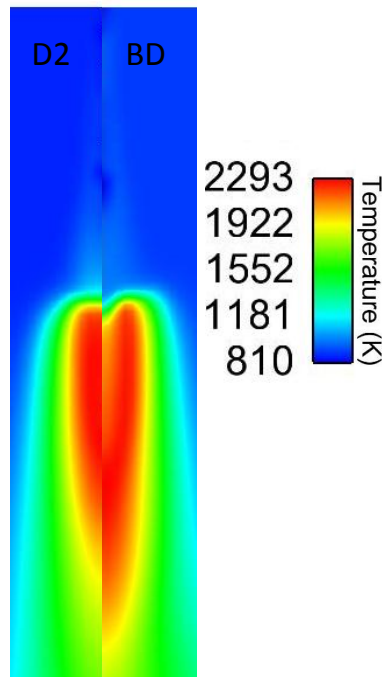


Figure 5.9 Temperature contours of diesel fuel (D2) and biodiesel (BD) flame at 5.5 ms at 900 K ambient temperature.

Engine simulation results

The proposed biodiesel chemistry and soot model was also applied to model engine experiments using a medium duty engine [82]. Table 5.2 lists the specifications of the engine and the operating conditions used for model validation. The simulations were conducted for at three different conditions, B100 fuel at 0% EGR, B100 fuel at 30% EGR and B20 fuel at 30% EGR.

An SOI sweep was provided at each of these conditions from -20 ATDC to +5 ATDC at each 5 degree intervals. A 60-degree sector mesh with periodic boundaries was used as the computation domain. The domain was meshed using a cylindrical grid with fine mesh near the axis and coarse mesh at the cylinder walls.

Table 5.2 John-Deere medium-duty diesel engine specifications

Engine	John-Deere 4045 HF475 4-Cylinder 4-valve direct injection
Bore X Stroke	106 mm X 127 mm
Compression ratio	17:1
Displacement	4.5 L
Connecting rod length	20.3 mm
Squish height	0.12 mm
Engine speed	1400 RPM
Piston	Articulated
Swirl	0.6
Maximum injection pressure	150 MPa
Injected fuel	50 mg/injection/cylinder
Injection duration	8 deg crank angle
Number of nozzle holes	6
Nozzle hole diameter	0.148 mm
Included spray angle	133.0 deg
Injection rate shape	Rising
Experimental conditions	SOI (ATDC)
A. B100, 0% EGR	-20, -15, -10, -5, 0, +5
B. B100, 30% EGR	-20, -15, -10, -5, 0, +5
C. B20, 30% EGR	-20, -15, -10, -5, 0, +5

Figure 5.10 shows the comparison of experimental results and simulation predictions at different operating conditions and SOI values. The model was able to predict qualitative trends in the soot levels at different SOI values. However the model was found to be more sensitive to EGR levels with B100 fuel than observed in the experiment. Overall the model predicted a higher level of soot using B20 fuel, which is in agreement with the experimental observations. As the soot model does not take in to account the aromatic composition in the fuel, using the same soot rates could result in over prediction of soot using biodiesel. Calibrating the soot rates for each fuel composition could help in overcoming this drawback and obtaining better soot predictions.

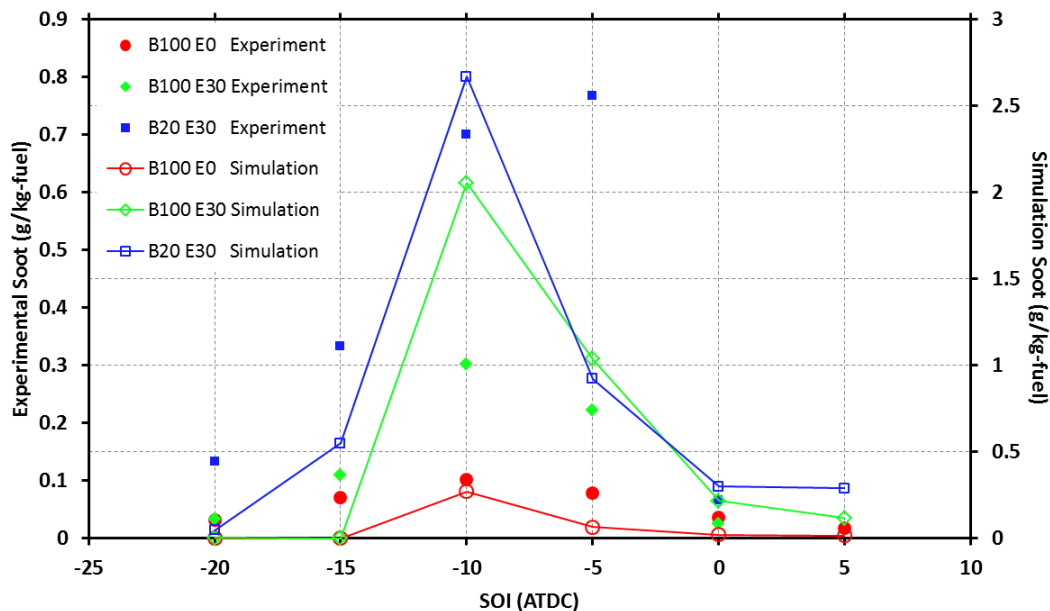


Figure 5.10 Comparison of measured and predicted soot

5.6 Summary

In this study, a gas parcel model was developed to improve the prediction of vapor penetrations of evaporating sprays. The model introduces artificial gas parcels, resulting from the

evaporating liquid droplets, into the domain. The gas parcel helps in improving the predicted vapor penetration by employing additional momentum sources beyond the liquid spray regions. The model was able to predict the vapor penetrations of fuel sprays under different operating conditions. A multi-component vaporization model was implemented in KIVA-3V to predict the evaporation rates of individual components in the fuel. The model was validated for single droplet vaporization history of RME at different ambient temperatures. This discrete component vaporization model was combined with detailed fuel chemistry and multi-step soot model to predict combustion of biodiesel and diesel sprays in a constant-volume chamber at high pressures and temperatures. The model was able to capture the characteristics of biodiesel sprays in liquid and vapor penetrations. The overall model was able to quantitatively predict the soot forming regions in the flame. As predicted by the model and validated by the experiments, biodiesel flame produces less soot than the diesel flame. The sooting trends with respect to the fuel type and ambient temperature are captured by the model. The mechanism was also able to predict the flame lift-off locations and flame temperatures of the different fuels reasonably well. The model results indicate that the presence of OH in the fuel rich zone and the higher flame temperature in biodiesel result in enhanced oxidation of soot. The biodiesel evaporation and combustion model was also applied to a medium-duty engine to predict the soot trends at different fuel injection timings using B100 and B20. It is anticipated that with proper calibrations, the present model can be used to study the biodiesel combustion and emission characteristics in a diesel engine under various operating conditions.

CHAPTER 6. CONCLUSIONS AND FUTURE RECOMMENDATIONS

6.1 Conclusions

Numerical modeling of pollutant formation in combustion systems using detailed chemical kinetics is performed in this research. A reduced reaction mechanism also containing fuel NO_x chemistry is developed to model producer gas combustion. Traditional diesel combustion mechanism is improved by the addition of detailed PAH chemistry. A multi-step soot model is implemented in KIVA-3V, a multi-dimensional CFD code widely used in engine modeling. The diesel spray and evaporation models are further improved by adding a gas parcel model and a multi-component evaporation model.

Using the reduced reaction mechanism to simulate producer gas combustion, NO_x emission characteristics in a practical burner was investigated. Fuel NO_x was found to be the major contributor of NO_x emissions using producer gas containing ammonia. It was also identified that high temperature fuel lean zones are the major NO producing sites. The NO emissions can be reduced by designing burner with wider high-temperature fuel rich zones. The emission performances of three new designs were studied using the developed reaction mechanism. The results suggested a burner with a bluff body in the flame region to effectively reduce the NO emissions. As the gasification technology progresses rapidly and gains wider acceptance, it is anticipated that this model can be used as a tool in designing low NO_x burners using producer gas derived from gasification of biomass.

A multi-step soot model coupled with PAH chemistry was used to model the sooting characteristics in diesel flames. The model was first applied in a constant-volume chamber to predict the soot forming locations in the flame. The model was able to predict the sooting regions and soot trends under different ambient conditions and EGR levels with reasonable accuracy.

Heavy-duty diesel engine experiments were simulated using the present n-heptane mechanism coupled with PAH chemistry and the multi-step soot model. The overall model was able to well predict the soot emissions over a range of fuel injection timings and EGR levels.

The gas parcel approach developed in this work was able to accurately predict the fuel vapor penetration using different fuel sprays under different operating conditions. The multi-component evaporation model was used to model the evaporation of biodiesel droplets and the results were in good agreement with experimental data, particularly after the initial expansion phase of droplets. The biodiesel evaporation model combined with the soot model was able to predict the sooting tendencies in diesel and biodiesel flames. In this study, a biodiesel reaction mechanism was coupled with additional chemical reactions for biodiesel components and PAH species. This model was further applied to model a medium-duty engine combustion using biodiesel-diesel mixtures at different EGR levels. The model was able to predict the soot emissions trends.

The reaction mechanisms and improved models developed in this study can be used in the future research of diesel engines. The soot model can be used as a tool to develop optimal combustion recipe for low temperature combustion modes. The discrete component model can be used to develop biodiesel combustion strategies and also in new combustion technology such as reactivity controlled compression ignition (RCCI).

6.2 Future Recommendations

Application and improvement of producer gas reaction mechanism

The model and reaction mechanism can be used to do a parametric study on 2D burner designs by varying the position and diameter of the bluff body. As the biomass feedstock varies,

so does the ammonia content in the syngas. It is of interest to model the combustion of producer gas from different feedstocks, especially ones with higher nitrogen content such as yellow corn.

One area of improvement in the producer gas combustion is the computer time. Even with multiple processors and reduced mechanism, the 3D simulations take three to four weeks to produce steady state results. Alternate strategies such as reduced-order model and dynamic reduction of the reaction mechanism can be investigated in order to reduce the computer time.

Application and improvements of diesel engine models

The multi-step soot model in the current study is calibrated manually based on available experimental data. A more accurate method will be to use optimization algorithms such as genetic algorithm or particle swarm optimization to minimize the prediction errors. As soot surface growth and oxidation by OH have been identified as the sensitive reaction steps, these two terms could be calibrated for different fuels such as diesel and biodiesel.

Another area of improvement is the reduction of reaction mechanisms. With the biodiesel mechanism and PAH chemistry, the total number of species tracked in the simulation is 95. The runtime varies from a few hours to a day depending on the mesh. As mentioned in the previous section, dynamic reduction and multi-zone models could be used to enhance the speed up.

The biodiesel reaction mechanism along with the additional reactions for biodiesel component species is not presently validated for ignition delay and flame speed properties. Although the burning characteristics of biodiesel as a whole are available, the characteristics of individual components are not currently available. The reaction rates of biodiesel components need to be calibrated with available fundamental experimental data so that the model can predict the effect of variation in biodiesel composition accurately.

One area of improvement with the use of the present gas parcel model is the need to address the over-prediction of cylinder pressure. The gas parcels produce a more diffused flame with leaner regions, which results in more rigorous combustion. As a result, the cylinder pressure is over-predicted. This is also observed in previous studies. More accurate modeling of turbulence-chemistry interaction can be the key to improving the combustion predictions using the gas parcel model.

The discrete component vaporization model and multi-step soot model can be further extended to other applications such as bio-oil gasification and bio-char formation. By adding bio-oil components to the fuel library, vaporization of bio-oil can be modeled. With appropriate chemistry to model gasification, the soot model methodology can be extended to model biochar formation.

APPENDIX A

Reduced mechanism developed for producer gas combustion

$$(k = A T^b \exp(-E/RT))$$

REACTIONS CONSIDERED	A	b	E
1. $2O+M \rightleftharpoons O_2+M$	1.20E+17	-1.0	0.0
H2 Enhanced by	2.400E+00		
H2O Enhanced by	1.540E+01		
CH4 Enhanced by	2.000E+00		
CO Enhanced by	1.750E+00		
CO2 Enhanced by	3.600E+00		
C2H6 Enhanced by	3.000E+00		
AR Enhanced by	8.300E-01		
2. $O+H+M \rightleftharpoons OH+M$	5.00E+17	-1.0	0.0
H2 Enhanced by	2.000E+00		
H2O Enhanced by	6.000E+00		
CH4 Enhanced by	2.000E+00		
CO Enhanced by	1.500E+00		
CO2 Enhanced by	2.000E+00		
C2H6 Enhanced by	3.000E+00		
AR Enhanced by	7.000E-01		
3. $O+H_2 \rightleftharpoons H+OH$	3.87E+04	2.7	6260.0
4. $O+HO_2 \rightleftharpoons OH+O_2$	2.00E+13	0.0	0.0
5. $O+H_2O_2 \rightleftharpoons OH+HO_2$	9.63E+06	2.0	4000.0
6. $O+CH \rightleftharpoons H+CO$	5.70E+13	0.0	0.0
7. $O+CH_2 \rightleftharpoons H+HCO$	8.00E+13	0.0	0.0
8. $O+CH_2(S) \rightleftharpoons H_2+CO$	1.50E+13	0.0	0.0
9. $O+CH_2(S) \rightleftharpoons H+HCO$	1.50E+13	0.0	0.0
10. $O+CH_3 \rightleftharpoons H+CH_2O$	5.06E+13	0.0	0.0
11. $O+CH_4 \rightleftharpoons OH+CH_3$	1.02E+09	1.5	8600.0
12. $O+CO(+M) \rightleftharpoons CO_2(+M)$	1.80E+10	0.0	2385.0
Low pressure limit:	0.60200E+15	0.00000E+00	0.30000E+04
H2 Enhanced by	2.000E+00		
O2 Enhanced by	6.000E+00		
H2O Enhanced by	6.000E+00		
CH4 Enhanced by	2.000E+00		
CO Enhanced by	1.500E+00		
CO2 Enhanced by	3.500E+00		
C2H6 Enhanced by	3.000E+00		
AR Enhanced by	5.000E-01		
13. $O+HCO \rightleftharpoons OH+CO$	3.00E+13	0.0	0.0
14. $O+HCO \rightleftharpoons H+CO_2$	3.00E+13	0.0	0.0
15. $O+CH_2O \rightleftharpoons OH+HCO$	3.90E+13	0.0	3540.0
16. $O+CH_2OH \rightleftharpoons OH+CH_2O$	1.00E+13	0.0	0.0
17. $O+CH_3O \rightleftharpoons OH+CH_2O$	1.00E+13	0.0	0.0
18. $O+CH_3OH \rightleftharpoons OH+CH_2OH$	3.88E+05	2.5	3100.0
19. $O+CH_3OH \rightleftharpoons OH+CH_3O$	1.30E+05	2.5	5000.0
20. $O+C_2H_4 \rightleftharpoons CH_3+HCO$	1.25E+07	1.8	220.0
21. $O+C_2H_5 \rightleftharpoons CH_3+CH_2O$	2.24E+13	0.0	0.0

22.	$O+C_2H_6 \rightleftharpoons OH+C_2H_5$	8.98E+07	1.9	5690.0	
23.	$O_2+CO \rightleftharpoons O+CO_2$	2.50E+12	0.0	47800.0	
24.	$O_2+CH_2O \rightleftharpoons HO_2+HCO$	1.00E+14	0.0	40000.0	
25.	$H+O_2+M \rightleftharpoons HO_2+M$	2.80E+18	-0.9	0.0	
	O2	Enhanced by	0.000E+00		
	H2O	Enhanced by	0.000E+00		
	CO	Enhanced by	7.500E-01		
	CO2	Enhanced by	1.500E+00		
	C2H6	Enhanced by	1.500E+00		
	N2	Enhanced by	0.000E+00		
	AR	Enhanced by	0.000E+00		
26.	$H+2O_2 \rightleftharpoons HO_2+O_2$	2.08E+19	-1.2	0.0	
27.	$H+O_2+H_2O \rightleftharpoons HO_2+H_2O$	1.13E+19	-0.8	0.0	
28.	$H+O_2+N_2 \rightleftharpoons HO_2+N_2$	2.60E+19	-1.2	0.0	
29.	$H+O_2+AR \rightleftharpoons HO_2+AR$	7.00E+17	-0.8	0.0	
30.	$H+O_2 \rightleftharpoons O+OH$	2.65E+16	-0.7	17041.0	
31.	$2H+M \rightleftharpoons H_2+M$	1.00E+18	-1.0	0.0	
	H2	Enhanced by	0.000E+00		
	H2O	Enhanced by	0.000E+00		
	CH4	Enhanced by	2.000E+00		
	CO2	Enhanced by	0.000E+00		
	C2H6	Enhanced by	3.000E+00		
	AR	Enhanced by	6.300E-01		
32.	$2H+H_2 \rightleftharpoons 2H_2$	9.00E+16	-0.6	0.0	
33.	$2H+H_2O \rightleftharpoons H_2+H_2O$	6.00E+19	-1.2	0.0	
34.	$2H+CO_2 \rightleftharpoons H_2+CO_2$	5.50E+20	-2.0	0.0	
35.	$H+OH+M \rightleftharpoons H_2O+M$	2.20E+22	-2.0	0.0	
	H2	Enhanced by	7.300E-01		
	H2O	Enhanced by	3.650E+00		
	CH4	Enhanced by	2.000E+00		
	C2H6	Enhanced by	3.000E+00		
	AR	Enhanced by	3.800E-01		
36.	$H+HO_2 \rightleftharpoons O+H_2O$	3.97E+12	0.0	671.0	
37.	$H+HO_2 \rightleftharpoons O_2+H_2$	4.48E+13	0.0	1068.0	
38.	$H+HO_2 \rightleftharpoons 2OH$	8.40E+13	0.0	635.0	
39.	$H+H_2O_2 \rightleftharpoons HO_2+H_2$	1.21E+07	2.0	5200.0	
40.	$H+H_2O_2 \rightleftharpoons OH+H_2O$	1.00E+13	0.0	3600.0	
41.	$H+CH \rightleftharpoons C+H_2$	1.65E+14	0.0	0.0	
42.	$H+CH_2(+M) \rightleftharpoons CH_3(+M)$	6.00E+14	0.0	0.0	
	Low pressure limit:	0.10400E+27	-0.27600E+01	0.16000E+04	
	TROE centering:	0.56200E+00	0.91000E+02	0.58360E+04	0.85520E+04
	H2	Enhanced by	2.000E+00		
	H2O	Enhanced by	6.000E+00		
	CH4	Enhanced by	2.000E+00		
	CO	Enhanced by	1.500E+00		
	CO2	Enhanced by	2.000E+00		
	C2H6	Enhanced by	3.000E+00		
	AR	Enhanced by	7.000E-01		
43.	$H+CH_2(S) \rightleftharpoons CH+H_2$	3.00E+13	0.0	0.0	
44.	$H+CH_3(+M) \rightleftharpoons CH_4(+M)$	1.39E+16	-0.5	536.0	
	Low pressure limit:	0.26200E+34	-0.47600E+01	0.24400E+04	
	TROE centering:	0.78300E+00	0.74000E+02	0.29410E+04	0.69640E+04
	H2	Enhanced by	2.000E+00		
	H2O	Enhanced by	6.000E+00		
	CH4	Enhanced by	3.000E+00		
	CO	Enhanced by	1.500E+00		

CO2 Enhanced by 2.000E+00
 C2H6 Enhanced by 3.000E+00
 AR Enhanced by 7.000E-01
 45. H+CH4<=>CH3+H2 6.60E+08 1.6 10840.0
 46. H+HCO(+M)<=>CH2O(+M) 1.09E+12 0.5 -260.0
 Low pressure limit: 0.24700E+25 -0.25700E+01 0.42500E+03
 TROE centering: 0.78240E+00 0.27100E+03 0.27550E+04 0.65700E+04
 H2 Enhanced by 2.000E+00
 H2O Enhanced by 6.000E+00
 CH4 Enhanced by 2.000E+00
 CO Enhanced by 1.500E+00
 CO2 Enhanced by 2.000E+00
 C2H6 Enhanced by 3.000E+00
 AR Enhanced by 7.000E-01
 47. H+HCO<=>H2+CO 7.34E+13 0.0 0.0
 48. H+CH2O(+M)<=>CH2OH(+M) 5.40E+11 0.5 3600.0
 Low pressure limit: 0.12700E+33 -0.48200E+01 0.65300E+04
 TROE centering: 0.71870E+00 0.10300E+03 0.12910E+04 0.41600E+04
 H2 Enhanced by 2.000E+00
 H2O Enhanced by 6.000E+00
 CH4 Enhanced by 2.000E+00
 CO Enhanced by 1.500E+00
 CO2 Enhanced by 2.000E+00
 C2H6 Enhanced by 3.000E+00
 49. H+CH2O(+M)<=>CH3O(+M) 5.40E+11 0.5 2600.0
 Low pressure limit: 0.22000E+31 -0.48000E+01 0.55600E+04
 TROE centering: 0.75800E+00 0.94000E+02 0.15550E+04 0.42000E+04
 H2 Enhanced by 2.000E+00
 H2O Enhanced by 6.000E+00
 CH4 Enhanced by 2.000E+00
 CO Enhanced by 1.500E+00
 CO2 Enhanced by 2.000E+00
 C2H6 Enhanced by 3.000E+00
 50. H+CH2O<=>HCO+H2 5.74E+07 1.9 2742.0
 51. H+CH2OH(+M)<=>CH3OH(+M) 1.06E+12 0.5 86.0
 Low pressure limit: 0.43600E+32 -0.46500E+01 0.50800E+04
 TROE centering: 0.60000E+00 0.10000E+03 0.90000E+05 0.10000E+05
 H2 Enhanced by 2.000E+00
 H2O Enhanced by 6.000E+00
 CH4 Enhanced by 2.000E+00
 CO Enhanced by 1.500E+00
 CO2 Enhanced by 2.000E+00
 C2H6 Enhanced by 3.000E+00
 52. H+CH2OH<=>H2+CH2O 2.00E+13 0.0 0.0
 53. H+CH2OH<=>OH+CH3 1.65E+11 0.7 -284.0
 54. H+CH2OH<=>CH2(S)+H2O 3.28E+13 -0.1 610.0
 55. H+CH3O(+M)<=>CH3OH(+M) 2.43E+12 0.5 50.0
 Low pressure limit: 0.46600E+42 -0.74400E+01 0.14080E+05
 TROE centering: 0.70000E+00 0.10000E+03 0.90000E+05 0.10000E+05
 H2 Enhanced by 2.000E+00
 H2O Enhanced by 6.000E+00
 CH4 Enhanced by 2.000E+00
 CO Enhanced by 1.500E+00
 CO2 Enhanced by 2.000E+00
 C2H6 Enhanced by 3.000E+00
 56. H+CH3O<=>H+CH2OH 4.15E+07 1.6 1924.0

57. $\text{H}+\text{CH}_3\text{O}\rightleftharpoons\text{H}_2+\text{CH}_2\text{O}$ 2.00E+13 0.0 0.0
 58. $\text{H}+\text{CH}_3\text{O}\rightleftharpoons\text{OH}+\text{CH}_3$ 1.50E+12 0.5 -110.0
 59. $\text{H}+\text{CH}_3\text{O}\rightleftharpoons\text{CH}_2(\text{S})+\text{H}_2\text{O}$ 2.62E+14 -0.2 1070.0
 60. $\text{H}+\text{CH}_3\text{OH}\rightleftharpoons\text{CH}_2\text{OH}+\text{H}_2$ 1.70E+07 2.1 4870.0
 61. $\text{H}+\text{CH}_3\text{OH}\rightleftharpoons\text{CH}_3\text{O}+\text{H}_2$ 4.20E+06 2.1 4870.0
 62. $\text{H}+\text{C}_2\text{H}_4(+\text{M})\rightleftharpoons\text{C}_2\text{H}_5(+\text{M})$ 5.40E+11 0.5 1820.0
 Low pressure limit: 0.60000E+42 -0.76200E+01 0.69700E+04
 TROE centering: 0.97530E+00 0.21000E+03 0.98400E+03 0.43740E+04
 H2 Enhanced by 2.000E+00
 H2O Enhanced by 6.000E+00
 CH4 Enhanced by 2.000E+00
 CO Enhanced by 1.500E+00
 CO2 Enhanced by 2.000E+00
 C2H6 Enhanced by 3.000E+00
 AR Enhanced by 7.000E-01
 63. $\text{H}+\text{C}_2\text{H}_5(+\text{M})\rightleftharpoons\text{C}_2\text{H}_6(+\text{M})$ 5.21E+17 -1.0 1580.0
 Low pressure limit: 0.19900E+42 -0.70800E+01 0.66850E+04
 TROE centering: 0.84220E+00 0.12500E+03 0.22190E+04 0.68820E+04
 H2 Enhanced by 2.000E+00
 H2O Enhanced by 6.000E+00
 CH4 Enhanced by 2.000E+00
 CO Enhanced by 1.500E+00
 CO2 Enhanced by 2.000E+00
 C2H6 Enhanced by 3.000E+00
 AR Enhanced by 7.000E-01
 64. $\text{H}+\text{C}_2\text{H}_5\rightleftharpoons\text{H}_2+\text{C}_2\text{H}_4$ 2.00E+12 0.0 0.0
 65. $\text{H}+\text{C}_2\text{H}_6\rightleftharpoons\text{C}_2\text{H}_5+\text{H}_2$ 1.15E+08 1.9 7530.0
 66. $\text{H}_2+\text{CO}(+\text{M})\rightleftharpoons\text{CH}_2\text{O}(+\text{M})$ 4.30E+07 1.5 79600.0
 Low pressure limit: 0.50700E+28 -0.34200E+01 0.84350E+05
 TROE centering: 0.93200E+00 0.19700E+03 0.15400E+04 0.10300E+05
 H2 Enhanced by 2.000E+00
 H2O Enhanced by 6.000E+00
 CH4 Enhanced by 2.000E+00
 CO Enhanced by 1.500E+00
 CO2 Enhanced by 2.000E+00
 C2H6 Enhanced by 3.000E+00
 AR Enhanced by 7.000E-01
 67. $\text{OH}+\text{H}_2\rightleftharpoons\text{H}+\text{H}_2\text{O}$ 2.16E+08 1.5 3430.0
 68. $2\text{OH}(+\text{M})\rightleftharpoons\text{H}_2\text{O}_2(+\text{M})$ 7.40E+13 -0.4 0.0
 Low pressure limit: 0.23000E+19 -0.90000E+00 -0.17000E+04
 TROE centering: 0.73460E+00 0.94000E+02 0.17560E+04 0.51820E+04
 H2 Enhanced by 2.000E+00
 H2O Enhanced by 6.000E+00
 CH4 Enhanced by 2.000E+00
 CO Enhanced by 1.500E+00
 CO2 Enhanced by 2.000E+00
 C2H6 Enhanced by 3.000E+00
 AR Enhanced by 7.000E-01
 69. $2\text{OH}\rightleftharpoons\text{O}+\text{H}_2\text{O}$ 3.57E+04 2.4 -2110.0
 70. $\text{OH}+\text{HO}_2\rightleftharpoons\text{O}_2+\text{H}_2\text{O}$ 1.45E+13 0.0 -500.0
 Declared duplicate reaction...
 71. $\text{OH}+\text{H}_2\text{O}_2\rightleftharpoons\text{HO}_2+\text{H}_2\text{O}$ 2.00E+12 0.0 427.0
 Declared duplicate reaction...
 72. $\text{OH}+\text{H}_2\text{O}_2\rightleftharpoons\text{HO}_2+\text{H}_2\text{O}$ 1.70E+18 0.0 29410.0
 Declared duplicate reaction...
 73. $\text{OH}+\text{C}\rightleftharpoons\text{H}+\text{CO}$ 5.00E+13 0.0 0.0

74. OH+CH<=>H+HCO	3.00E+13	0.0	0.0
75. OH+CH2<=>H+CH2O	2.00E+13	0.0	0.0
76. OH+CH2<=>CH+H2O	1.13E+07	2.0	3000.0
77. OH+CH2(S)<=>H+CH2O	3.00E+13	0.0	0.0
78. OH+CH3(+M)<=>CH3OH(+M)	2.79E+18	-1.4	1330.0
Low pressure limit: 0.40000E+37 -0.59200E+01 0.31400E+04			
TROE centering: 0.41200E+00 0.19500E+03 0.59000E+04 0.63940E+04			
H2	Enhanced by	2.000E+00	
H2O	Enhanced by	6.000E+00	
CH4	Enhanced by	2.000E+00	
CO	Enhanced by	1.500E+00	
CO2	Enhanced by	2.000E+00	
C2H6	Enhanced by	3.000E+00	
79. OH+CH3<=>CH2+H2O	5.60E+07	1.6	5420.0
80. OH+CH3<=>CH2(S)+H2O	6.44E+17	-1.3	1417.0
81. OH+CH4<=>CH3+H2O	1.00E+08	1.6	3120.0
82. OH+CO<=>H+CO2	4.76E+07	1.2	70.0
83. OH+HCO<=>H2O+CO	5.00E+13	0.0	0.0
84. OH+CH2O<=>HCO+H2O	3.43E+09	1.2	-447.0
85. OH+CH2OH<=>H2O+CH2O	5.00E+12	0.0	0.0
86. OH+CH3O<=>H2O+CH2O	5.00E+12	0.0	0.0
87. OH+CH3OH<=>CH2OH+H2O	1.44E+06	2.0	-840.0
88. OH+CH3OH<=>CH3O+H2O	6.30E+06	2.0	1500.0
89. OH+C2H6<=>C2H5+H2O	3.54E+06	2.1	870.0
90. 2HO2<=>O2+H2O2	1.30E+11	0.0	-1630.0
Declared duplicate reaction...			
91. 2HO2<=>O2+H2O2	4.20E+14	0.0	12000.0
Declared duplicate reaction...			
92. HO2+CH2<=>OH+CH2O	2.00E+13	0.0	0.0
93. HO2+CH3<=>O2+CH4	1.00E+12	0.0	0.0
94. HO2+CH3<=>OH+CH3O	3.78E+13	0.0	0.0
95. HO2+CO<=>OH+CO2	1.50E+14	0.0	23600.0
96. HO2+CH2O<=>HCO+H2O2	5.60E+06	2.0	12000.0
97. C+O2<=>O+CO	5.80E+13	0.0	576.0
98. CH+O2<=>O+HCO	6.71E+13	0.0	0.0
99. CH+H2<=>H+CH2	1.08E+14	0.0	3110.0
100. CH+H2O<=>H+CH2O	5.71E+12	0.0	-755.0
101. CH+CH4<=>H+C2H4	6.00E+13	0.0	0.0
102. CH+CO2<=>HCO+CO	1.90E+14	0.0	15792.0
103. CH2+O2=>OH+H+CO	5.00E+12	0.0	1500.0
104. CH2+H2<=>H+CH3	5.00E+05	2.0	7230.0
105. CH2+CH3<=>H+C2H4	4.00E+13	0.0	0.0
106. CH2+CH4<=>2CH3	2.46E+06	2.0	8270.0
107. CH2(S)+N2<=>CH2+N2	1.50E+13	0.0	600.0
108. CH2(S)+AR<=>CH2+AR	9.00E+12	0.0	600.0
109. CH2(S)+O2<=>H+OH+CO	2.80E+13	0.0	0.0
110. CH2(S)+O2<=>CO+H2O	1.20E+13	0.0	0.0
111. CH2(S)+H2<=>CH3+H	7.00E+13	0.0	0.0
112. CH2(S)+H2O(+M)<=>CH3OH(+M)	4.82E+17	-1.2	1145.0
Low pressure limit: 0.18800E+39 -0.63600E+01 0.50400E+04			
TROE centering: 0.60270E+00 0.20800E+03 0.39220E+04 0.10180E+05			
H2	Enhanced by	2.000E+00	
H2O	Enhanced by	6.000E+00	
CH4	Enhanced by	2.000E+00	
CO	Enhanced by	1.500E+00	
CO2	Enhanced by	2.000E+00	

C2H6	Enhanced by	3.000E+00			
113. CH2(S)+H2O<=>CH2+H2O		3.00E+13	0.0	0.0	
114. CH2(S)+CH3<=>H+C2H4		1.20E+13	0.0	-570.0	
115. CH2(S)+CH4<=>2CH3		1.60E+13	0.0	-570.0	
116. CH2(S)+CO<=>CH2+CO		9.00E+12	0.0	0.0	
117. CH2(S)+CO2<=>CH2+CO2		7.00E+12	0.0	0.0	
118. CH2(S)+CO2<=>CO+CH2O		1.40E+13	0.0	0.0	
119. CH2(S)+C2H6<=>CH3+C2H5		4.00E+13	0.0	-550.0	
120. CH3+O2<=>O+CH3O		3.56E+13	0.0	30480.0	
121. CH3+O2<=>OH+CH2O		2.31E+12	0.0	20315.0	
122. CH3+H2O2<=>HO2+CH4		2.45E+04	2.5	5180.0	
123. 2CH3(+M)<=>C2H6(+M)		6.77E+16	-1.2	654.0	
Low pressure limit: 0.34000E+42 -0.70300E+01 0.27620E+04					
TROE centering: 0.61900E+00 0.73200E+02 0.11800E+04 0.99990E+04					
H2	Enhanced by	2.000E+00			
H2O	Enhanced by	6.000E+00			
CH4	Enhanced by	2.000E+00			
CO	Enhanced by	1.500E+00			
CO2	Enhanced by	2.000E+00			
C2H6	Enhanced by	3.000E+00			
AR	Enhanced by	7.000E-01			
124. 2CH3<=>H+C2H5		6.84E+12	0.1	10600.0	
125. CH3+HCO<=>CH4+CO		2.65E+13	0.0	0.0	
126. CH3+CH2O<=>HCO+CH4		3.32E+03	2.8	5860.0	
127. CH3+CH3OH<=>CH2OH+CH4		3.00E+07	1.5	9940.0	
128. CH3+CH3OH<=>CH3O+CH4		1.00E+07	1.5	9940.0	
129. CH3+C2H6<=>C2H5+CH4		6.14E+06	1.7	10450.0	
130. HCO+H2O<=>H+CO+H2O		1.50E+18	-1.0	17000.0	
131. HCO+M<=>H+CO+M		1.87E+17	-1.0	17000.0	
H2	Enhanced by	2.000E+00			
H2O	Enhanced by	0.000E+00			
CH4	Enhanced by	2.000E+00			
CO	Enhanced by	1.500E+00			
CO2	Enhanced by	2.000E+00			
C2H6	Enhanced by	3.000E+00			
132. HCO+O2<=>HO2+CO		1.34E+13	0.0	400.0	
133. CH2OH+O2<=>HO2+CH2O		1.80E+13	0.0	900.0	
134. CH3O+O2<=>HO2+CH2O		4.28E-13	7.6	-3530.0	
135. C2H5+O2<=>HO2+C2H4		8.40E+11	0.0	3875.0	
136. N+NO<=>N2+O		2.70E+13	0.0	355.0	
137. N+O2<=>NO+O		9.00E+09	1.0	6500.0	
138. N+OH<=>NO+H		3.36E+13	0.0	385.0	
139. HO2+NO<=>NO2+OH		2.11E+12	0.0	-480.0	
140. NO+O+M<=>NO2+M		1.06E+20	-1.4	0.0	
H2	Enhanced by	2.000E+00			
H2O	Enhanced by	6.000E+00			
CH4	Enhanced by	2.000E+00			
CO	Enhanced by	1.500E+00			
CO2	Enhanced by	2.000E+00			
C2H6	Enhanced by	3.000E+00			
AR	Enhanced by	7.000E-01			
141. NO2+O<=>NO+O2		3.90E+12	0.0	-240.0	
142. NO2+H<=>NO+OH		1.32E+14	0.0	360.0	
143. NH+O<=>NO+H		4.00E+13	0.0	0.0	
144. NH+H<=>N+H2		3.20E+13	0.0	330.0	
145. NH+OH<=>N+H2O		2.00E+09	1.2	0.0	

146.	NH+O2<=>NO+OH	1.28E+06	1.5	100.0
147.	NH+N<=>N2+H	1.50E+13	0.0	0.0
148.	NH+NO<=>N2+OH	2.16E+13	-0.2	0.0
149.	NH2+O<=>OH+NH	3.00E+12	0.0	0.0
150.	NH2+H<=>NH+H2	4.00E+13	0.0	3650.0
151.	NH2+OH<=>NH+H2O	9.00E+07	1.5	-460.0
152.	NNH<=>N2+H	3.30E+08	0.0	0.0
153.	NNH+M<=>N2+H+M	1.30E+14	-0.1	4980.0
	H2	Enhanced by	2.000E+00	
	H2O	Enhanced by	6.000E+00	
	CH4	Enhanced by	2.000E+00	
	CO	Enhanced by	1.500E+00	
	CO2	Enhanced by	2.000E+00	
	C2H6	Enhanced by	3.000E+00	
	AR	Enhanced by	7.000E-01	
154.	NNH+O2<=>HO2+N2	5.00E+12	0.0	0.0
155.	NNH+O<=>OH+N2	2.50E+13	0.0	0.0
156.	NNH+O<=>NH+NO	7.00E+13	0.0	0.0
157.	NNH+H<=>H2+N2	5.00E+13	0.0	0.0
158.	NNH+OH<=>H2O+N2	2.00E+13	0.0	0.0
159.	NNH+CH3<=>CH4+N2	2.50E+13	0.0	0.0
160.	CN+O<=>CO+N	7.70E+13	0.0	0.0
161.	CN+H2O<=>HCN+OH	8.00E+12	0.0	7460.0
162.	CN+H2<=>HCN+H	2.95E+05	2.5	2240.0
163.	HCN+M<=>H+CN+M	1.04E+29	-3.3	126600.0
	H2	Enhanced by	2.000E+00	
	H2O	Enhanced by	6.000E+00	
	CH4	Enhanced by	2.000E+00	
	CO	Enhanced by	1.500E+00	
	CO2	Enhanced by	2.000E+00	
	C2H6	Enhanced by	3.000E+00	
	AR	Enhanced by	7.000E-01	
164.	HCN+O<=>NH+CO	5.07E+03	2.6	4980.0
165.	HCN+O<=>CN+OH	3.91E+09	1.6	26600.0
166.	HCN+OH<=>HOCN+H	1.10E+06	2.0	13370.0
167.	HCN+OH<=>HNCO+H	4.40E+03	2.3	6400.0
168.	HCN+OH<=>NH2+CO	1.60E+02	2.6	9000.0
169.	C+N2<=>CN+N	6.30E+13	0.0	46020.0
170.	CH+N2<=>HCN+N	3.12E+09	0.9	20130.0
171.	CH2+N2<=>HCN+NH	1.00E+13	0.0	74000.0
172.	CH2(S)+N2<=>NH+HCN	1.00E+11	0.0	65000.0
173.	C+NO<=>CN+O	1.90E+13	0.0	0.0
174.	C+NO<=>CO+N	2.90E+13	0.0	0.0
175.	CH+NO<=>HCN+O	4.10E+13	0.0	0.0
176.	CH+NO<=>N+HCO	2.46E+13	0.0	0.0
177.	CH2+NO<=>H+HNCO	3.10E+17	-1.4	1270.0
178.	CH2+NO<=>OH+HCN	2.90E+14	-0.7	760.0
179.	CH2(S)+NO<=>H+HNCO	3.10E+17	-1.4	1270.0
180.	CH2(S)+NO<=>OH+HCN	2.90E+14	-0.7	760.0
181.	CH3+NO<=>HCN+H2O	9.60E+13	0.0	28800.0
182.	HNCO+O<=>NH+CO2	9.80E+07	1.4	8500.0
183.	HNCO+H<=>NH2+CO	2.25E+07	1.7	3800.0
184.	HNCO+OH<=>NH2+CO2	3.30E+06	1.5	3600.0
185.	HNCO+M<=>NH+CO+M	1.18E+16	0.0	84720.0
	H2	Enhanced by	2.000E+00	
	H2O	Enhanced by	6.000E+00	

CH4	Enhanced by	2.000E+00			
CO	Enhanced by	1.500E+00			
CO2	Enhanced by	2.000E+00			
C2H6	Enhanced by	3.000E+00			
AR	Enhanced by	7.000E-01			
186. HOCN+H<=>H+HNCO		2.00E+07	2.0	2000.0	
187. CH3+N<=>HCN+H2		3.70E+12	0.1	-90.0	
188. NH3+H<=>NH2+H2		5.40E+05	2.4	9915.0	
189. NH3+OH<=>NH2+H2O		5.00E+07	1.6	955.0	
190. NH3+O<=>NH2+OH		9.40E+06	1.9	6460.0	
191. N+CO2<=>NO+CO		3.00E+12	0.0	11300.0	
192. O+CH3=>H+H2+CO		3.37E+13	0.0	0.0	
193. OH+HO2<=>O2+H2O		5.00E+15	0.0	17330.0	
Declared duplicate reaction...					
194. OH+CH3=>H2+CH2O		8.00E+09	0.5	-1755.0	
195. CH+H2(+M)<=>CH3(+M)		1.97E+12	0.4	-370.0	
Low pressure limit: 0.48200E+26 -0.28000E+01 0.59000E+03					
TROE centering: 0.57800E+00 0.12200E+03 0.25350E+04 0.93650E+04					
H2	Enhanced by	2.000E+00			
H2O	Enhanced by	6.000E+00			
CH4	Enhanced by	2.000E+00			
CO	Enhanced by	1.500E+00			
CO2	Enhanced by	2.000E+00			
C2H6	Enhanced by	3.000E+00			
AR	Enhanced by	7.000E-01			
196. CH2+O2=>2H+CO2		5.80E+12	0.0	1500.0	
197. CH2+O2<=>O+CH2O		2.40E+12	0.0	1500.0	
198. CH2(S)+H2O=>H2+CH2O		6.82E+10	0.2	-935.0	

NOTE: A units mole-cm-sec-K, E units cal/mole

15. $c_3h_4+oh=c_2h_4+hco$	1.00E+12	0.0	0.0
16. $ch_3+ho_2=ch_3o+oh$	5.00E+13	0.0	0.0
17. $ch_3+oh=ch_2+h_2o$	7.50E+06	2.0	5000.0
18. $ch_2+oh=ch_2o+h$	2.50E+13	0.0	0.0
19. $ch_2+o_2=hco+oh$	4.30E+10	0.0	-500.0
20. $ch_2+o_2=co_2+h_2$	6.90E+11	0.0	500.0
21. $ch_2+o_2=co+h_2o$	2.00E+10	0.0	-1000.0
22. $ch_2+o_2=ch_2o+o$	5.00E+13	0.0	9000.0
23. $ch_2+o_2=co_2+h+h$	1.60E+12	0.0	1000.0
24. $ch_2+o_2=co+oh+h$	8.60E+10	0.0	-500.0
25. $ch_3o+co=ch_3+co_2$	1.57E+14	0.0	11800.0
26. $co+oh=co_2+h$	8.99E+07	1.4	5232.9
27. $o+oh=o_2+h$	4.00E+14	-0.5	0.0
28. $h+ho_2=oh+oh$	1.70E+14	0.0	875.0
29. $oh+oh=o+h_2o$	6.00E+08	1.3	0.0
30. $h+o_2+m=ho_2+m$	3.60E+17	-0.7	0.0
h2o	Enhanced by	2.100E+01	
co2	Enhanced by	5.000E+00	
h2	Enhanced by	3.300E+00	
co	Enhanced by	2.000E+00	
31. $h_2o_2+m=oh+oh+m$	4.30E+16	0.0	45500.0
h2o	Enhanced by	2.100E+01	
co2	Enhanced by	5.000E+00	
h2	Enhanced by	3.300E+00	
co	Enhanced by	2.000E+00	
32. $h_2+oh=h_2o+h$	1.17E+09	1.3	3626.0
33. $ho_2+ho_2=h_2o_2+o_2$	2.00E+12	0.0	0.0
34. $ch_2o+oh=hco+h_2o$	5.56E+10	1.1	-76.5
35. $ch_2o+ho_2=hco+h_2o_2$	3.00E+12	0.0	8000.0
36. $hco+o_2=ho_2+co$	3.30E+13	-0.4	0.0
37. $hco+m=h+co+m$	1.59E+18	0.9	56712.3
38. $ch_3+ch_3o=ch_4+ch_2o$	4.30E+14	0.0	0.0
39. $c_2h_4+oh=ch_2o+ch_3$	6.00E+13	0.0	960.0
40. $c_2h_4+oh=c_2h_3+h_2o$	8.02E+13	0.0	5955.0
41. $c_2h_3+o_2=ch_2o+hco$	4.00E+12	0.0	-250.0
42. $c_2h_3+hco=c_2h_4+co$	6.03E+13	0.0	0.0
43. $c_2h_5+o_2=c_2h_4+ho_2$	2.00E+10	0.0	-2200.0
44. $ch_4+o_2=ch_3+ho_2$	7.90E+13	0.0	56000.0
45. $oh+ho_2=h_2o+o_2$	7.50E+12	0.0	0.0
46. $ch_3+o_2=ch_2o+oh$	3.80E+11	0.0	9000.0
47. $ch_4+h=ch_3+h_2$	6.60E+08	1.6	10840.0
48. $ch_4+oh=ch_3+h_2o$	1.60E+06	2.1	2460.0
49. $ch_4+o=ch_3+oh$	1.02E+09	1.5	8604.0
50. $ch_4+ho_2=ch_3+h_2o_2$	9.00E+11	0.0	18700.0
51. $ch_4+ch_2=ch_3+ch_3$	4.00E+12	0.0	-570.0
52. $c_3h_6=c_2h_3+ch_3$	3.15E+15	0.0	85500.0
53. $ch_2+ch_2=c_2h_2+h_2$	1.20E+13	0.0	800.0
54. $ch_2+ch_2=c_2h_2+h+h$	1.20E+14	0.0	800.0
55. $c_2h_4+m=c_2h_2+h_2+m$	1.50E+14	0.0	55800.0
56. $c_2h_2+o_2=hco+hco$	4.00E+12	0.0	28000.0
57. $c_2h_2+o=ch_2+co$	1.02E+07	2.0	1900.0

58. $c_2h_2+h+m=c_2h_3+m$	5.54E+12	0.0	2410.0
59. $c_2h_3+h=c_2h_2+h_2$	4.00E+13	0.0	0.0
60. $c_2h_3+oh=c_2h_2+h_2o$	3.00E+13	0.0	0.0
61. $c_2h_3+ch_2=c_2h_2+ch_3$	3.00E+13	0.0	0.0
62. $c_2h_3+c_2h_3=c_2h_2+c_2h_4$	1.45E+13	0.0	0.0
63. $c_2h_3+o=c_2h_2+oh$	1.00E+13	0.0	0.0
64. $c_2h_2+oh=ch_3+co$	4.83E-04	4.0	-2000.0
65. $c_2h_3=c_2h_2+h$	4.60E+40	-8.8	46200.0
66. $n+no<=>n_2+o$	3.50E+13	0.0	330.0
67. $n+o_2<=>no+o$	2.65E+12	0.0	6400.0
68. $n+oh<=>no+h$	7.33E+13	0.0	1120.0
69. $n_2o+o<=>n_2+o_2$	1.40E+12	0.0	10810.0
70. $n_2o+o<=>2no$	2.90E+13	0.0	23150.0
71. $n_2o+h<=>n_2+oh$	4.40E+14	0.0	18880.0
72. $n_2o+oh<=>n_2+ho_2$	2.00E+12	0.0	21060.0
73. $n_2o(+m)<=>n_2+o(+m)$	1.30E+11	0.0	59620.0
Low pressure limit:	0.62000E+15	0.00000E+00	0.56100E+05
h2	Enhanced by	2.000E+00	
h2o	Enhanced by	6.000E+00	
ch4	Enhanced by	2.000E+00	
co	Enhanced by	1.500E+00	
co2	Enhanced by	2.000E+00	
74. $ho_2+no<=>no_2+oh$	2.11E+12	0.0	-480.0
75. $no+o+m<=>no_2+m$	1.06E+20	-1.4	0.0
h2	Enhanced by	2.000E+00	
h2o	Enhanced by	6.000E+00	
ch4	Enhanced by	2.000E+00	
co	Enhanced by	1.500E+00	
co2	Enhanced by	2.000E+00	
76. $no_2+o<=>no+o_2$	3.90E+12	0.0	-240.0
77. $no_2+h<=>no+oh$	1.32E+14	0.0	360.0
78. $ch_2+c_2h_2=c_3h_3+h$	1.20E+13	0.0	6620.0
79. $c_2h_2+c_2h_3=c_4h_4+h$	4.90E+16	-1.1	11800.0
80. $c_3h_3+oh=c_2h_3+hco$	2.00E+13	0.0	0.0
81. $2c_3h_3=>A1$	5.00E+06	0.0	0.0
82. $c_2h_2+N-c_4h_3=A1-$	1.90E+63	-15.2	30600.0
Reverse Arrhenius coefficients:	2.56E+75	-16.9	137600.0
83. $c_2h_2+N-c_4h_5=h+A1$	1.60E+18	-1.9	7400.0
Reverse Arrhenius coefficients:	1.65E+27	-2.4	78290.0
84. $h+c_6h_4-1=A1-$	3.90E+69	-16.6	34100.0
Reverse Arrhenius coefficients:	1.26E+75	-16.9	134800.0
85. $h+C-c_6h_4=A1-$	1.50E+47	-9.7	22900.0
Reverse Arrhenius coefficients:	9.42E+50	-10.4	104500.0
86. $N-c_6h_5=A1-$	3.50E+46	-10.4	33600.0
Reverse Arrhenius coefficients:	5.87E+48	-9.9	98060.0
87. $h+c_6h_6-1=h+A1$	3.70E+20	-2.4	6800.0
Reverse Arrhenius coefficients:	1.27E+23	-1.8	70400.0
88. $N-c_6h_7=h+A1$	5.30E+25	-4.4	17300.0
Reverse Arrhenius coefficients:	1.99E+25	-3.3	44690.0
89. $h+A1=C-c_6h_7$	1.40E+51	-11.9	16100.0
Reverse Arrhenius coefficients:	2.39E+54	-13.0	39670.0

90. $h+A1=A1+h2$	4.00E+12	0.0	7887.0
Reverse Arrhenius coefficients:	3.55E+07	1.0	-207.0
91. $oh+A1=A1+h2o$	1.60E+08	1.4	1450.0
Reverse Arrhenius coefficients:	9.08E+04	2.1	9303.0
92. $h+A1-(+M)=A1(+M)$	1.00E+14	0.0	0.0
Low pressure limit:	0.66000E+76	-0.16300E+02	0.70000E+04
TROE centering:	0.10000E+01	0.10000E+00	0.58490E+03 0.10000E+16
ch4	Enhanced by	2.000E+00	
co	Enhanced by	1.500E+00	
co2	Enhanced by	2.000E+00	
h2	Enhanced by	2.000E+00	
h2o	Enhanced by	6.000E+00	
93. $o+A1=h+c6h5o$	2.20E+13	0.0	4530.0
Reverse Arrhenius coefficients:	4.01E+14	-0.5	19450.0
94. $oh+A1=h+c6h5oh$	1.30E+13	0.0	10600.0
Reverse Arrhenius coefficients:	3.73E+16	-0.9	9979.0
95. $A1+o2=o+c6h5o$	2.10E+12	0.0	7470.0
Reverse Arrhenius coefficients:	1.52E+16	-1.0	15050.0
96. $c4h2+N-c4h3=A1c2h-$	1.90E+63	-15.2	3.1
Reverse Arrhenius coefficients:	2.15E+77	-17.4	135100.0
97. $c2h+A1=h+A1c2h$	5.00E+13	0.0	0.0
Reverse Arrhenius coefficients:	3.43E+20	-1.7	28920.0
98. $c2h2+A1=-N-A1c2h2$	7.90E+29	-5.2	13700.0
Reverse Arrhenius coefficients:	1.71E+37	-6.9	53320.0
99. $c2h2+A1=-h+A1c2h$	2.50E+29	-4.4	26400.0
Reverse Arrhenius coefficients:	3.61E+36	-6.0	33280.0
100. $h+A1c2h=N-A1c2h2$	1.60E+32	-5.7	11090.0
Reverse Arrhenius coefficients:	2.39E+32	-5.9	43820.0
101. $h+A1c2h=I-A1c2h2$	1.60E+32	-5.7	11090.0
Reverse Arrhenius coefficients:	8.08E+34	-6.3	52440.0
102. $h+A1c2h=A1c2h*+h2$	2.50E+14	0.0	16000.0
Reverse Arrhenius coefficients:	4.28E+09	1.1	7271.0
103. $h+A1c2h=A1c2h+h2$	2.50E+14	0.0	16000.0
Reverse Arrhenius coefficients:	4.30E+09	1.1	7633.0
104. $oh+A1c2h=A1c2h*+h2o$	1.60E+08	1.4	1450.0
Reverse Arrhenius coefficients:	1.75E+05	2.2	8668.0
105. $oh+A1c2h=A1c2h+h2o$	1.60E+08	1.4	1450.0
Reverse Arrhenius coefficients:	1.76E+05	2.2	9031.0
106. $h+A1c2h-(+M)=A1c2h(+M)$	1.00E+14	0.0	0.0
Low pressure limit:	0.66000E+76	-0.16300E+02	0.70000E+04
TROE centering:	0.10000E+01	0.10000E+00	0.58490E+03 0.10000E+16
ch4	Enhanced by	2.000E+00	
co	Enhanced by	1.500E+00	
co2	Enhanced by	2.000E+00	
h2	Enhanced by	2.000E+00	
h2o	Enhanced by	6.000E+00	
107. $h+A1c2h*(+M)=A1c2h(+M)$	1.00E+14	0.0	0.0
Low pressure limit:	0.66000E+76	-0.16300E+02	0.70000E+04
TROE centering:	0.10000E+01	0.10000E+00	0.58490E+03 0.10000E+16
ch4	Enhanced by	2.000E+00	
co	Enhanced by	1.500E+00	

co2	Enhanced by	2.000E+00		
h2	Enhanced by	2.000E+00		
h2o	Enhanced by	6.000E+00		
108. c2h2+A1c2h*=A1c2hAC		1.00E+13	0.0	0.0
Reverse Arrhenius coefficients:		7.93E+19	-1.6	43310.0
109. A1c2hAC=A2-X		1.00E+10	0.0	0.0
Reverse Arrhenius coefficients:		2.09E+14	-0.3	48250.0
110. o2+A1c2hAC=>2hco+A1c2h*		1.00E+13	0.0	0.0
111. h+A2-X=A2		1.00E+13	0.0	0.0
Reverse Arrhenius coefficients:		2.23E+18	-0.9	116100.0
112. h+A2=h2+A2-X		1.00E+14	0.0	0.0
Reverse Arrhenius coefficients:		1.19E+09	0.9	-11870.0
113. oh+A2=h2o+A2-X		2.10E+13	0.0	19.1
Reverse Arrhenius coefficients:		1.60E+10	0.6	4095.0
114. c2h+A2=c2h2+A2-X		2.00E+13	0.0	0.0
Reverse Arrhenius coefficients:		1.27E+13	-0.2	18260.0
115. ch3+A2=ch4+A2-X		2.00E+13	0.0	0.0
Reverse Arrhenius coefficients:		6.18E+12	0.1	-8889.0
116. oh+A2=>hco+ch2-3+A1c2h		1.00E+13	0.0	0.0
117. o2+A2-X=>hco+A1c2h+co		1.00E+13	0.0	0.0
118. c2h2+A2-X=h+A2R5		1.00E+13	0.0	0.0
Reverse Arrhenius coefficients:		2.94E+20	-1.3	39560.0
119. h+A2R5-=A2R5		1.00E+13	0.0	0.0
Reverse Arrhenius coefficients:		1.11E+18	-0.9	116100.0
120. h+A2R5=h2+A2R5-		1.00E+14	0.0	0.0
Reverse Arrhenius coefficients:		2.38E+09	0.9	-11870.0
121. oh+A2R5=h2o+A2R5-		2.10E+13	0.0	19.1
Reverse Arrhenius coefficients:		3.20E+10	0.6	4094.0
122. c2h+A2R5=c2h2+A2R5-		2.00E+13	0.0	0.0
Reverse Arrhenius coefficients:		2.55E+13	-0.2	18250.0
123. ch3+A2R5=ch4+A2R5-		2.00E+13	0.0	0.0
Reverse Arrhenius coefficients:		1.24E+13	0.1	-8889.0
124. h+A2R5c2h=c2h2+A2R5-		1.00E+14	0.0	0.0
Reverse Arrhenius coefficients:		5.77E+07	1.2	-8984.0
125. c2h+A2R5c2h=c4h2+A2R5-		2.00E+13	0.0	0.0
Reverse Arrhenius coefficients:		1.83E+12	0.1	22230.0
126. h+A2R5c2h*=A2R5c2h		1.00E+13	0.0	0.0
Reverse Arrhenius coefficients:		5.57E+17	-0.9	116100.0
127. h+A2R5c2h=h2+A2R5c2h*		1.00E+14	0.0	0.0
Reverse Arrhenius coefficients:		4.76E+09	0.9	-11870.0
128. oh+A2R5c2h=h2o+A2R5c2h*		2.10E+13	0.0	19.1
Reverse Arrhenius coefficients:		6.40E+10	0.6	4094.0
129. c2h+A2R5c2h=c2h2+A2R5c2h*		2.00E+13	0.0	0.0
Reverse Arrhenius coefficients:		5.10E+13	-0.2	18250.0
130. ch3+A2R5c2h=ch4+A2R5c2h*		2.00E+13	0.0	0.0
Reverse Arrhenius coefficients:		2.47E+13	0.1	-8889.0
131. c2h2+A2R5c2h*=ANc2hAC		1.00E+13	0.0	0.0
Reverse Arrhenius coefficients:		3.59E+20	-1.7	48600.0
132. ANc2hAC=A3R5-		1.00E+10	0.0	0.0
Reverse Arrhenius coefficients:		2.09E+14	-0.3	50450.0
133. h+A3R5-=A3R5		1.00E+13	0.0	0.0

	Reverse Arrhenius coefficients:	5.57E+17	-0.9	116100.0
134.	$\text{h}+\text{A3R5}=\text{h2}+\text{A3R5}$ -	1.00E+14	0.0	0.0
	Reverse Arrhenius coefficients:	4.76E+09	0.9	-11870.0
135.	$\text{oh}+\text{A3R5}=\text{h2o}+\text{A3R5}$ -	2.10E+13	0.0	19.1
	Reverse Arrhenius coefficients:	6.40E+10	0.6	4096.0
136.	$\text{c2h}+\text{A3R5}=\text{c2h2}+\text{A3R5}$ -	2.00E+13	0.0	0.0
	Reverse Arrhenius coefficients:	5.10E+13	-0.2	18260.0
137.	$\text{ch3}+\text{A3R5}=\text{ch4}+\text{A3R5}$ -	2.00E+13	0.0	0.0
	Reverse Arrhenius coefficients:	2.47E+13	0.1	-8887.0
138.	$\text{oh}+\text{A2R5}=\text{hcco}+\text{A2}$	1.00E+13	0.0	0.0
139.	$\text{o2}+\text{A2R5}=\text{2co}+\text{A2-X}$	1.00E+13	0.0	0.0
140.	$\text{oh}+\text{A2R5c2h}=\text{hcco}+\text{A2R5}$	1.00E+13	0.0	0.0
141.	$\text{o2}+\text{A2R5c2h}^*=\text{2co}+\text{A2R5}$ -	1.00E+13	0.0	0.0
142.	$\text{o2}+\text{ANc2hAC}=\text{2hco}+\text{A2R5c2h}^*$	1.00E+13	0.0	0.0
143.	$\text{oh}+\text{A3R5}=\text{hco}+\text{ch2-3}+\text{A2R5c2h}$	1.00E+13	0.0	0.0
144.	$\text{o2}+\text{A3R5}=\text{hco}+\text{co}+\text{A2R5c2h}$	1.00E+13	0.0	0.0

REFERENCES

1. "EPA," <http://www.epa.gov/air/criteria.html>, March-01-2014.
2. Wei, E.T., Shu, H.P., "Nitroaromatic Carcinogens in Diesel Soot - a Review of Laboratory Findings," *American Journal of Public Health*, 73 (1983) 1085-1088.
3. Kong, S.-C., Reitz, R.D., "Use of detailed chemical kinetics to study HCCI engine combustion with consideration of turbulent mixing effects," *Journal of Engineering for Gas Turbines and Power-Transactions of the Asme*, 124 (2002) 702-707.
4. "CHEMKIN 4," <http://www.reactiondesign.com>, July-25-2012.
5. Turns, S.R., "An introduction to combustion : concepts and applications," 2nd ed., WCB/McGraw-Hill, Boston, 2000.
6. Magnussen, B.F., "On the Structure of Turbulence and a Generalized Eddy Dissipation Concept for Chemical Reaction in Turbulent Flow," Nineteenth AIAA Meeting, 1981,
7. Magnussen, B.F., Hjertager, B.H., "On mathematical models of turbulent combustion with special emphasis on soot formation and combustion," In 16th Symp. (Int'l.) on Combustion, 1976,
8. Kong, S.-C., Kim, H., Reitz, R.D., Kim, Y., "Comparisons of combustion simulations using a Representative Interactive Flamelet model and direct integration of CFD with detailed chemistry," *Proceedings of the 2005 Spring Technical Conference of the ASME Internal Combustion Engine Division*, (2005) 159-169.
9. Kong, S.-C., Reitz, R.D., "Multidimensional Modeling of Diesel Ignition and Combustion Using a Multistep Kinetics Model," *Journal of Engineering for Gas Turbines and Power-Transactions of the Asme*, 115 (1993) 781-789.
10. Westbrook, C.K., Pitz, W.J., Curran, H.J., "Chemical kinetic modeling study of the effects of oxygenated hydrocarbons on soot emissions from diesel engines," *Journal of Physical Chemistry A*, 110 (2006) 6912-6922.
11. Lu, T.F., Law, C.K., "A directed relation graph method for mechanism reduction," *Proceedings of the Combustion Institute*, 30 (2005) 1333-1341.
12. Lu, T.F., Ju, Y.G., Law, C.K., "Complex CSP for chemistry reduction and analysis," *Combustion and Flame*, 126 (2001) 1445-1455.
13. Lakshminarayanan, P.A., Aghav, Y.V., "Multi-dimensional Modelling of Diesel Combustion: Review," *Modelling Diesel Combustion*, (2010) 207-246.

14. Nishida, K., Hiroyasu, H., "Simplified Three-Dimensional Modeling of Mixture Formation and Combustion in a D.I. Diesel Engine," SAE Technical Paper 890269, 1989, doi:[10.4271/890269](https://doi.org/10.4271/890269).
15. Amsden, A.A., KIVA-3V: A Block-Structured KIVA Program for Engines with Vertical or Canted Valves, (version 3V), Los Alamos National Labs report LA-13313-MS Los Alamos, New Mexico, 1997.
16. Amsden, A.A., P.J.O'Rourke, Butler, T.D., KIVA II - A computer program for chemically reacting flows with sprays, (version II), Los Alamos National Laboratory, Los Alamos, New Mexico, 1989.
17. ANSYS FLUENT, (version 14.0), Chapter 16: Discrete Phase, Fluent Theory Guide, ANSYS Inc., 2011.
18. O'Rourke, P., Amsden, A., "The Tab Method for Numerical Calculation of Spray Droplet Breakup," SAE Technical Paper 872089, 1987, doi:[doi:10.4271/872089](https://doi.org/10.4271/872089).
19. Reitz, R.D., "Modeling atomization processes in high-pressure vaporizing sprays," *Atomisation Spray Technology*, 3 (1987) 309-337.
20. Patterson, M., Reitz, R.D., "Modeling the Effects of Fuel Spray Characteristics on Diesel Engine Combustion and Emission," SAE Technical Paper 980131, 1998.
21. O'Rourke, P.J., "Collective Drop Effects on Vaporizing Liquid Sprays," PhD thesis, Princeton University, 1981.
22. Faeth, G.M., "Current Status of Droplet and Liquid Combustion," *Progress in Energy and Combustion Science*, 3 (1977) 191-224.
23. Demirbas, A., "Political, economic and environmental impacts of biofuels: A review," *Applied Energy*, 86 (2009) S108-S117.
24. Brown, R.C., "Biorenewable resources: engineering new products from agriculture," Wiley-Blackwell, 2003.
25. Hamelinck, C.N., Faaij, A.P.C., "Future prospects for production of methanol and hydrogen from biomass," *Journal of Power Sources*, 111 (2002) 1-22.
26. Tock, L., Gassner, M., Marechal, F., "Thermochemical production of liquid fuels from biomass: Thermo-economic modeling, process design and process integration analysis," *Biomass Bioenerg.*, 34 (2010) 1838-1854.
27. Lieuwen, T., Yang, V., Yetter, R., "Synthesis Gas Combustion: Fundamentals and Applications," CRC Press, 2009.
28. Drake, M.C., Blint, R.J., "Thermal NO_x in stretched laminar opposed-flow diffusion flames with CO/H₂/N₂ fuel," *Combustion and Flame*, 76 (1989) 151-167.

29. Weydahl, T., Bugge, M., Gran, I., Ertesvåg, I., "Computational modeling of nitric oxide formation in biomass combustion " *International Journal of Applied Mechanics in Engineering*, 7 (2001) 125-141.
30. Bowman, C.T., Hanson, R.K., Davidson, D.F., W.C. Gardiner, J., Lissianski, V., Smith, G.P., Golden, D.M., Frenklach, M., Goldenberg, M., "GRI 2.11 mechanism," http://www.me.berkeley.edu/gri_mech/, April-01-2013.
31. Giles, D.E., Som, S., Aggarwal, S.K., "NO_x emission characteristics of counterflow syngas diffusion flames with airstream dilution," *Fuel*, 85 (2006) 1729-1742.
32. Shih, H.Y., Hsu, J.R., "Computed NO_x emission characteristics of opposed-jet syngas diffusion flames," *Combustion and Flame*, 159 (2012) 1851-1863.
33. Sethuraman, S., Van Huynh, C., Kong, S.-C., "Producer Gas Composition and NO_x Emissions from a Pilot-Scale Biomass Gasification and Combustion System Using Feedstock with Controlled Nitrogen Content," *Energy & Fuels*, 25 (2011) 813-822.
34. Huynh, C.V., Kong, S.-C., "Performance characteristics of a pilot-scale biomass gasifier using oxygen-enriched air and steam," *Fuel*, 103 (2013) 987-996.
35. Adouane, B., Hoppesteyn, P., de Jong, W., van der Wel, M., Hein, K.R.G., Spliethoff, H., "Gas turbine combustor for biomass derived LCV gas, a first approach towards fuel-NO_x modelling and experimental validation," *Applied Thermal Engineering*, 22 (2002) 959-970.
36. Azuhata, S., Kaji, R., Akimoto, H., Hishinuma, Y., "A study of the kinetics of the NH₃-NO-O₂-H₂O₂ reaction," *Symposium (International) on Combustion*, 18 (1981) 845-852.
37. Drake, M.C., Pitz, R.W., Correa, S.M., Lapp, M., "Nitric oxide formation from thermal and fuel-bound nitrogen sources in a turbulent nonpremixed syngas flame," *Symposium (International) on Combustion*, 20 (1985) 1983-1990.
38. Miller, J.A., Bowman, C.T., "Mechanism and Modeling of Nitrogen Chemistry in Combustion," *Progress in Energy and Combustion Science*, 15 (1989) 287-338.
39. Zabetta, E.C., Kilpinen, P., Hupa, M., Stahl, K., Leppalahti, J., Cannon, M., Nieminen, J., "Kinetic modeling study on the potential of staged combustion in gas turbines for the reduction of nitrogen oxide emissions from biomass IGCC plants (vol 14, pg 751, 2000)," *Energy & Fuels*, 14 (2000) 1335-1335.
40. Sullivan, N., Jensen, A., Glarborg, P., Day, M.S., Grcar, J.F., Bell, J.B., "Ammonia conversion and NO_x formation in laminar coflowing nonpremixed methane-air flames," *Combustion and Flame*, 131 (2002) 285-298.
41. Zabetta, E.C., Hupa, M., Saviharju, K., "Reducing NO_x emissions using fuel staging, air staging, and selective noncatalytic reduction in synergy," *Industrial & Engineering Chemistry Research*, 44 (2005) 4552-4561.

42. Tesner, P.A., Snegirio.Td, Knorre, V.G., "Kinetics of Dispersed Carbon Formation," *Combustion and Flame*, 17 (1971) 253-&.
43. Surovikin, V., "Analytical description of the processes of nucleus-formation and growth of particles of carbon black in the thermal decomposition of aromatic hydrocarbons in the gas phase," *Khimiya Tverdogo Topliva*, 10 (1976) 111-122.
44. Nagle, J., Strickland-Constable, R., "Oxidation of carbon between 1000-2000 C," *Proceedings of the fifth carbon conference*, Pergamon New York, 1962, pp. 154-164.
45. Kong, S.-C., Han, Z., Reitz, R.D., "The development and application of a diesel ignition and combustion model for multidimensional engine simulations," *Assessment*, 2013 (1995) 09-06.
46. Han, Z., Uludogan, A., Hampson, G., Reitz, R.D., "Mechanism of Soot and NO_x Emission Reduction Using Multiple-injection in a Diesel Engine," SAE Technical Paper 960633, 1996, doi:[10.4271/960633](https://doi.org/10.4271/960633).
47. Kong, S.-C., Sun, Y., Rietz, R.D., "Modeling Diesel Spray Flame Liftoff, Sooting Tendency, and NO_x Emissions Using Detailed Chemistry With Phenomenological Soot Model," *Journal of Engineering for Gas Turbines and Power*, 129 (2007) 245-251.
48. D'Errico, G., Ettorre, D., Lucchini, T., "Comparison of combustion and pollutant emission models for DI diesel engines," SAE Technical paper 2007-24-0045, 2007.
49. Vishwanathan, G., Reitz, R.D., "Modeling Soot Formation Using Reduced Polycyclic Aromatic Hydrocarbon Chemistry in n-Heptane Lifted Flames With Application to Low Temperature Combustion," *Journal of Engineering for Gas Turbines and Power-Transactions of the Asme*, 131 (2009).
50. Frenklach, M., Clary, D.W., Gardiner Jr, W.C., Stein, S.E., "Detailed kinetic modeling of soot formation in shock-tube pyrolysis of acetylene," *Symposium (International) on Combustion*, 20 (1985) 887-901.
51. Wang, H., Frenklach, M., "A detailed kinetic modeling study of aromatics formation in laminar premixed acetylene and ethylene flames," *Combustion and Flame*, 110 (1997) 173-221.
52. Appel, J., Bockhorn, H., Frenklach, M., "Kinetic modeling of soot formation with detailed chemistry and physics: laminar premixed flames of C₂ hydrocarbons," *Combustion and Flame*, 121 (2000) 122-136.
53. Mauss, F., Schäfer, T., Bockhorn, H., "Inception and growth of soot particles in dependence on the surrounding gas phase," *Combustion and Flame*, 99 (1994) 697-705.
54. Mauss, F., Trilken, B., Breitbach, H., Peters, N., "Soot formation in partially premixed diffusion flames at atmospheric pressure," *Soot formation in combustion*, Springer, 1994, pp. 325-349.

55. Leung, K.M., Lindstedt, R.P., Jones, W.P., "A Simplified Reaction-Mechanism for Soot Formation in Nonpremixed Flames," *Combustion and Flame*, 87 (1991) 289-305.
56. Belardini, P., Bertoli, C., Beatrice, C., D'anna, A., Del Giacomo, N., "Application of a reduced kinetic model for soot formation and burnout in three-dimensional diesel combustion computations," *Symposium (International) on Combustion*, 26 (1996) 2517-2524.
57. Kazakov, A., Foster, D.E., "Modeling of soot formation during DI diesel combustion using a multi-step phenomenological model," SAE Technical paper 982463, 1998.
58. Tao, F., Golovitchev, V.I., Chomiak, J., "A phenomenological model for the prediction of soot formation in diesel spray combustion," *Combustion and Flame*, 136 (2004) 270-282.
59. Boulanger, J., Liu, F., Neill, W.S., Smallwood, G.J., "An improved soot formation model for 3D diesel engine simulations," *Journal of Engineering for Gas Turbines and Power*, 129 (2007) 877-884.
60. Tao, F., Reitz, R.D., Foster, D.E., Liu, Y., "Nine-step phenomenological diesel soot model validated over a wide range of engine conditions," *International Journal of Thermal Sciences*, 48 (2009) 1223-1234.
61. Vishwanathan, G., Reitz, R.D., "Development of a practical soot modeling approach and its application to low-temperature diesel combustion," *Combustion Science and Technology*, 182 1050-1082.
62. Lapuerta, M., Armas, O., Rodriguez-Fernandez, J., "Effect of biodiesel fuels on diesel engine emissions," *Progress in Energy and Combustion Science*, 34 (2008) 198-223.
63. Kumar, N., Chauhan, S.R., "Performance and emission characteristics of biodiesel from different origins: A review," *Renewable and Sustainable Energy Reviews*, 21 633-658.
64. Torres, D., O'Rourke, P., Amsden, A., "A discrete multicomponent fuel model," *Atomization and Sprays*, 13 (2003).
65. Zhang, L., Kong, S.-C., "Vaporization modeling of petroleum-biofuel drops using a hybrid multi-component approach," *Combustion and Flame*, 157 (2010) 2165-2174.
66. Ra, Y., Reitz, R.D., "A vaporization model for discrete multi-component fuel sprays," *International Journal of Multiphase Flow*, 35 (2009) 101-117.
67. Zhang, L., Kong, S.-C., "Modeling of multi-component fuel vaporization and combustion for gasoline and diesel spray," *Chemical Engineering Science*, 64 (2009) 3688-3696.
68. Yuan, W., Hansen, A.C., Zhang, Q., "Predicting the physical properties of biodiesel for combustion modeling," *Transactions of the ASAE*, 46 (2003) 1487-1493.

69. Brakora, J.L., "A Comprehensive Combustion Model for Biodiesel-Fueled Engine Simulations," PhD Dissertation, University of Wisconsin-Madison, 2012.
70. Saha, K., Abu-Ramadan, E., Li, X.G., "Multicomponent evaporation model for pure and blended biodiesel droplets in high temperature convective environment," *Applied Energy*, 93 (2012) 71-79.
71. Abramzon, B., Sirignano, W.A., "Droplet Vaporization Model for Spray Combustion Calculations," *International Journal of Heat and Mass Transfer*, 32 (1989) 1605-1618.
72. Renksizbulut, M., Haywood, R.J., "Transient Droplet Evaporation with Variable Properties and Internal Circulation at Intermediate Reynolds-Numbers," *International Journal of Multiphase Flow*, 14 (1988) 189-202.
73. Yuan, W., Hansen, A., "Computational investigation of the effect of biodiesel fuel properties on diesel engine NOx emissions," *International Journal of Agricultural and Biological Engineering*, 2 (2009) 41-48.
74. Fisher, E., Pitz, W., Curran, H., Westbrook, C., "Detailed chemical kinetic mechanisms for combustion of oxygenated fuels," *Proceedings of the Combustion Institute*, 28 (2000) 1579-1586.
75. Brakora, J.L., Ra, Y., Reitz, R.D., McFarlane, J., Daw, C.S., "Development and validation of a reduced reaction mechanism for biodiesel-fueled engine simulations," *SAE International Journal of Fuels and Lubricants*, 1 (2009) 675-702.
76. Brakora, J., Reitz, R.D., "A Comprehensive Combustion Model for Biodiesel-Fueled Engine Simulations," SAE Technical Paper 2013-01-1099, 2013.
77. Herbinet, O., Pitz, W.J., Westbrook, C.K., "Detailed chemical kinetic oxidation mechanism for a biodiesel surrogate," *Combustion and Flame*, 154 (2008) 507-528.
78. Herbinet, O., Pitz, W.J., Westbrook, C.K., "Detailed chemical kinetic mechanism for the oxidation of biodiesel fuels blend surrogate," *Combustion and Flame*, 157 (2010) 893-908.
79. Wang, W., Gowdagiri, S., Oehlschlaeger, M.A., "Comparative Study of the Autoignition of Methyl Decanoates, Unsaturated Biodiesel Fuel Surrogates," *Energy & Fuels*, 27 5527-5532.
80. Yuan, W., Hansen, A.C., Tat, M.E., Van Gerpen, J.H., Tan, Z., "Spray, ignition, and combustion modeling of biodiesel fuels for investigating NOx emissions," *Transactions of the ASAE*, 48 (2005) 933-939.
81. Yang, J., Golovitchev, V.I., Redón Lurbe, P., López Sánchez, J.J., "Chemical Kinetic Study of Nitrogen Oxides Formation Trends in Biodiesel Combustion," *International Journal of Chemical Engineering*, (2012) 22.

82. Karra, P.K., Veltman, M.K., Kong, S.-C., "Characteristics of engine emissions using biodiesel blends in low-temperature combustion regimes," *Energy & Fuels*, 22 (2008) 3763-3770.
83. Nerva, J.-G., Genzale, C.L., Kook, S., Garca-Oliver, J.M., Pickett, L.M., "Fundamental spray and combustion measurements of soy methyl-ester biodiesel," *International Journal of Engine Research*, 14 (2013) 373-390.
84. Pickett, L.M., Siebers, D.L., "Soot in diesel fuel jets: effects of ambient temperature, ambient density, and injection pressure," *Combustion and Flame*, 138 (2004) 114-135.
85. Menard, T., Tanguy, S., Berlemont, A., "Coupling level set/VOF/ghost fluid methods: Validation and application to 3D simulation of the primary break-up of a liquid jet," *International Journal of Multiphase Flow*, 33 (2007) 510-524.
86. Li, Y., Kong, S.-C., "Mesh refinement algorithms in an unstructured solver for multiphase flow simulation using discrete particles," *Journal of Computational Physics*, 228 (2009) 6349-6360.
87. Béard, P., Duclos, J., Habchi, C., Bruneaux, G., Mokaddem, K., Baritaud, T., "Extension of Lagrangian-Eulerian Spray Modeling: Application to High Pressure Evaporating Diesel Sprays," 2000, doi:[10.4271/2000-01-1893](https://doi.org/10.4271/2000-01-1893).
88. Sterno, N., Greeves, G., Tullis, S., Jiang, X., Zhao, H., "Improvements of the KIVA Dense Spray Modeling for HSDI Diesel Engines," SAE Technical Paper 2007-01-0001 2007, doi:[10.4271/2007-01-0001](https://doi.org/10.4271/2007-01-0001).
89. Abani, N., Reitz, R.D., "Modeling Subgrid-Scale Mixing of Vapor in Diesel Sprays Using Jet Theory," *Atomization and Sprays*, 20 (2010) 71-83.
90. Coppens, F.H.V., De Ruyck, J., Konnov, A.A., "The effects of composition on burning velocity and nitric oxide formation in laminar premixed flames of CH₄+H₂+O₂+N₂," *Combustion and Flame*, 149 (2007) 409-417.
91. Tian, Z., Li, Y., Zhang, L., Glarborg, P., Qi, F., "An experimental and kinetic modeling study of premixed NH₃/CH₄/O₂/Ar flames at low pressure," *Combustion and Flame*, 156 (2009) 1413-1426.
92. Zabetta, E.C., Hupa, M., "A detailed kinetic mechanism including methanol and nitrogen pollutants relevant to the gas-phase combustion and pyrolysis of biomass-derived fuels," *Combustion and Flame*, 152 (2008) 14-27.
93. Smith, G.P., Golden, D.M., Frenklach, M., Moriarty, N.W., Eiteneer, B., Goldenberg, M., Bowman, C.T., Hanson, R.K., Song, S., Gardiner, W.C., Lissianski, V.V., Qin, Z., "GRI 3.0 Mechanism," http://www.me.berkeley.edu/gri_mech/, July-18-2012.

94. Braun-Unkhoff, M., Slavinskaya, N., Aigner, M., "A Detailed and Reduced Reaction Mechanism of Biomass-Based Syngas Fuels," *Journal of Engineering for Gas Turbines and Power-Transactions of the Asme*, 132 (2010).
95. Coppens, F.H.V., De Ruyck, J., Konnov, A.A., "The effects of composition on burning velocity and nitric oxide formation in laminar premixed flames of $\text{CH}_4 + \text{H}_2 + \text{O}_2 + \text{N}_2$," *Combustion and Flame*, 149 (2007) 409-417.
96. Kumar, P., Li, M., Roy, S., Kulatilaka, W., Gord, J.R., Katta, V., Meyer, T.R., "Experimental and numerical investigation of fuel-bound NO formation in NH_3 -seeded flames," Spring Technical Meeting of the Central States Section of the Combustion Institute 2012,
97. Ouimette, P., Seers, P., "Numerical comparison of premixed laminar flame velocity of methane and wood syngas," *Fuel*, 88 (2009) 528-533.
98. Wang, H., Frenklach, M., "Detailed Reduction of Reaction-Mechanisms for Flame Modeling," *Combustion and Flame*, 87 (1991) 365-370.
99. "Ansys Fluent v14.0.0," <http://www.ansys.com/Products/Simulation+Technology/Fluid+Dynamics/ANSYS+Fluent>, July-25-2012.
100. Pope, S.B., "Computationally efficient implementation of combustion chemistry using in situ adaptive tabulation," *Combustion Theory and Modelling*, 1 (1997) 41-63.
101. Han, Z., Reitz, R.D., "A temperature wall function formulation for variable-density turbulent flows with application to engine convective heat transfer modeling," *International Journal of Heat and Mass Transfer*, 40 (1997) 613-625.
102. Reitz, R.D., Kuo, T.-W., "Modeling of HC emissions due to crevice flows in premixed-charge engines," SAE Technical Paper 892085, 1989.
103. Han, Z., Reitz, R.D., "Turbulence Modeling of Internal Combustion Engines Using RNG k- ϵ Models," *Combustion Science and Technology*, 106 (1995) 267-295.
104. Patel, A., Kong, S.-C., Reitz, R.D., "Development and Validation of a Reduced Reaction Mechanism for HCCI Engine Simulations," SAE Technical Paper 2004-01-0558, 2004, doi:[10.4271/2004-01-0558](https://doi.org/10.4271/2004-01-0558).
105. Li, Y., Kong, S.-C., "Diesel combustion modelling using LES turbulence model with detailed chemistry," *Combustion Theory and Modelling*, 12 (2008) 205-219.
106. Zeuch, T., Moreac, G., Ahmed, S.S., Mauss, F., "A comprehensive skeletal mechanism for the oxidation of n-heptane generated by chemistry-guided reduction," *Combustion and Flame*, 155 (2008) 651-674.

107. Ciezki, H., Adomeit, G., "Shock-tube investigation of self-ignition of n-heptane-air mixtures under engine relevant conditions," *Combustion and Flame*, 93 (1993) 421-433.
108. Davis, S.G., Law, C.K., "Laminar flame speeds and oxidation kinetics of iso-octane-air and n-heptane-air flames," *Symposium (International) on Combustion*, 27 (1998) 521-527.
109. "Digital Analysis of Reactive Systems © DigAnaRS," <http://www.diganars.com>, March-20-2013.
110. Kent, J.H., Wagner, H.G., "Soot Measurements in Laminar Ethylene Diffusion Flames," *Combustion and Flame*, 47 (1982) 53-65.
111. Dworkin, S.B., Zhang, Q., Thomson, M.J., Slavinskaya, N.A., Riedel, U., "Application of an enhanced PAH growth model to soot formation in a laminar coflow ethylene/air diffusion flame," *Combustion and Flame*, 158 (2011) 1682-1695.
112. Yoshihara, Y., Kazakov, A., Wang, H., Frenklach, M., "Reduced mechanism of soot formation Application to natural gas-fueled diesel combustion," *Symposium (International) on Combustion*, 25 (1994) 941-948.
113. Ladommatos, N., Song, H., Zhao, H., "Measurements and predictions of diesel soot oxidation rates," *Proceedings of the Institution of Mechanical Engineers Part D-Journal of Automobile Engineering*, 216 (2002) 677-689.
114. Fenimore, C.P., Jones, G.W., "Oxidation of Soot by Hydroxyl Radicals," *Journal of Physical Chemistry*, 71 (1967) 593-597.
115. Balthasar, M., Heyl, A., Mauss, F., Schmitt, F., Bockhorn, H., "Flamelet modeling of soot formation in laminar ethyne/air-diffusion flames," *Symposium (International) on Combustion*, 26 (1996) 2369-2377.
116. Netzell, K., Lehtiniemi, H., Mauss, F., "Calculating the soot particle size distribution function in turbulent diffusion flames using a sectional method," *Proceedings of the Combustion Institute*, 31 (2007) 667-674.
117. "Engine Combustion Network," <http://www.sandia.gov/ecn>, Mar-23-2013.
118. Sukumaran, S., Kong, S.-C., Cho, N.H., "Modeling Evaporating Diesel Sprays Using an Improved Gas Particle Model," SAE Technical Paper 2013-2001-1598, 2013.
119. Pang, B., Xie, M.-Z., Jia, M., Liu, Y.-D., "Development of a Phenomenological Soot Model Coupled with a Skeletal PAH Mechanism for Practical Engine Simulation," *Energy & Fuels*, 27 (2013) 1699-1711.
120. Wang, H., Reitz, R.D., Yao, M., Yang, B., Jiao, Q., Qiu, L., "Development of an n-heptane-n-butanol-PAH mechanism and its application for combustion and soot prediction," *Combustion and Flame*, 160 (2013) 504-519.

121. Dukowicz, J.K., "A particle-fluid numerical model for liquid sprays," *Journal of Computational Physics*, 35 (1980) 229-253.
122. D'Errico, G., Lucchini, T., "Validation of spray and combustion models for Diesel engines using constant-volume experiments," Proceedings of the ILASS America Conference, 2011.
123. Som, S., Senecal, P., Pomraning, E., "Comparison of RANS and LES turbulence models against constant volume diesel experiments," 24th Annual Conference on Liquid Atomization and Spray Systems, ILASS Americas, San Antonio, TX, 2012.
124. Yuan, W., Hansen, A., Zhang, Q., "Vapor pressure and normal boiling point predictions for pure methyl esters and biodiesel fuels," *Fuel*, 84 (2005) 943-950.
125. Yaws, C.L., Gabbula, C., "Yaws" Handbook of Thermodynamic and Physical Properties of Chemical Compounds," Knovel, 2003.
126. Yuan, W., Hansen, A.C., Zhang, Q., "Predicting the temperature dependent viscosity of biodiesel fuels," *Fuel*, 88 (2009) 1120-1126.
127. Fuller, E.N., Schettle, P.D., Giddings, J.C., "A New Method for Prediction of Binary Gas-Phase Diffusion Coefficients," *Industrial and Engineering Chemistry*, 58 (1966) 19-27.
128. Naber, J.D., Siebers, D.L., "Effects of gas density and vaporization on penetration and dispersion of diesel sprays," SAE Technical Paper 960034, 1996,
129. Morin, C., Chauveau, C., Gokalp, I., "Droplet vaporisation characteristics of vegetable oil derived biofuels at high temperatures," *Experimental Thermal and Fluid Science*, 21 (2000) 41-50.